Bernd Fuchsbichler

High Capacity Intermetallic Composite Anode Materials for Lithium Ion Batteries

Doctoral Thesis

Submitted in fulfilment for doctor`s degree of technical science

at

Graz University of Technology

Univ.-Prof.Dipl.-Ing. Dr. Franz Stelzer

Institute for Chemistry and Technology of Materials

Graz University of Technology

2011

Meinen Eltern

Deutsche Fassung:

Beschluss der Curricula-Kommission für Bachelor-, Master- und Diplomstudien vom 10.11.2008

Genehmigung des Senates am 1.12.2008

EIDESSTATTLICHE ERKLÄRUNG

Ich erkläre an Eides statt, dass ich die vorliegende Arbeit selbstständig verfasst, andere als die angegebenen Quellen/Hilfsmittel nicht benutzt, und die den benutzten Quellen wörtlich und inhaltlich entnommene Stellen als solche kenntlich gemacht habe.

Graz, am …… ……..

(Unterschrift)

Englische Fassung:

STATUTORY DECLARATION

I declare that I have authored this thesis independently, that I have not used other than the declared sources / resources, and that I have explicitly marked all material which has been quoted either literally or by content from the used sources.

…… ……..

date (signature)

Acknowledgement

I would like to express my deep gratitude to the head of the Institute for Chemistry and Technology of Materials, Prof. Dipl.-Ing. Dr. techn. Franz Stelzer, for giving me the possibility to write this doctoral thesis and for his excellent guidance, leadership and support during the last years.

My special thanks are extended to Dipl.-Ing. Dr. techn. Stefan Koller for the excellent collaboration within the NanoPoLiBat project, his great collegiality, for his helpful advices and for all the fruitful discussions.

I am particularly grateful to have the great opportunity to work in such an extraordinary working environment with such amazing colleagues and friends. That`s why a special thanks goes to: Dipl.-Ing. Christoph Stangl, Dipl.-Ing. Harald Kren, Dipl.-Ing. Colin God, Dipl.-Ing. Cornelia Bayer, Dipl.-Ing. Dr. Martin Schmuck, Dipl.-Ing. Bsc. Michaela Scharfegger, Dipl.-Ing. Bsc. Laura Kaltenböck Andrea Droisner and Dipl. -Ing. Lucas Hauser.

Furthermore I would like to thank the European Commision for the financial support under contract STRP 033195 (NanoPoLiBat, Nanotechnology for advanced) and also the VARTA Micro Innovation GmbH for the opportunity to finish my work.

I want to acknowledge the Austrian Center for Electron Microscopy and Nanoanalysis FELMI-ZFE for TEM sample preparation and imaging.

Thanks to the scientific and non scientific staff members of the ICTM, TU Graz. They gave me an unconditional support and made my life much easier.

I would particularly thank my partner Verena for her understanding and support during my study. Without her guidance this work would not have been possible in this way.

Finally, I feel deeply grateful to my parents for their great support over all these years. I just want to say: Thank you!

Abstract

Today lithium-ion batteries represent the system of choice for energy intense mobile application such as smart phones, laptops and other consumer electronic devices. Rising requirements on the energy storage systems are caused by the high energy demand of today's electronic devices. Due to this reason the storage of more lithium ions in the same volume and with a lower weight of the host material is one of the most important challenges today and also in future.

Presently graphite or other carbonaceous materials are the most common active masses for negative electrodes in lithium-ion batteries. The theoretical capacity of the LiC_6 compound (372 $mAh \cdot g^{-1}$) is quite poor compared to those that are accessible with binary lithium intermetallic phases, like $Li_{22}Si_5$, with a theoretical capacity of 4200 $mAh \cdot g^{-1}$. Unfortunately the high capacity of the Si/Li-intermetallic phases is accompanied with high volume changes during lithium insertion and extraction, whereas the difference in volume of the unlithiated silicon and the fully lithiated $Li_{22}Si_5$ phase is about 300%. As a result of the highly ionic character of the formed zintl phases they are very brittle, so that the mechanical stress resulting from the high volume changes causes a rapid decay of the structural stability of the host material. A consequence of the cracking and disintegration of the active material is the loss of contact to the ionic and electric conducting electrode environment coming along with a large capacity fading of such electrodes.

This doctoral thesis aims to overcome the current limitations in specific energy by the use of silicon as active material in lithium ion batteries. Therefore a new way to produce a graphite/silicon composite material as anode material for high capacity lithium ion batteries using a gelatinous silicon compound, formed from cyclopentasilane (CPS), as precursor, was investigated. The novel layered design of this active material provides an excellent cycling stability, rate capability and coulombic efficiency.

Continuative, efficiency problems, their reasons and the consequences for the implementation of silicon in lithium ion batteries will be discussed. Additionally the effect of mechanical electrode stabilization and enhanced conductivity on cycle life and efficiency, as well as the poor coulombic efficiencies, caused by the use of nano-particles in silicon/graphite composite materials were investigated and compared to the introduced new composite material. In the last chapter the alternative of a high capacity anode, containing germanium as active material, for lithium ion batteries will be examined and discussed.

Kurzfassung

Heutzutage stellen Lithium-Ionen-Batterien für energieintensive mobile Anwendungen wie Smartphones, Laptops und andere Geräte der Unterhaltungselektronik das System der Wahl dar. Durch den immer höheren Energiebedarf, von zunehmend ausgereifteren Geräten, ist es notwendig geworden Speichersysteme mit höherer spezifischer Energie ($Wh \cdot kg^{-1}$) und Energiedichte ($Wh \cdot l^{-1}$) zu entwickeln.

Derzeit sind Grafite oder andere kohlenstoffhaltige Materialien die gebräuchlichsten aktiven Massen für negative Elektroden in Lithium-Ionen-Batterien. Die theoretische Kapazität der LiC_6 Grenzphase (372 $mAh \cdot g^{-1}$) ist im Gegensatz zu der theoretischen Speicherkapazität von Silizium, mit einer theoretischen Kapazität von 4200 $mAh \cdot g^{-1}$ ($Li_{22}Si_5$), gering. Leider ist die hohe Kapazität dieser intermetallischen Phasen mit hohen Volumsänderungen (bis zu 300%) während des Lithiierungs- und Delithierungvorganges versehen. Als Folge des stark ionischen Charakters der gebildeten Zintl-Phasen sind diese ausgebildeten Phasen sehr spröde. Daher führen die auftretenden hohen mechanischen Belastungen aufgrund der Volumsausdehnungen zu einem schnellen mechanischen Abbau des Trägermaterials. Diese Pulverisierung und Desintegration der Aktivmaterialteilchen bedeutet gleichzeitig einen Kontaktverlust zu der ionischen und elektrisch leitenden Elektrodenumgebung und resultiert somit in einem großen Kapazitätsverlust.

Das Ziel dieser Arbeit stellte die Überwindung der derzeitigen Limitierungen bei der Verwendung von Silizium als Anodenaktivmaterial dar. Im Zuge dieser Aufgabenstellung wurde ein neuartiges Grafit/Silizium-Verbundmaterial entwickelt, welches eine hervorragende Zyklenstabilität, Ratenfähigkeit und coulometrische Effizienz aufweist. Das neuartige Design des Materials (Schichstruktur), welches für das ausgezeichnete elektrochemische Verhalten verantwortlich ist, konnte erst durch die gleichzeitige Entwicklung eines neuen Produktionsprozesses erzielt werden.

Weiters wurden im Zuge dieser Arbeit Effizienzprobleme, ihre Ursachen und die Folgen für die Anwendung von Silizium in Lithium-Ionen-Batterien diskutiert. Auch die Auswirkungen einer mechanischen Stabilisierung der Elektrode, die in einer verbesserte Leitfähigkeit, erhöhten Zyklenlebensdauer und Effizienz resultierte, wurden untersucht. Des Weiteren wurden die Hintergründe schlechter Effizienz beim Einsatz von Siliziumnanopartikeln beforscht und mit dem neuenartigen Si/C Kompositmaterial mit verringerter Oberfläche verglichen. Im Schlusskapitel wurde die Möglichkeit des Einsatzes von Germaniumpartikeln als Anodenaktivmaterial untersucht und diskutiert.

1 Introduction

The storage of electrical energy will become one of the most important fields of interest in future, either as energy supply for mobile electrical devices, or as energy storage systems for solar and wind energy or in the automotive sector. Hybrid and electric vehicles are one of the most promising candidates to decrease the traffic-related CO_2-emissions. Thus it is hardly surprising that the market for rechargeable batteries is growing rapidly (see Figure 1).

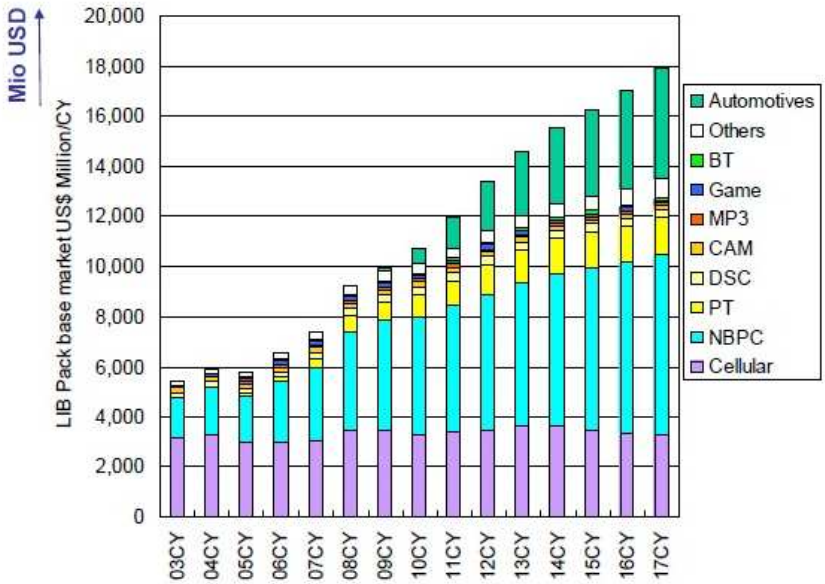

Figure 1: Market for rechargeable batteries splitted after application (1)

Together with the growing market for rechargeable batteries, higher requirements on the energy storage systems are caused by the high energy demand of todays electronic devices. These requirements are not only high energy and power densities, also a long lifetime, safety and low costs are key factors for their use. All these requirements delimitate the possible choices for energy storage systems massively. In Figure 2 (Ragone-Plot from different battery systems) many different battery systems are compared in terms of their specific power and energy. The specific power and also the specific energy are determined by the storage mechanism of the different systems. Due to the reason of the variety of materials, which can be used in LIBs, they can be designed as high power or as well as high energy systems. Compared to other systems it is obvious that LIBs are the only energy storage system, which can be applied in such a wide range and are able to fulfil all the demands which are required by the mentioned applications.

For this reason the European Commission published in 2001 the report “Future Needs and Challenges for Non-Nuclear Energy Research in the European Union”(2), where the lithium ion battery technology was described as one of the key enabling technologies in the area of energy storage.

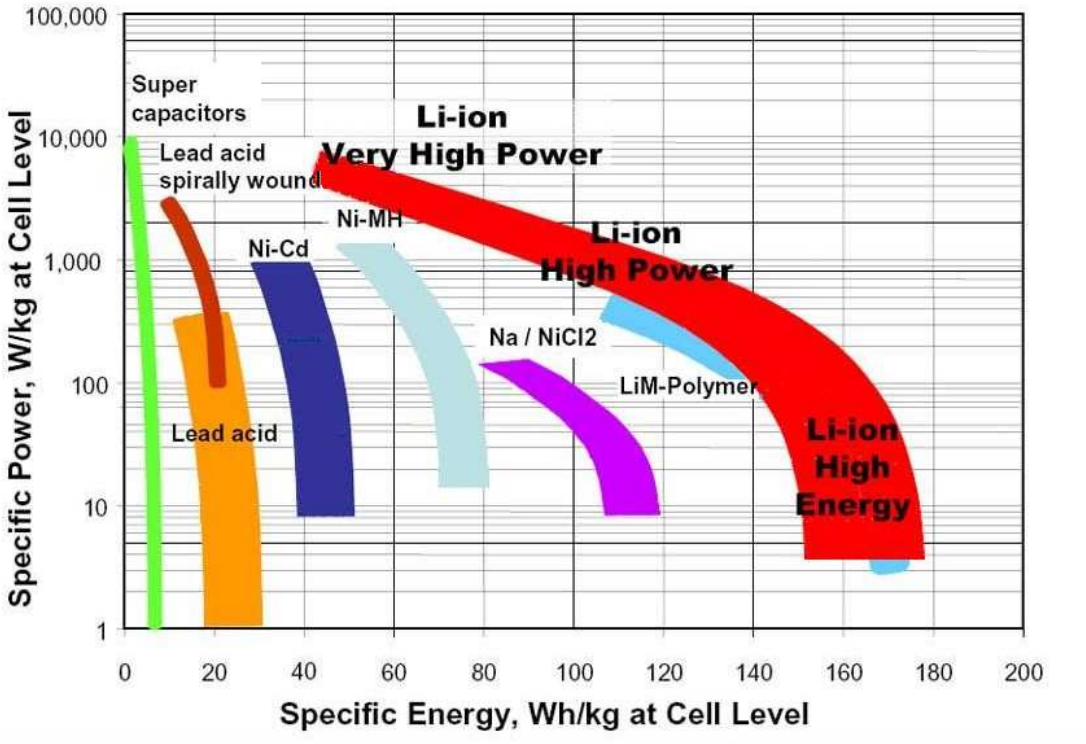

Figure 2: Ragone-Plot from different battery systems (source: SAFT)

The improvements in terms of specific energy ($Wh \cdot kg^{-1}$) and energy density ($Wh \cdot l^{-1}$) that were made since the market introduction of LIBs, mainly were achieved by improvements of the cell design. For the future further large improvements cannot be expected by developments on the cell design. There is a strong need to change the chemistry of the cell to overcome the current limitations.

Given by the physical fact that electrical energy is determined by the potential and by the capacity (Equation 1) there are two possible ways to increase the energy in a lithium ion battery. One possibility is to increase the cell potential and the second possibility is to use materials with higher specific capacities.

$$E_{el} = U \cdot I \cdot t$$

Equation 1

E_{el}... electrical energy

U... potential [V]

I... current [A]

t... time [h]

In Figure 3 are many possibilities of future cathode and anode materials shown, whereat on the cathode side F_2, due to its chemical nature, is not taken into consideration at the moment. For the use of O_2 as cathode in Li-Air batteries many efforts will be spent at the moment to implement such a cathode in rechargeable lithium batteries, but there are many technical and chemical problems which have to be overcome in the next decades.

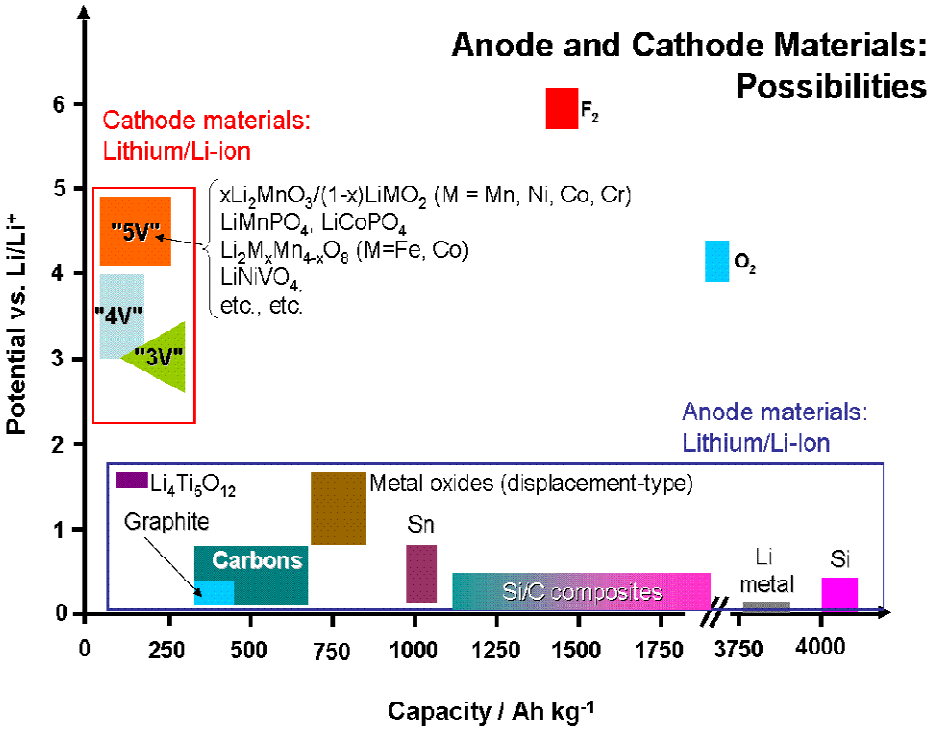

Figure 3: Possible future anode and cathode materials(3)

In next year's there is no promising high capacity cathode material for the implementation in lithium ion batteries in sight. The only way to increase the specific energy of the battery is the use of 5V cathode materials. An example for such a high volt cathode material is a modification of the well investigated spinel structured $LiMn_2O_4$, with a general composition $LiM_xMn_{2-x}O_4$(4) (M= a transition metal element). With an average discharge voltage of 4.7 V and a specific discharge capacity of

140 mAh·g^{-1} the use of such a cathode material leads to a theoretical specific energy of ~470 Wh·kg^{-1} in combination with a common graphite electrode.

On the anode side the use of high capacity materials, like silicon/graphite composites, seems to be an appropriate way to increase the specific energy. It is easy to quantify the advantage of anode materials with higher capacities. The relationship between the total capacities of the electrode materials (anode + cathode) and the specific capacity of the anode is quite simple (5).

$$C_{total} = \frac{C_C}{1 + \frac{C_C}{C_A}} = \frac{C_C \cdot C_A}{C_C + C_A}$$

Equation 2

C_{total}... total specific capacity

C_C... specific cathode capacity

C_A... specific anode capacity

For a given specific cathode capacity, the total specific capacity does not increase linearly (Figure 4). It is also obvious that the increase of the total capacity strongly depends on the value of the specific cathode capacity. The most noticeable improvement of the total capacity can be done when the carbonaceous anode can be replaced by a high capacity anode material, like a silicon-based composite anode, with a specific capacity of 1200 mAh·g^{-1} (Figure 4).

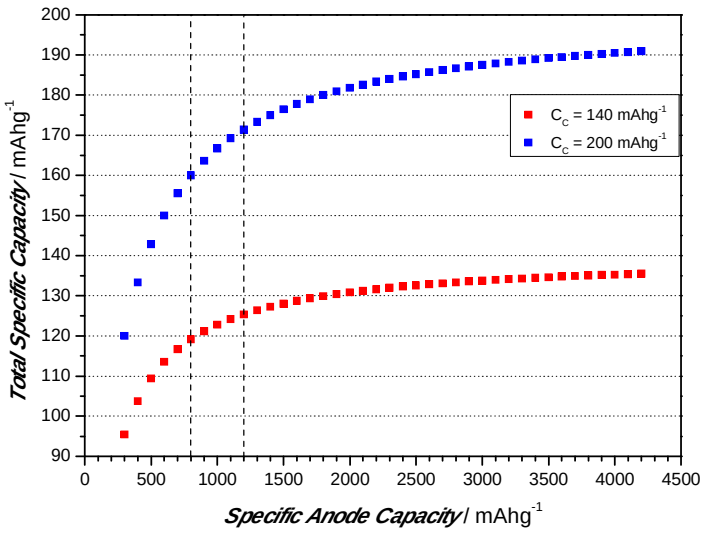

Figure 4: Total capacity, presented as a function of the anode capacity(5)

Nowadays alloy materials start to replace graphite as the negative electrode in lithium ion batteries. A nanostructured composite material consisting of tin, cobalt and carbon were commercialized by Sony in 2005 (Nexelion^{TM}) (6). Compared to tin, with a theoretical capacity of 993 mAh g^{-1} ($Li_{4.4}Sn$), the silicon intermetallic compound has a 4 times larger theoretical capacity ($Li_{4.4}Si$, 4200 mAh g^{-1}). In both cases the intercalation of lithium leads to a large volume expansion during the electrochemical formation of the intermetallic compound. This large volume change, together with the brittleness of the intermetallic compound, leads to cracking and pulverization of the particles and results in a reduced lifetime of such electrodes.

In the last decades many efforts were made to overcome these problems and to enhance the cycle life and stability of these electrodes. Based on the research on tin and silicon based anode materials at TU Graz since 1993, in this doctoral thesis the development and investigation of a new silicon/graphite composite material with a novel layered structured design will be discussed. Also a new production process using a gelatinous silicon compound, formed from CPS, as precursor for the preparation of this active material will be shown. The novel design of this composite material provides an excellent cycling stability, rate capability and coulombic efficiency.

Further, efficiency problems, their reasons and the consequences for the implementation of silicon in lithium ion batteries will be discussed. Also the effect of mechanical electrode stabilization and enhanced conductivity on cycle life and efficiency will be shown. Additionally the poor coulombic efficiencies, caused by the use of nano-particles in silicon/graphite composite materials will be examined and compared to the introduced new composite material. In the closing chapter the alternative of a high capacity anode containing germanium as active material for lithium ion batteries will be examined and discussed.

2 Theoretical Aspects

2.1 Thermodynamic Fundamentals

The build up and the very basic principle of a galvanic cell were not changed since Luigi Galvani (7). For the conversion of chemical energy into electrical energy two different spatial separated electrodes (most often a metal) are dipped into an electrolyte solution. These two electrodes are connected by an internal salt bridge or porous membrane and an external circuit. In Figure 5 a schematic build up of a galvanic cell (Daniell element) is shown.

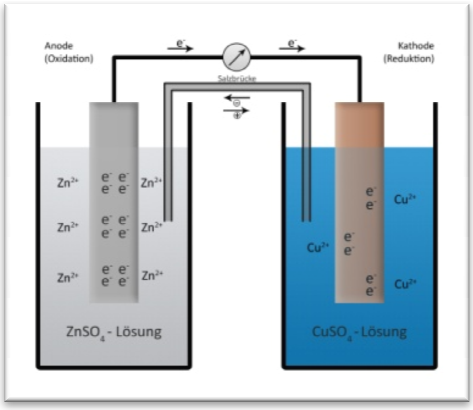

Figure 5: Schematic build up of a Daniell element (8)

The Daniell element is a historical example for a galvanic cell, which was developed by John Fredric Daniell in 1836. It consists of a zinc-stick, which is dipped in an aqueous zinc-salt solution, on the one side, and a copper-stick, which is dipped in an aqueous copper-salt solution, on the other side. Both half-cells are connected by a salt bridge (saturated KCl or NH_4NO_3) or by a diaphragm to ensure charge equilibrium during discharge.

Half cell reactions of the Daniell element:

Anode: oxidation of Zinc $$\boldsymbol{Zn \rightarrow Zn^{2+} + 2\,e^-}$$

Equation 3

Cathode: reduction of Copper $$\boldsymbol{Cu^{2+} + 2e^- \rightarrow Cu}$$

Equation 4

The potential can be calculated by the difference between the two half cells potentials.

$$\Delta \boldsymbol{E} = \boldsymbol{E_{cathode}} - \boldsymbol{E_{anode}}$$

Equation 5

Under standard conditions (temperature 298 K, concentration 1 $mol \cdot L^{-1}$, pressure 1 atm) the half cell potential correlates to the standard potential.

E_{Anode} = -0,76 V

$E_{cathode}$ = 0,34 V

$$\Delta \boldsymbol{E} = \boldsymbol{E_{cathode}} - \boldsymbol{E_{anode}} = \boldsymbol{E_{copper}} - \boldsymbol{E_{zinc}} = \mathbf{1,10\ V}$$

Equation 6

The correlation of the electromotive force and of the free reaction enthalpy (Gibbs free energy) of the cell reaction is given by:

$$\Delta_R \boldsymbol{G} = -\boldsymbol{z} \cdot \boldsymbol{F} \cdot \Delta \boldsymbol{E}$$

Equation 7

$\Delta_R G$… free reaction enthalpy

F... Faraday-constant, F = 96485.33 [C / mol]

z… number of transferred electrons

ΔE… electromotive force

For the cell reaction of the Daniell element $\Delta_R G$ is negative, which means that the occurring process is voluntary. As long as the chemical equilibrium is not achieved, electrical work can be done. The maximum work, which can be done depends on the potential difference between the electrodes and is equal to the Gibbs free energy (at constant temperature and pressure).

$$\boldsymbol{W_{E,max}} = \Delta_R \boldsymbol{G}$$

Equation 8

$W_{E,max}$… maximum work

For a chemical process, where k substances A_1 to A_k are involved,

$$\boldsymbol{v_1 A_1 + \ v_2 A_2 + \ \ldots \rightarrow \ldots + v_{k-1} A_{k-1} + \ v_k A_k}$$

Equation 9

the change of the Gibbs free energy is

$$\boldsymbol{\Delta_R G = \Delta_R G^{\theta} + \ RT \ln Q} \qquad \boldsymbol{with \ \ Q = \prod_{j=1}^{k} (a_j)^{v_j}}$$

Equation 10

$\Delta_R G$... free reaction enthalpy

$\Delta_R G^{\theta}$... standard free reaction enthalpy

R... Ideal gas constant, R = 8.314472 [J / mol K]

T... temperature [K]

a_j... standard activity drawn to the activity of substance j

v_j... stoichiometric coefficient of the substance j in the reaction equation

By dividing both sides by (*-z F*)

$$\boldsymbol{E = \ - \frac{\Delta_R G^{\theta}}{z\,F} - \frac{R\,T}{z\,F} \ln \prod_{j=1}^{k} (a_j)^{v_j}}$$

Equation 11

can be obtained. The first term on the right side is the standard cell potential, which is

$$\boldsymbol{\Delta_R G^{\theta} = \ - z \cdot F \cdot E^{\theta}}$$

Equation 12

The standard cell potential is the free standard enthalpy of the cell reaction, expressed in form of a potential (V), which follows to the common Nernst equation

$$\boldsymbol{E = \ E^{\theta} - \frac{RT}{z \cdot F} \ln \prod_{j=1}^{k} (a_j)^{v_j}}$$

Equation 13

In the special case of a redox reaction, the Nernst equation describes the dependence of the concentration of the electrode potential of a redox couple.

$$E = E^{\theta} + \frac{RT}{z \cdot F} \ln \frac{a_{ox}}{a_{red}}$$

Equation 14

E… potential difference, respectivily electric potential [V]

E^{θ}... standard potential [V]

T… temperature [K]

a… activity of the respective redox-partner

F... Faraday-constant, F = 96485.33 [C / mol]

R... Ideal gas constant, R = 8.314472 [J / mol K]

z… number of transferred electrons

Each combination of two electrodes is called a galvanic element. Because of the Nernst equation it is possible to combine the electrical parameter voltage (respectively electrode potential) with the chemical parameter concentration. Basically the Nernst equation is only legal for cells without mass transport and currentless procedures, but it is an initial point for the derivation of equations in systems with a current flow.

As shown before the potential of the electrode surface is determined by Nernst equation. If an equilibrium exists, the currents in anodic and cathodic directions are equal. If these are related to an electrode area they are called exchange current densities (j_0, unit: $mA \cdot cm^{-2}$).

$$j_a = | j_c | = j_0$$

Equation 15

j_a... anodic current density

j_c... cathodic current density

j_0... exchange current density

If a current flows, a potential drop down can be measured. This decay in the potential is called overpotential η (9). So the real potential is the difference between E^{θ} and the sum of the overpotentials.

$$E_{real} = E^{\theta} - \sum | \eta |$$

Equation 16

The sum of the overpotentials should be as small as possible because they lower the usable energy of the system.

On the basis of the origin of the overpotentials, a distinction has to be made between a few different types.(10) (11).

Charge-Transfer overpotential:

The charge-transfer over potential is caused by the nature of the substances that are reacting, the conditions in the electrolyte, and the characteristics of the electrode. All these factors result in a limitation on the speed of the charge transfer through the phase boundary electrode/electrolyte. The mathematical formula, which deals with this form of overpotential is the Butler-Volmer equation [Equation 17] (12).

The exact mechanism of the lithium-ion transfer through the electrode/electrolyte phase boundary in lithium ion batteries is, in contrast to common metal electrodes, not fully understood. Therefore a mathematical description by the Butler-Volmer equation is difficult.

$$\boldsymbol{I = A * i_0 * \left\{ exp\left[\frac{(1-\alpha) * z * F}{R * T} * (E - E_0)\right] - exp\left[-\frac{\alpha * z * F}{R * T} * (E - E_0)\right]\right\}}$$

Equation 17

I... electrode current [A]

A... electrochemical reactive surface area [m^2]

i_0... exchange current density [$A \cdot m^{-2}$]

E... electrode potential [V]

E_0... electrode potential in equilibrium [V]

T... temperature [K]

z... number of transferred for reaction

F... Faraday constant F = 96485.33 [C / mol]

R... Ideal gas constant, R = 8.314472 [J / mol K]

α... symmetry factor, dimensionless

Diffusion overpotential:

When a high current density exists at the electrode/electrolyte boundary, a depletion of the reacting substance is possible, so that the reaction kinetic is only determined by the diffusion process through this zone (Nernst layer) (10). The generated diffusion overpotential can be described by following formula (with j_{limit} as the maximum current density):

$$\eta_{diff} = \frac{RT}{zF}\ln(1 - \frac{j}{j_{limit}})$$

Equation 18

Reaction overpotential:

The charge transfer and the diffusion overpotential are both of higher importance, but sometimes it is possible that other phenomena, such as adsorption or desorption, limit the reaction kinetics. For this reason the reaction overpotential is mentioned here (10).

Crystallization overpotential:

The reason for the crystallization overpotential is the inhibited intercalation of metal ions in their lattice. By charging of secondary batteries this overpotential is of fundamental importance especially during metal deposition on the negative side. (10)

2.2 Mass Transport in Lithium Ion Batteries

The fundamental principle of lithium ion batteries is based on the charge carrier transport in form of solvated lithium ions in an electrolyte between two electrodes. The electrolyte consists of a solution of a lithium salt in an organic solvent. The two electrodes are able to store lithium ions at different potentials. In the charge reaction the lithium ions, which are embedded in the solid phase of the positive electrode, get extracted and are transported through the electrolyte to the negative electrode. During the extraction of the lithium ions from the positive electrode, the host material gets oxidized. At the negative electrode the lithium ions get inserted in a host matrix and as a consequence the host matrix gets reduced. Therefore the lithium ions do not represent the redox active species in a lithium ion battery. In Figure 6 the schematic drawing of a lithium ion battery is shown with graphite as negative electrode and $LiCoO_2$ as positive electrode.

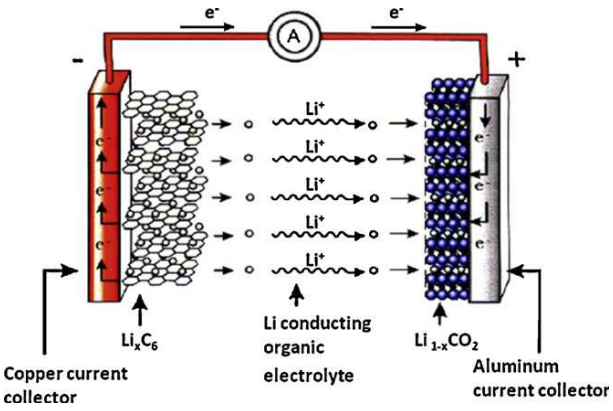

Figure 6: Scheme of a common lithium ion battery(13)

Reaction at the positive electrode:

$$LiCoO_2 \underset{\text{discharge}}{\overset{\text{charge}}{\rightleftharpoons}} 0.5\ Li^+ + 0.5\ e^- + Li_{0.5}CoO_2$$

Equation 19

Reaction at the negative electrode:

$$Li^+ + C_6 + e^- \underset{\text{discharge}}{\overset{\text{charge}}{\rightleftharpoons}} LiC_6$$

Equation 20

Overall cell reaction:

$$2\ LiCoO_2 + C_6 \underset{\text{discharge}}{\overset{\text{charge}}{\rightleftharpoons}} LiC_6 + 2\ Li_{0.5}CoO_2$$

Equation 21

2.2.1 Decisive Mass Transport steps in Lithium Ion Batteries

As previously specified the Nernst equation is only valid for systems without mass transport. But this parameter is, like shown before, one of the basis principles of a lithium ion battery, so an elementary understanding of the transport mechanism in lithium ion batteries is essential. Like for any other battery system, the principle mass transport in a lithium ion battery is based on three different transport mechanismn (14) (Figure 7).

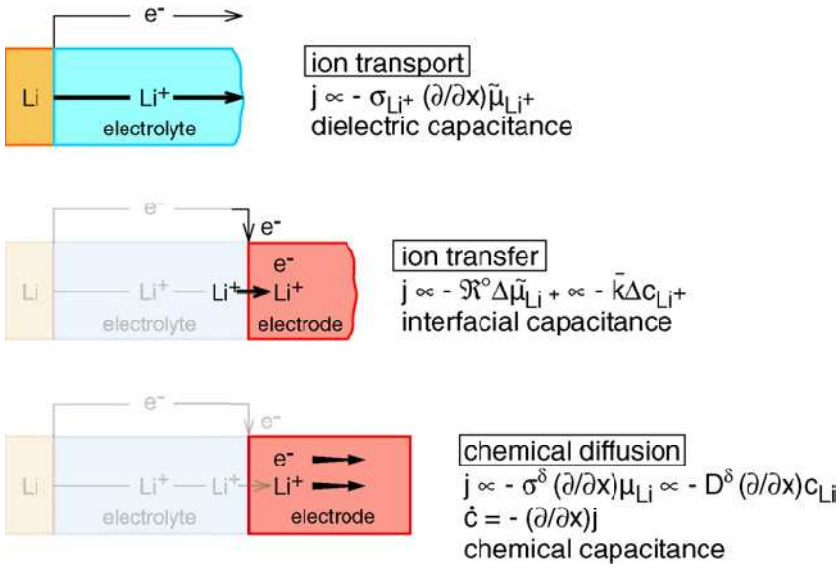

Figure 7: The three mechanism of mass transport in lithium ion batteries (14)

Transport through the electrolyte:

The lithium ion transport through the electrolyte does not violate the condition of electroneutrality when the charge carrying is compensated by an electron flow over an extern circuit. Transient phenomena in the electrolyte typically occur within nanoseconds and are from dielectric nature Therefore the transport is in principle a steady state process, driven by gradients in the electrochemical potential of the ion (μ), the transport coefficient being the lithium ion conductivity.

Lithium transfer through the electrolyte/electrode boundary:

The driving force for the lithium ion transfer through the electrolyte/electrode boundary is given by the gradient of μ_{Li+} on both sides. The respective transport coefficient is determined by the charge carrier exchange rate. Approximately equilibrium should prevail otherwise this process has needs to be described by electrochemical kinetics.

Lithium storage process:

The storage process occurs within microseconds and is characterized by the interfacial capacitance. The time dependence plays a role when the chemical diffusion of lithium ions and electrons are necessary for the storage of lithium. The driving force is the gradient of the chemical potential of lithium (Equation 22) as well as the ambipolar conductivity (Equation 23), which are both influenced by the lithium ion as well as by the electron.

$$\frac{\partial}{\partial x}\mu_{Li} = \frac{\partial}{\partial x}(\mu_{Li^+} + \mu_{e^-})$$

Equation 22

$$\sigma^{\delta} = ((\sigma_{e^-}^{-1} + \sigma_{Li^+}^{-1})^{-1})$$

Equation 23

Through expression of the driving force by the terms of the Lithium concentration gradients ((∂ / ∂ x)c_{Li}), the transport coefficient becomes the chemical diffusion coefficient D^{δ}. Additionally to σ^{δ} the chemical diffusion coefficient includes the chemical capacitance C^{δ}.

Although in a real system much more parameters are involved (e.g. protection layers, etc.), these three transport mechanism are considered as the major ones for transport (14).

2.2.2 Carbonaceous Materials

Nowadays graphite or other carbonaceous materials are the most used active materials for the negative electrode in lithium ion batteries. Lithium ions can be reversibly intercalated and extracted in carbonaceous materials during charging and discharging. The reaction is described by the equation below:

$$C_n + xLi + xe^- \leftrightharpoons Li_xC_n$$

Equation 24

The type of carbon influences the electrochemical behaviour and therefore the characteristics of the current/potential curve. A basic categorisation can be done into graphitic (ordered) carbons and non graphitic (disordered) carbons. From the crystallographic point of view the term “graphite” is only applicable for carbon materials with a layered lattice structure and a perfect stacking order of the graphene layers, either in the predominant AB structure or the in less common ABC structure (rhombohedral graphite). For the transformation of AB into ABC stacking only a small amount of energy is required, but typically only five percent of the graphene layers in natural graphite are arranged rhombohedrally (10).

Usually the ideal graphite structure is not given for practical carbonaceous materials. So the terms “natural”, “artificial” or “synthetic” and “pyrolytic” graphite are commonly used, although the materials are polycrystalline (15).

When the disorder in the structure becomes more dominant, the carbonaceous materials are not longer referred to graphitic carbons and must be denominated as non graphitic carbons. In non-graphitic carbons most of the carbon atoms are arranged in a planar hexagonal network, but the structure is characterized by amorphous areas, in which graphitic (layered) structure segments are embedded (16)(17).

Graphite:

Graphite intercalation compounds (GIC) were known since the 1950´s (18). Graphite is a layered compound and consists of hexagonal sheets of sp^2 – carbons (Figure 8). The ABAB layers are held together by van der Waals forces and change to AAA^{2-} arrangement during the intercalation of lithium into these layers(19).

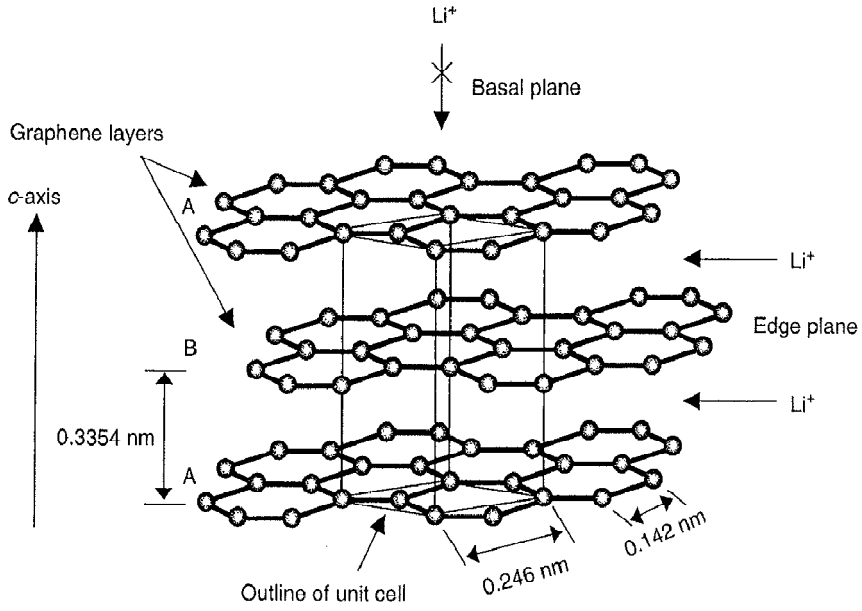

Figure 8: Hexagonal structure of graphite (20)

The structure is resilient enough to compensate a moderate growth of the distance between the layers from 335 pm to 370 pm (10.3%) (21)(22)(23) during lithium intercalation and extraction. During the intercalation of lithium ions into the graphite a stepwise reduction of the graphite takes place and a GIC is formed with a maximum stochiometry of LiC_6 (one lithium atom per 6 carbon atoms)(24)(25). The reason for these staging phenomena is given by thermodynamic causes. To "open" the van der Waals gaps between two layers for the guests entering and to enlarge the space between the layers, energy is required. Repulsive forces between the lithium atoms lead to a more randomized distribution in the host material (10).

The staging phenomena can be described by the stage index "s", which is equal to the number of graphene layers between two nearest guest layers. Because of thermodynamic reasons, noted above, only a few van der Waal gaps are energetically favoured over a random distribution of guests. The degree of lithium-intercalation into graphite can be easily observed during the electrochemical reduction of carbons in Li^+ containing electrolytes. Figure 9 shows a schematic constant current curve (left) and voltammetric curve (right) for the electrochemical formation of lithiated graphite. In the constant current curve the potential plateaus indicate the coexistence of two phases. This two phase regions are indicated by current peaks under potentiodynamic control (Figure 9 right). Four different intercalation compounds can be identified.

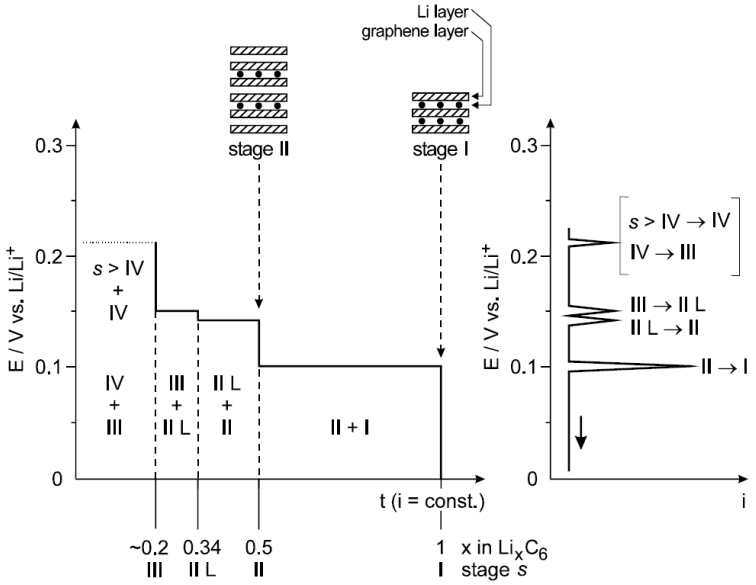

Figure 9: Schematic constant current curve (left) and voltammetric curve (right) for the electrochemical formation of lithiated graphite (26)

The four intercalation compounds (LiC_{30}, LiC_{18}, LiC_{12} and LiC_6) (27), which can be obtained through electrochemical reduction of carbons in Li^+ containing electrolytes or through chemical synthesis (10) (18) (28) (29)(30), were identified and confirmed by X-Ray diffraction (10) (24) (28) (31) (32) and Raman-spectroscopy (33) (34).

Non graphitic carbons:

The preparation of most non graphitic carbons occurs by pyrolysis at temperatures below 1500°C. As precursors organic polymers or hydrocarbon precursors are used. By a further heat treatment at temperatures about 3000°C a differentiation between two different types of non graphitic carbons can be made (hard carbons and soft carbons).

Hard carbon is a non graphitized glass like carbon, which does not graphitize even if it is heat treated at high temperature. The carbon layers are immobilized by strong crosslinking. It is possible to increase the number of crosslinks by using precursors which tend to crosslink or by the use of crosslinking agents such as oxygen(35). The denotation hard carbon is given by the fact that non graphitizing carbons are mechanical harder than the graphitizing ones.

In graphitizing carbons (soft carbons) the structure segments are mobile enough to form graphite like crystallites during the heating process. The crosslinking between the graphite-like crystallites is weak, so it is simple to transform the disorderly stacked carbon layers and graphite crystallites into more ordered (more graphitic) arrangements (27).

In Figure 10 the schematic profiles of soft- and hard carbon and their differences to the schematic profile of graphite are shown.

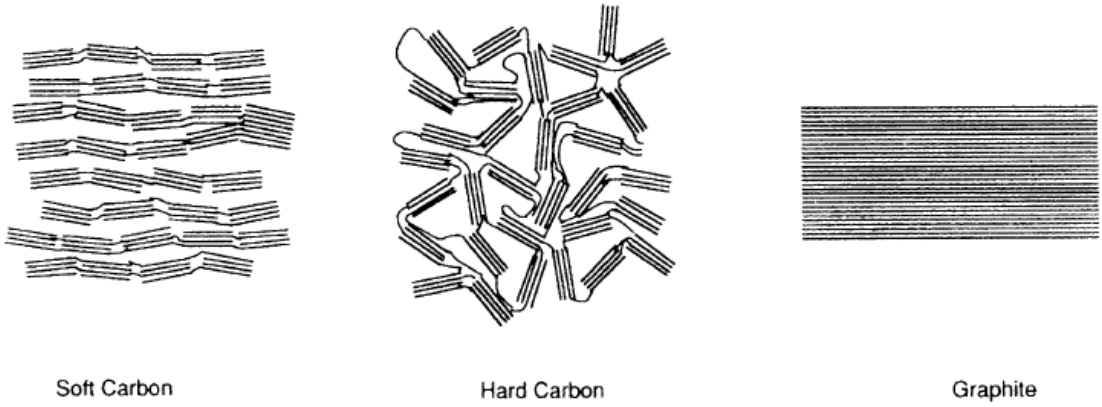

Figure 10: Schematically design of soft carbon, hard carbon and graphite (19)

In Figure 11 the dependence of the heat treatment on the specific capacity of non graphitic carbons is shown. The materials in the three highlighted regions are proposed for the use as active materials in lithium ion batteries.

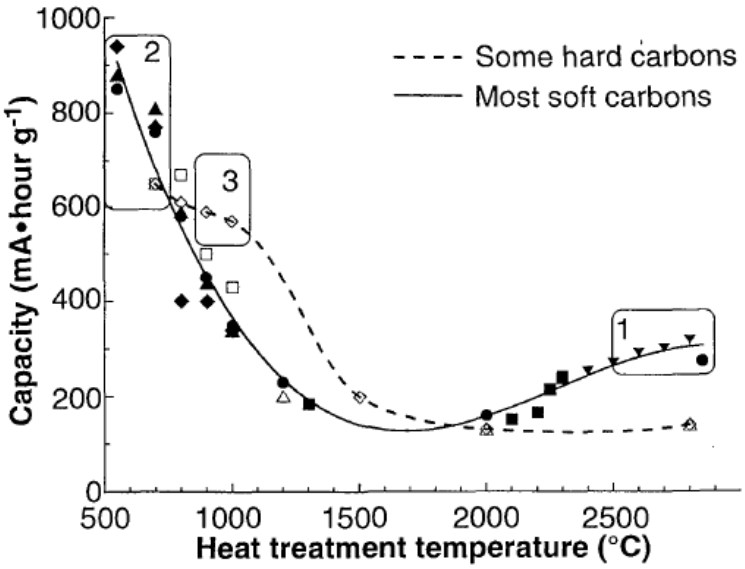

Figure 11: Reversible capacity for hard- and soft carbons versus heat treatment (2nd charge – discharge cycle)(36)

The huge difference in the specific capacities at different temperatures is a result of the structures and chemistry of carbons prepared by heating of organic precursor (36).

As seen before hard carbons offer a higher specific capacity than graphitic carbons. The reason for the higher specific capacity is due to the fact of an adsorption of lithium on the surfaces of the small

graphene sheets. In Figure 12a the scheme of a fully lithiated graphite is shown. When graphite is fully lithiated (next nearest neighbour sites fully occupied) there is one layer of lithium per carbon layer. In hard carbons lithium might be adsorbed on each side of the single layer, which leads to two lithium atoms per six carbon atoms, without requiring lithium atoms to occupy nearest neighbour sites. Figure 12b shows schematically how lithium can be adsorbed in a carbon made up of small single layers.

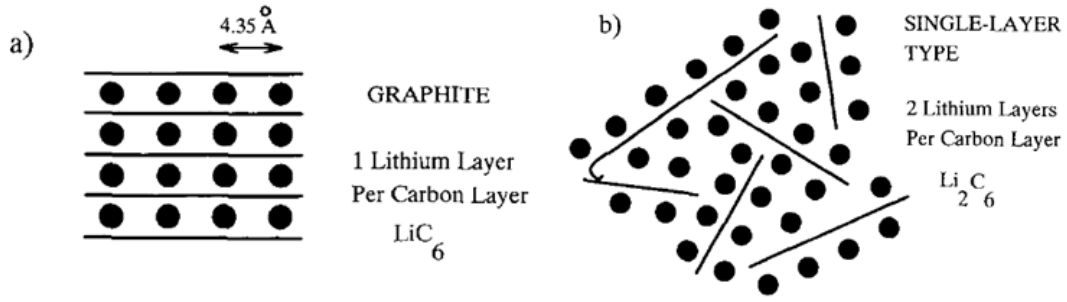

Figure 12: Schematic diagram showing the intercalation of Lithium in a) graphite and b) single layer hard carbon (37)

For the application in lithium ion batteries generally graphite and hard carbons are used.

2.2.3 Lithium Intermetallics

At room temperature lithium is able to form well-defined intermetallic phases (Li_xM) with numerous metals M (M=Mg, Ca, Al, Si, Ge, Sn, Pb, As, Sb, Bi, Pt, Ag, Au, Zn, Cd, Hg) if the metal is polarized to a sufficiently negative potential in a Li^+ containing liquid organic electrolyte (38).

$$Me + x\ Li^+ + x\ e^- \underset{\text{discharge}}{\overset{\text{charge}}{\rightleftharpoons}} MeLi_x$$

Equation 25

Because this process is quite reversible, metals, which can form intermetallic phases with lithium, have found considerable interest for use as materials on the negative electrode side in lithium ion batteries.

The metallic host materials are in analogy to carbonaceous materials also used in the discharged (delithiated) state. The formation of the intermetallic phase and the formation of the solid electrolyte interphase (SEI, see chapter 2.2.4) take place during the first lithiation.

The first systematic work on lithium intermetallics were for their use in high temperature cells (~400°C). In these cells, the lithium intermetallics replaced the metallic lithium electrode because of the low melting point of metallic lithium (180°C) (39) (40) (41) and the therefore related safety problems. At room temperature lithium intermetallics were first used as substrates for the electrodeposition of metallic lithium from Li^+ containing electrolytes (42) (43) . It took a while until the intermetallic phase building phenomena of lithium with the respective metal was identified (38)

From the late `70s to the beginning `90s lithium intermetallics seemed to be the appropriate material to replace metallic lithium in rechargeable lithium cells (44) (45), whereas the performance and safety problem of metallic lithium was the driving force for this research. By the use of graphite and the introduction of the lithium ion batteries on the market the interest on lithium intermetallics decreased. Beginning with the announcement of the Stalion® lithium ion cell (Fuji Photo Film Celltic Co.) in 1996 the situation changed (46). With a higher specific energy and energy density than conventional carbon based lithium ion batteries, the interest on lithium intermetallic compounds as negative electrodes increased rapidly. In this case the carbon anode was substituted by an amorphous tin-based composite oxide and was cycled against a “standard” $LiCoO_2$ cathode.

The lithium packing density (PD_{Li}) in lithium intermetallic compounds is much higher than in graphite intercalation compounds (GIC`s). It is comparable to that of metallic lithium or even slightly higher. It should be mentioned, that lithium is stored in the host material in ionic and not in atomic form. Table 1 gives an overview on the PD_{Li} for some metallic host materials.

Table 1: Lithium packing densities of various lithium intermetallic compounds (38)

Compound	PD_{Li}
	[mol·L^{-1}]
Li	76.36
$Li_{22}Sn_5$	75.74
$Li_{22}Pb_5$	72.17
$Li_{22}Si_5$	88.56

The high lithium packing densities of lithium intermetallic compounds result in much higher theoretic specific charges and charge densities compared to commonly used GIC (LiC_6). They have a similar reductive potential compared to GIC`s, which is close to that of metallic lithium or slightly higher (see Figure 13).

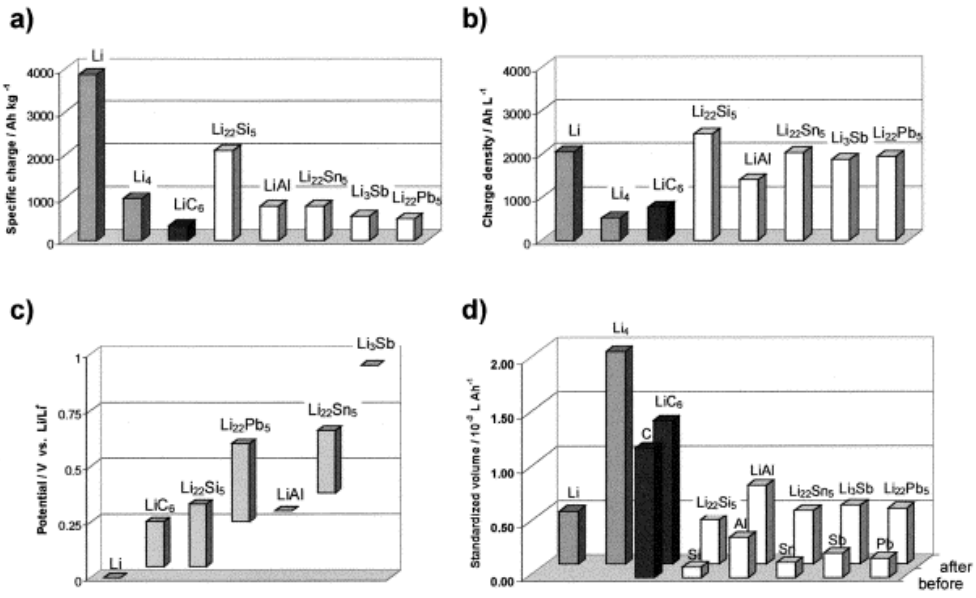

Figure 13: a) Specific charges and (b) charge densities, (c) range of plateau potentials for the lithiation reaction of these anode materials and (d) volumes of these anode materials before and after lithiation (38)

For example the charge density of silicon ($Li_{22}Si_5$) is more than 3 times higher than those of graphite (LiC_6). Not least because of their low costs and their good availability silicon, tin and alumina are the most promising host materials.

Drawbacks of lithium intermetallic compounds:

Although lithium intermetallic compounds have the advantage concerning their higher charge density, today carbonaceous anodes are commonly used in commercial lithium ion batteries. The reasons are large volume and structure changes of the host material during lithium insertion and extraction. During the formation of the intermetallic phase (formation of $Li_x^+M^{x-}$), the host metal has do accept, next to the several mols of lithium ions, also the negative charges. The charge transfer reaction is shown in Equation 26.

$$M^0 + xe^- \leftrightarrow M^{x-}$$

Equation 26

As a consequence of the fact that the M^{x-} ions are larger than the neutral M^0 atoms, the volume differences between the lithiated and lithium-free host material are in the order of 100-300% (see also Figure 13d)(47) (48) (49). The formed lithium intermetallic phases (Li_xM) are of highly ionic character (e.g. formation of a Zintl-phase, $Li_x^+M^{x-}$) and therefore usually quite brittle (50) (51). Combined with the mechanical stress, by reason of the volume changes, a rapid decay of mechanical stability of the electrode occurs. A loss of interparticle contact(52) caused by cracking and pulverization of the particles leads to a typical fail of the electrode after only a few charge/discharge cycles.

So an intelligent electrode or particle design is necessary to overcome the problems of the dimensional instability of these electrodes.

2.2.3.1 Silicon

As already mentioned silicon, with its theoretical capacity of 4200 mAh·g^{-1} ($Li_{22}Si_5$)(53), is a promising candidate for the use as anode material in the next generation of high energy lithium ion batteries. Unfortunately the high capacity of the Si/Li-intermetallic phases is accompanied with high volume changes during lithium insertion and extraction, whereas the difference in volume of the unlithiated silicon and the fully lithiated $Li_{22}Si_5$ phase is about 310% (54). As a consequence of these high volume changes, a cracking and disintegration of the active material particles can be observed. Thereby a loss of contact to the ionic and electric conducting electrode environment occurs and this leads to a large capacity fading (28).

In the last years the research on silicon was intensified to get a deeper understanding of the building of the lithium/silicon intermetallic phases at room temperature and to overcome the dimensional problems of silicon based electrodes. The use of small sized particles (47)(48)(55) and nanomaterials, e.g. nanowires (56) (57), the embedding of the host material into a dimensional stable matrix (38) and the use of Carboxymethylcellulose (CMC) as binder (58) (59) are some approaches to overcome the dimensional problems of such electrodes (more in chapter 2.2.3.3).

In 1981 Huggins et al. identified, by equilibrium coloumbic titration technique, four intermediate phases at a temperature of 420°C for the Li-Si system (60): $Li_{1.71}Si$, $Li_{2.33}Si$, $Li_{3.25}Si$ and $Li_{4.4}Si$.

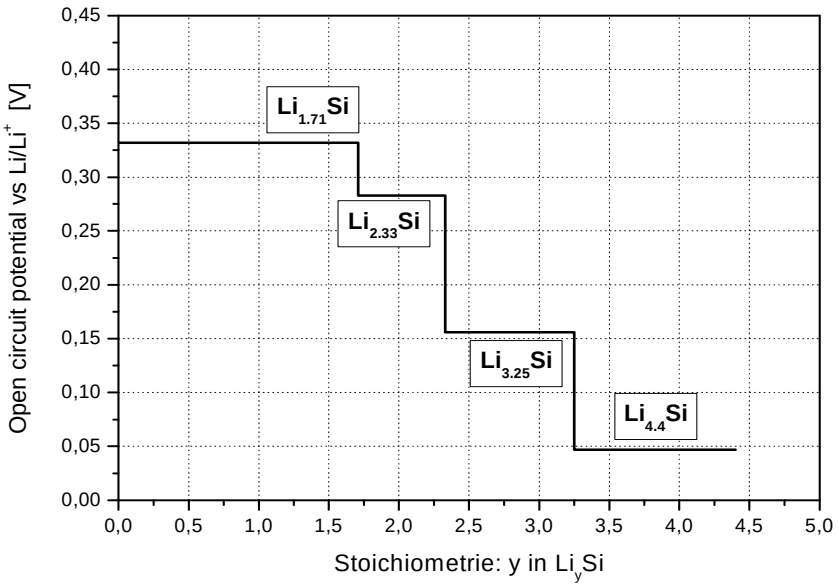

Figure 14: Coloumbic titration curve of the Li-Si system (60)

Because the properties of these four phases are varying in many respects, the binary phase diagram of the Li/Si system will be shown in Figure 15 and some of the chemical and physical properties of the four phases are summarized in Table 2.

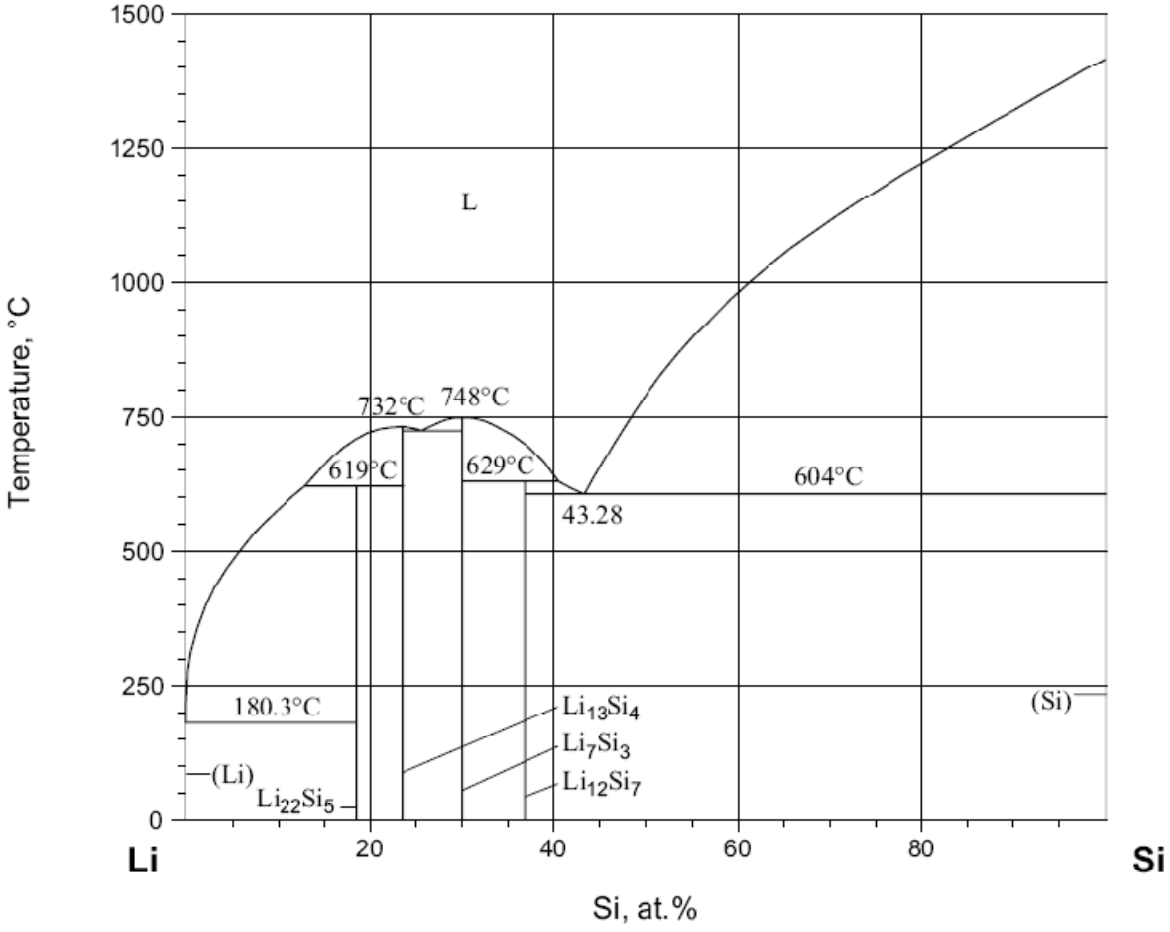

Figure 15: Binary phase diagramm of the Li/Si system (61)

Table 2: Chemical and physical properties of the four intermediated phases for the Li/Si system (at 420°C) (62)

stoichiometry		molar mass	specific capacity excl. Li	potential	crystal structure	density	volume expansion
		[g/mol]	[mAh/g]	[mV vs. Li/Li^+]		[g/cm^3]	[%]
$Li_{12}Si_7$	$Li_{1.71}Si$	40.0	1636	0.332	orthorhombic	1.15	190
Li_7Si_3	$Li_{2.33}Si$	44.3	2227	0.283	Rhombohedral	1.43	158
$Li_{13}Si_4$	$Li_{3.25}Si$	50.6	3101	0.156	Orthorhombic	1.38	206
$Li_{22}Si_5$	$Li_{4.4}Si$	58.6	4199	0.047	cubic	1.18	314

By a view on the physical properties it is easy to distinguish, that a limitation of the state of charge (SOC) can enhance the cycle properties of a silicon electrode during lithiation/delithiation by controlling the volume expansion at the expense of losing capacity.

For a further understanding of the lithiation of silicon at room temperature XRD, High Resolution TEM (HRTEM) and Raman Spektroskopic measurements were done (63) (64) (65).

XRD and HREM measeruments done by Limthongkul et al indicate a different mechanism of the lithiation of crystalline silicon at room temperature compared to the lithiation at high temperatures (64) (66). None of the stable intermediated Li/Si phase found at 420°C were detected at room temperature, instead an amorphization of the silicon was found. It was shown in HRTEM measurement that a crystalline phase coexists next to the lithium containing amorphous phase. By using the Nernst-equation, the Gibbs free energy of the amorphous Li/Si phase was determined and a Gibbs free energy phase diagram of the expected crystalline and amorphous Li/Si phase was constructed (Figure 16).

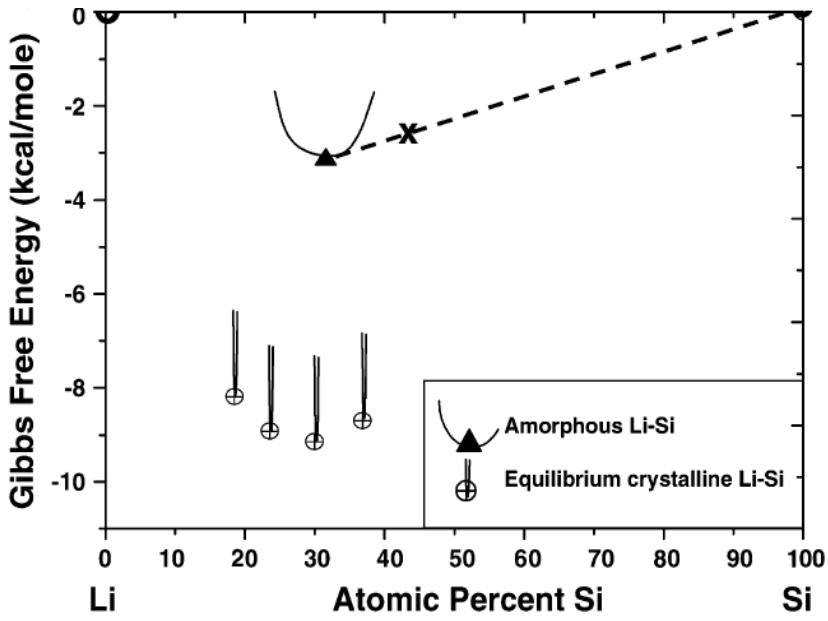

Figure 16: Gibbs free energy phase diagram of amorphous Li/Si and crystalline Li/Si (64)

The four crystalline phases have a lower Gibbs free energy then the amorphous phase. At room temperature crystallization is not possible, so another mechanism to lower the Gibbs free energy has to take place to reach the thermodynamic equilibrium. This is the thermodynamic proof of the building through diffusion of the metastable amorphous phase, which Gibbs free energy is lower. Obrovac et al. and Dahn et al. confirmed these results by ex-situ XRD measurements and showed that the two phase region, which occurs under 50mV vs. Li/Li^+, does not contain the expected $Li_{4.4}Si$

phase but a new $Li_{3.75}Si$ phase (65) (67). Only when the potential gets lowered to 0V vs. Li/Li^+ micro cracks can be observed, whereat the building of these micro cracks will be attributed to the formation of the crystalline $Li_{4.4}Si$ phase. The new metastable phase ($Li_{3.75}Si$) has a specific capacity of 3580 mAh g^{-1}.

In 2010 J.Y. Kwon et al. (68) showed that the formation of the $Li_{3.75}Si$ phase is a function of temperature. Under a temperature of 85°C the $Li_{3.75}Si$ phase appears whereat a temperature over 100°C the formation of a $Li_{4.2}Si$ phase can be observed. The formation of the crystalline $Li_{4.2}Si$ occurs near 0.0V against Li/Li^+, but due to the fact that this crystallization is a slow kinetic reaction the potential must be unexpended a long time.

All these results do not explain the voltage plateaus which indicate two phase regions during galvanostatic experiments (69). So it must be noted there is no consensus about the real formed phases during the lithiation of silicon among scientists. An agreement is only made about the mechanical stress which leads to a bad cycle life, bad reversibility's and agglomeration of nano silicon during cycling.

2.2.3.2 Germanium

As previously delineated there is a large interest in the development of binary lithium intermetallic systems for the application in secondary lithium ion batteries, especially for the tin and silicon systems. The analogues Li_xGe_y system has received only little attention. The fully lithiated $Li_{4.4}Ge$ has a theoretical capacity of 1600 $mAh \cdot g^{-1}$ (70), which is ~40 % compared to the lithiated silicon system. However silicon typically forms a native oxide layer on the surface under air, which reacts during the lithiation to Li_2O and elemental silicon (71). Especially when the silicon is nano sized the native oxide layer accounts a significant fraction of the silicon atom and so there is a large irreversible capacity in the first cycled caused by forming of Li_2O (72). In contrast to silicon, germanium is in air chemical stable and has not the strong affinity to form a native oxide (73). Like other binary lithium intermetallic compounds germanium undergoes also a large volume change (370%) during lithiation/delithiation.

The main advantage of this system is the diffusivity of lithium in germanium which is 400 times higher than the diffusivity of lithium in silicon at room temperature (74). So germanium may be an attractive electrode material for the use in high power lithium ion batteries or as addition to silicon electrodes to increase the lithium diffusivity of such electrodes.

M.R. St. John et al. report that five voltage plateaus were observed by the electrochemical reaction of germanium with lithium at high temperature (360°C – 400°C): LiGe, Li_9Ge_4, $Li_{16}Ge_5$, $Li_{15}Ge_4$ and $Li_{22}Ge_5$ (75).

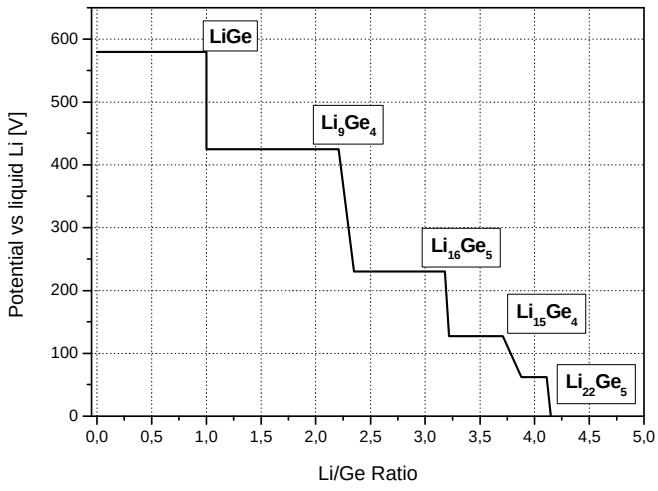

Figure 17: Coloumbic titration curve for the Li/Ge system (400°C)(75)

Analogue to the silicon system, there is not only one real lithiation mechanism for germanium at room temperature. J. Graetz et al. reported many crystalline phases during lithiation of a germanium thin film (73): mainly LiGe, Li_7Ge_2, $Li_{15}Ge_4$, and $Li_{11}Ge_6$, in small quantities Li_9Ge_4, $Li_{22}Ge_5$ and also a small amount of an amorphous phase. Meanwhile S. Yoon et al. delineate Li_9Ge_4, Li_7Ge_2 and a mixture of $Li_{15}Ge_4$ and $Li_{22}Ge_5$ as the main phases during the lithiation of a carbon coated germanium composite electrode (76).

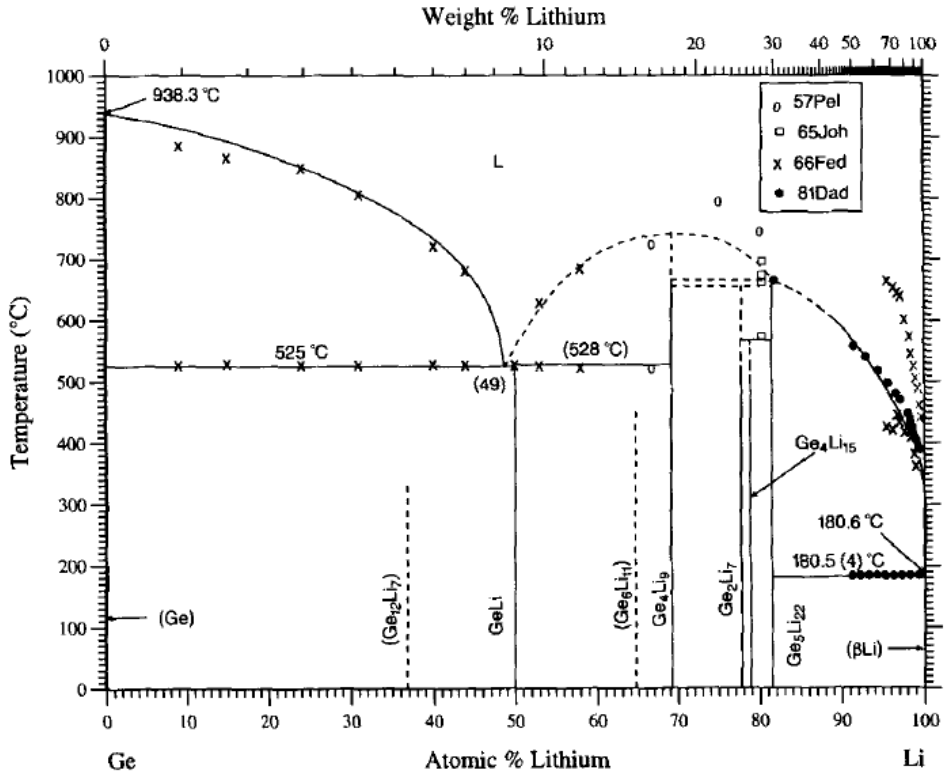

Figure 18: Binary phase diagram of the Li/Ge system (77)

In contrast to the previously referred papers, in the case of lithiation of germanium nanowires mainly the formation of an amorphous phase can be observed similar to the lithiation mechanism of silicon nanowires (70).

For the germanium system the same approaches and concepts for the anode design are usefull to overcome the dimensional problems during lithiation, like small sized particles and nanomaterials, e.g. nanowires, thin film electrodes or the embedding of the host material into a dimensional stable matrix(70)(73) (78) .

2.2.3.3 Concepts for the Anode-Design

Various approaches have been used to overcome the problems concerning the large volume changes and resultant the poor capacity retention and cycle life of these, during lithium insertion/extraction, dimensional unstable materials. Following are the three most promising approaches discussed:

- Use of nano scale particles
- Embedding of the active material in an active or inactive matrix
- Use of special binder-systems

Use of nano scale particles:

The reduction of the particle size into the nano scale area enhances the cycling stability of such formed electrodes significantly. There is a deviant chemistry behaviour of nano sized particles compared to macro sized ones, and so also the deformation, volume expansion and the cracking behaviour is different. The use of small sized particles and their influence on the cycling stability is sufficient reviewed in literature (47) (79).

An electrode prepared by the use of small sized particles offers also a better kinetic because of a homogenous intercalation of the material. There is a concentration gradient in a particle during lithiation because of lithium diffusion in the solid state, which depends on the particle size. Larger particles also have a larger concentration gradient from the surface to the inner of the particle than small particles. By a look on the different volume expansions at different states of lithiation it is obvious that such a concentration gradient leads to more mechanical stress based on different volume expansions from the surface to the inner part of the particle. Therefore less cracks and breaks are expected which will lead to a better cycle stability, and a better cycling efficiency by the cause of less electrolyte decomposition (48) (80).

Embedding of the active material in an active or inactive matrix:

Like shown before, cycling of intermetallic compounds leads to a massive volume expansion, which ends up in pulverization of the electrodes and therefore in a limited cycle life. To counter this large volume changes it is possible to embed the active material particles in a less reactive or inactive matrix. The concept behind this idea is the lowering or buffering of the local volume expansions by a dimensional stable matrix.

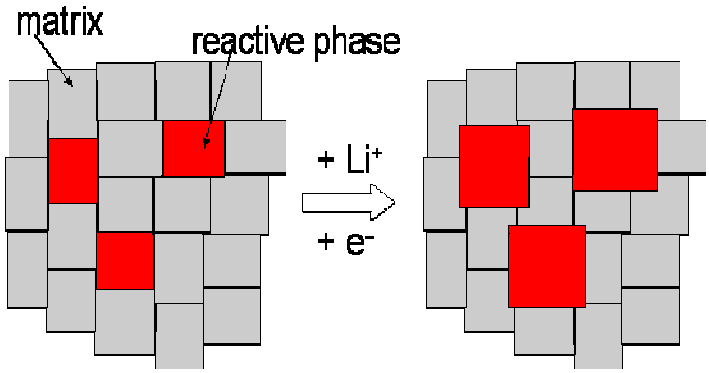

Figure 19: Concept of buffering the volume expansion of a reactive phase (38).

The less or not reactive matrix must have the ability to withstand the large volume changes during cycling, so a high mechanical strength is required. Also a high electronic conductivity is necessary to ensure a fast charge transfer(72).

Winter et al. (38) delineate a way to buffer the volume expansion of a tin/antimony electrode system. Tin and antimony exhibit both a large volume expansion, but feature with different formation potentials of the intermetallic phases. During the formation of the lithium-antimony intermetallic phase, the tin phase acts as stable and electric conductive matrix at this potential. Tin is able to accumulate the local volume expansions coming from this intermetallic phase formation. The formation of the lithium/tin intermetallic phases at a lower potential and the resulting volume expansion can be buffered by the former formed lithium-antimony structure.

From a practical point of view carbon seems to be the ideal matrix material because of its softness, a relatively low density, good electronic conductivity, small volume expansion during lithium insertion/extraction and the ability to store lithium ions as well (72). For the success of such a concept a homogenous distribution of the active material in the matrix is necessary. A difference between the particle sizes of the active- and matrix material is beneficial as well. So a combination of the two former delineated approaches is reasonable. When the active material is in the nano range and the matrix material is in the micrometer range it is possible to build up a 3 dimensional porous structure. In the space between the less reactive matrix particles the volume expansion of the nano sized active material can be buffered, and so the expansion of the whole electrode can be held low.

The best example for practicability of the combination of these two approaches is the commerzialized Nexelion™ battery in 2005.

Influence of the binder system on cycleability:

The electrode performance strongly depends on the binder system. The used binder system should meet various requirements, starting by the electrochemical stability in the applied potential window, chemical inertness against the used organic solvents in the electrolyte system and certainly the warranty of mechanical stability. In terms of energy density of the whole battery it is desirable to reduce all inactive components to a minimum as well as the binder content by keeping the required mechanical stability of the electrode.

In common graphitic carbon electrodes polyvinyledendiflouride (PVdF) is the binder of choice. Due to the fact of different requirements, e.g. to compensate large volume changes, the use of PVdF as binder in intermetallic and intermetallic composite electrodes failed (see Figure 20).

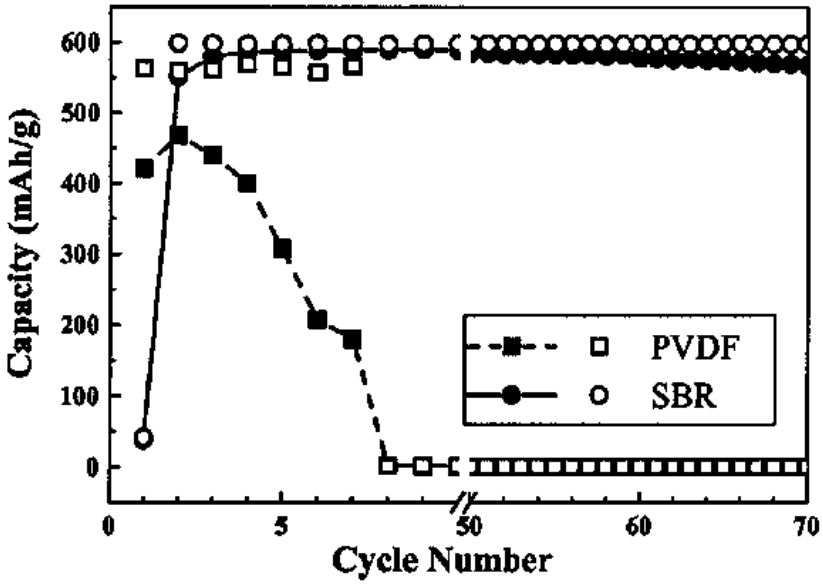

Figure 20: Comparison of the cycling performance of Si/C composite electrodes by the use of different binders (81)

The impact of the binder system on the cycling stability of silicon/graphite composite anodes is very well shown in literature (59) (82).

The water soluble sodium salt of the carboxymethylcellulose (CMC) seems to be the appropriate choice as binder for silicon/graphite and silicon electrodes. Next to an enhanced cycling stability also the electrode processing becomes environmentally friendly, because water can be used as processing solvent instead of organic solvents(59).

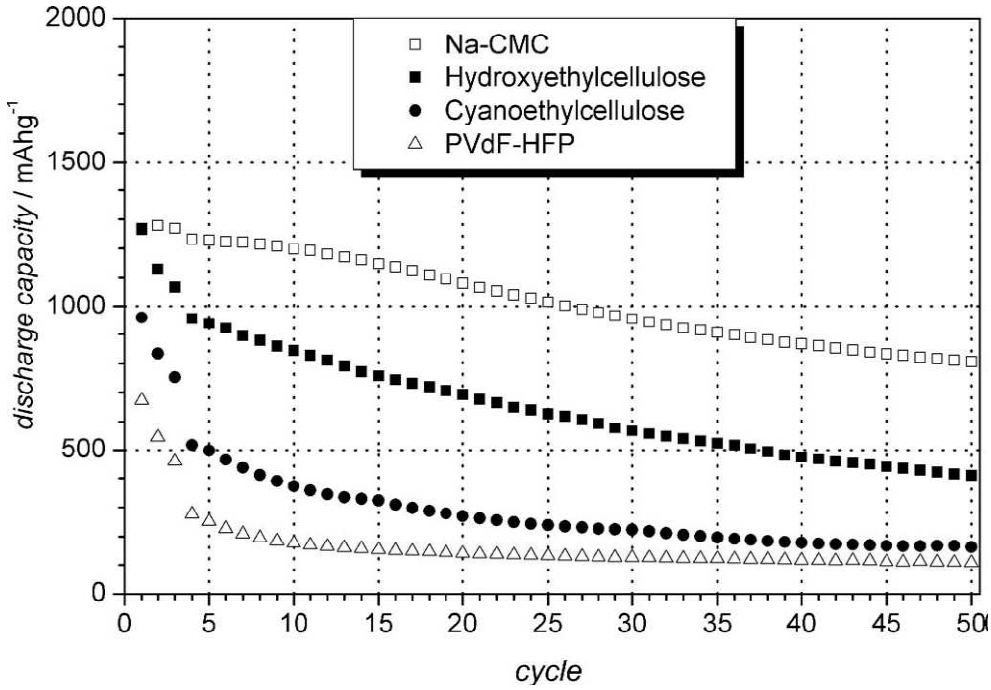

Figure 21: Influence of different cellulose binders compared to PVdF binder on cycling stability(59).

The exact reason for the enhanced cycling stability of silicon electrodes by using CMC as binder is intensively discussed in science. Styrene butadiene rubber (SBR), although having high deformation abilities, is not improving the cyclability in the expected extent meanwhile CMC, with a very important stiffness and a small elongation at break, can compensate the large volume changes much better. So it is obvious that elasticity is not the key parameter for binders to guarantee a good cycling stability (83).

Diverse explanations have been shown in literature. While B. Lestriez et al. (84) report that the better cycling stability can explained by the formation of an efficient network, N.S. Hochgatterer et al.(59) and D. Mazouzi (85) report an ester like CH_3COO-Si bond formed between the OH-groups on the surface of the silicon particle and the carboxyl group of the CMC is the reason for the improved cycling performance.

2.2.4 Electrolyte and the Role of the Solid Electrolyte Interphase (SEI) for a Long Cycle Life

Electrodes are thermodynamic unstable at low and very high potentials against the electrolyte system. In the first charge cycle when the negative potential goes below the thermodynamic stable area of the electrolyte, the electrolyte solvent starts to degrade on the electrode surface and forms the so called “solid electrolyte interphase” (SEI) (86). This corrosion layer is the reason for the principle work of lithium- and lithium ion batteries (87) (88) (89). This layer protects the electrolyte from further decomposition and the electrode from further corrosion. In contrast to alkaline earth metals, this interphase is nearly ideally lithium ion permeable and electronic insulating.

The SEI composition depends strongly on the electrode /electrolyte interactions. Competing and parallel solvent and salt reduction processes result in a number of organic and inorganic decomposition products on the electrode surface (90). Because some parts of the SEI are soluble in the electrolyte (91) the determination of the SEI thickness is difficult, and so the SEI thickness may vary from 0.1 nm up to several µm (92) (93). The key role of the SEI on the negative electrode is the protection of the electrolyte from further decomposition and the electrode from further corrosion and thereby to ensure a good cycling efficiency and cycling stability.

The composition and the structure of the SEI is object of the research of various workgroups (93) (94) (95).

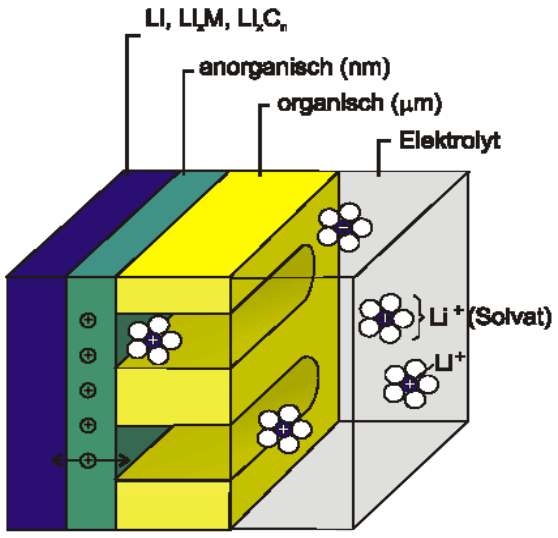

Figure 22: Schematic model of the SEI (95)

The general build up of the SEI is widely accepted. The SEI consists of an inorganic layer, consisting of e.g. Li_2CO_3 or LiF, that is contacting the electrode surface and an organic layer, consisting of oligomeric and polymeric electrolyte decomposition products. Depending on the electrolyte composition the chemical composition of the SEI layer is different (95).

The basic requirements for an ideal SEI layer, and therefore for a high efficiency and a small irreversible capacity, are:

- homogeneous chemical composition of the SEI
- fast formation of the SEI
- a good lithium permeability
- no electron transport through the SEI

Unfortunately the SEI layer is not ideally, major reasons for the inhomogenity of the SEI are listed below (96):

- different deposition rates and -potential of the solution molecules and electrolyte anions
- inhomogenity of the reaction products concerning their chemical composition
- many areas of the SEI show different electronic and ionic conductivity as well as different layer thickness (result: different reactivity)

The SEI is one of the most variable components of a lithium based cell und therefore the choice of the right electrolyte composition is from immanent importance for the cycle life of a lithium ion battery.

Solvated co-intercalation into graphite:

Due to the fact that the SEI formation and therefore the passivating of the particle surface sometimes fail, solvated co-intercalition into graphite is possible. This co-intercalation results in an exfoliation of the graphite (90) . Two different mechanisms, for the explanation of the exfoliation of graphite have been proposed in literature (97) (98).

In the first model the authors propose a co-intercalation of solvent molecules together with lithium ions between the graphene sheets (97), whereby a broadening of the distance between two graphene layers and furthermore a damage of the graphitic structure occurs. Within a few cycle the the electrode is not longer able to reversibly intercalate/deintercalate lithium ions and so the cycle life is reduced dramatically.

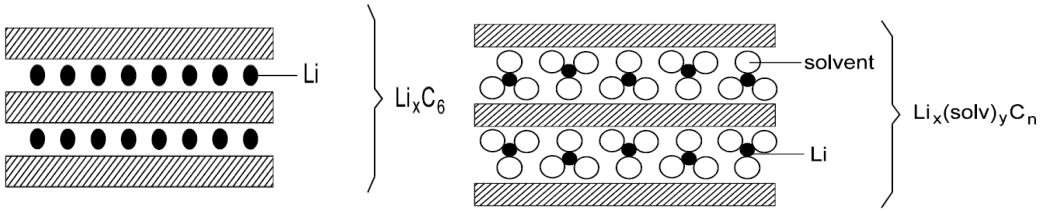

Figure 23: Lithium intercalation and solvated co-intercalation (28)

In the second model the authors argue that in propylene carbonate (PC) an internal pressure, that can be traced to the reduction of PC on the edge of the graphite particles to $R(OCO_2Li)_2$ and propylene gas, is responsible for the exfoliation of the graphite (98). The particles get cracked and fresh reactive surface is exposed to the electrolyte. In this model graphite particles covered with electrically insulating surface films are generated. They further propose that co-intercalations is only limited to ether electrolytes.

But it is a fact that solvated co-intercalation leads to a limited cycle life of graphite electrodes. So it is important to use the right electrolyte setup, either with electrolytes which form an effective SEI or by addition of film forming additives to ensure a good cycle life and high efficiencies.

Film forming agents should improve the formation of the SEI and so influence the cycleability and cycle life of lithium ion batteries significantly. Usually not more than 5 percentage (either weight or by volume) are added (99).

Role of the SEI for the cycleability of silicon:

In contrast to graphite a solvated co-intercalation into silicon is not possible by the reason of a different lithium storage mechanism (compare chapter 2.2.2 and 2.2.3).

In Figure 24 the schematic SEI formation of a silicon-bulk electrode (above) and silicon particles (below) during lithiation/delithiation is shown.

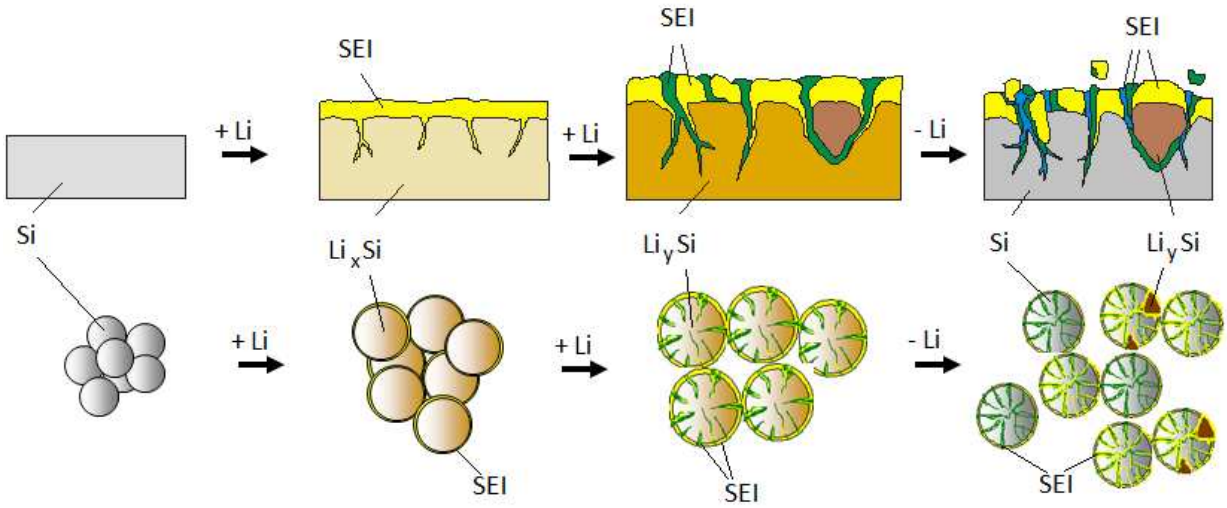

Figure 24: Schematic lithiation of silicon under consideration of the SEI building (100)

When the potential window falls below the thermodynamical stability of the electrolyte solution during lithiation, the bulk electrode respectively the particles become covered with the protective SEI layer. Because of the large volume and structure changes cracks will be generated on the surface area during further lithiation. If the SEI is not flexible enough to compensate this structure and volume changes and the so generated cracks, new electrode surface is exposed to the electrolyte and a further decomposition of electrolyte and formation of new SEI is the consequence (green area in Figure 24). Every new formation of SEI is connected with a loss of lithium and results in a bad efficiency and cycle life. By the use of bulk electrodes also a particle seperation is possible (shown in Figure 24 as brown area). This disconnected and thereby lost particles denote a further lost of lithium because of irreversible trapping of lithium in this particle. In silicon particles the pulverization of the particles and the loss of trapped lithium in a fragment happen most time during delithiation, when lithium gets extracted from the particles combined with a volume reduction. Also a loss of the contact between the particles and so the loss of a whole particle is possible (can be avoided by the right electrode setup).

By the use of intermetallic compounds as active material in negative electrodes, next to the homogeneity and compactness, a flexible SEI is one of the most important factors to guarantee high efficiencies and therefore a good cycling stability. For this reason the addition of film forming additives is necessary, e.g. addition of vinylene carbonate (99).

As previously described the composition of the SEI is strongly associated with the composition of the electrolyte solution but also of the electrode surface/electrolyte interactions.

The influence of the electrode surface on the SEI formation was shown in literature on the basis of silicon thin film electrodes with a native SiO_2 and SiOH layer (101) (102) and also by the use of silicon nano wires (103). An example from literature for this influence is given below.

Below the change of the SEI composition and the behavior of a silicon thin film electrode with a native SiO_2 layer during the first charge/discharge cycle in an ethylene carbonate/diethyl carbonate (1:1, v:v) + 1M $LiPF_6$ electrolyte is shown (Figure 25 and Figure 26) (102).

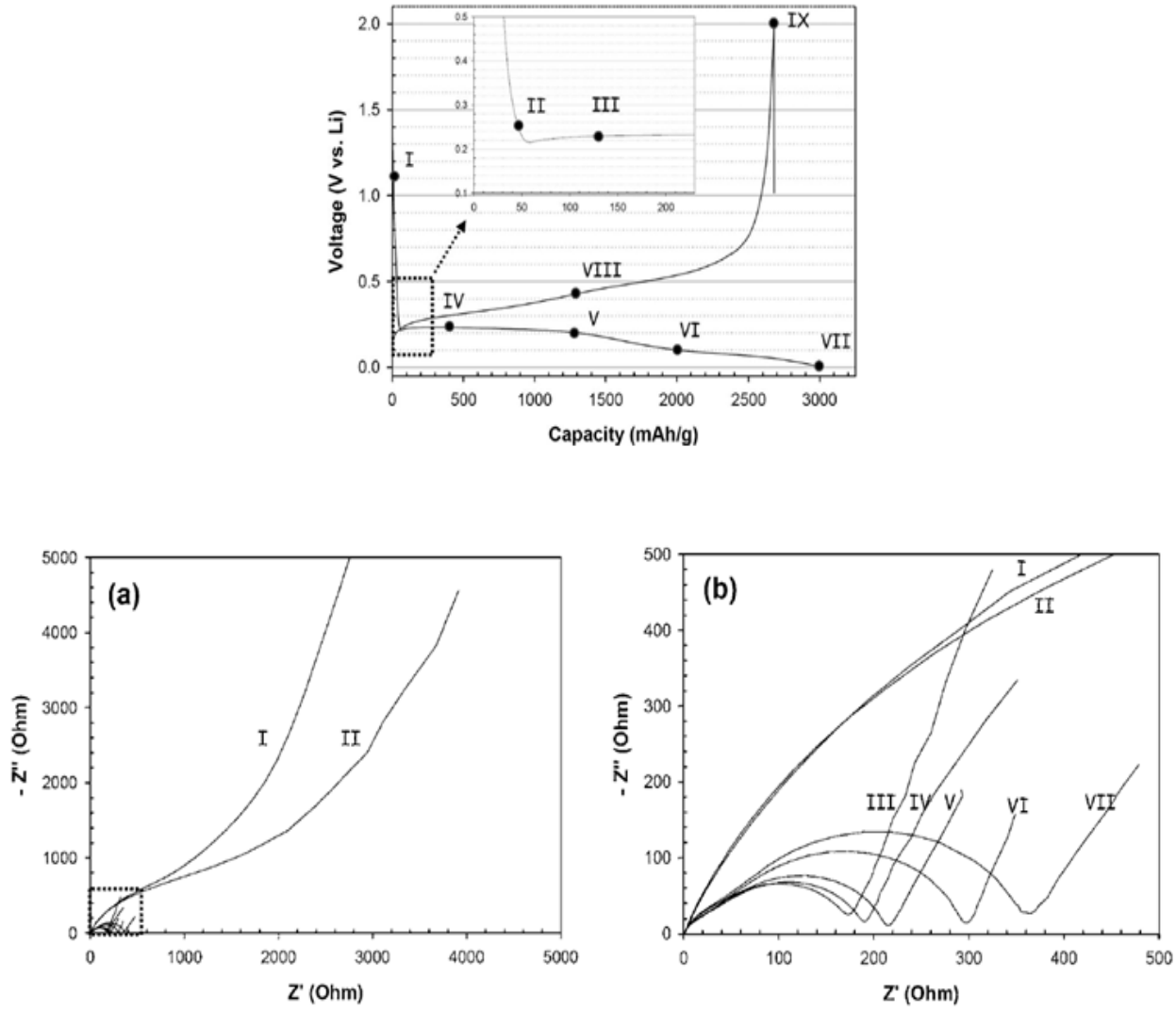

Figure 25: Charge/Discharge curve of silicon electrode (above) and below the associated impedance spectra at each stage (a) and the magnified impedance spectra (b)

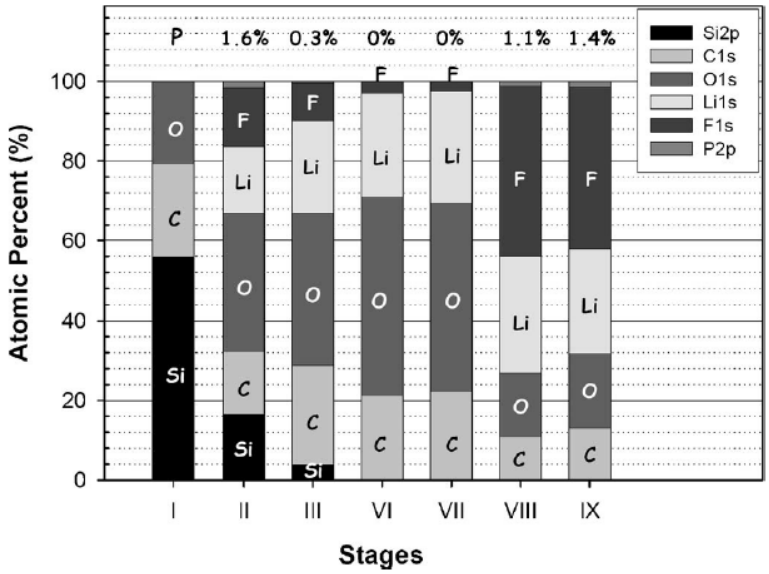

Figure 26: Surface composition, in atomic percent, of the silicon thin film electrode for each stage (done by XPS analysis)

The SEI formation strongly depends on the native SiO_2 layer and the applied current. With decreasing potential during the formation of the intermetallic Li/Si phase the percentage of silicon in the surface is also decreasing meanwhile the percentage of fluorine is increasing (Figure 26). The strongly decreasing impedance during SEI formation is an indicator for the dissolution of the native SiO_2 layer, by the fact that this layer has a worse lithium diffusion coefficient than the formed SEI. After the first formation of the SEI the electrolyte solvents and anions from the conducting salt and there decomposition products are especially involved in the SEI growing. An increasing of the impedance after a length of time given by the fact of SEI growing is also obvious (Figure 25).

During discharging basically the decomposition of the conducting salt can be observed, this leads to a higher fluorine percentage caused by formation of LiF on the surface.

2.2.5 Viewing on Practical Full Cell Problems - Cathode materials

Like delineated in chapter 2.2.3, lithium intermetallic compounds are able to store up to ~10 times more lithium per weight than graphitic carbons. This fact does not imply that the 1 to 1 substitution of the common used graphitic carbon with an intermetallic compound increase the cell energy up to 10 times. There are many practical problems concerning the substitution of graphitic carbons by intermetallic compounds secondary to the cycling problems of intermetallic compounds. Commonly used active materials at the positive side are transition lithium storage metals, like e.g. $LiCoO_2$. These transition metals deliver a specific capacity of 140 - 170 $mAh \cdot g^{-1}$. This is only the ~half of that from graphitic carbons and ~ one thirtieth of that from silicon. The low charge density of the cathode materials together with the need for more free lithium in the cell to utilize the positive effect of a higher charge density on the negative side, leads to a balancing problem. So it is a challange to balance the cathode to a pure silicon electrode. Like shown in the introduction the most noticeable improvement of the total capacity can be done, when the carbonaceous anode can be replaced by a silicon-based composite anode with a specific capacity of 1200 $mAh \cdot g^{-1}$ (5).

The balancing problem will be tightened by low coulombic efficiencies caused by continuous formation of SEI on new exposed electrode surface and trapped lithium in disconnected particles during cycling. This loss of mobile lithium must be compensated by over balancing of the cathode or developing new cathode materials with higher specific capacities or by further inserting of lithium. To clarify the problems of low efficiencies, an efficiency of 99% using graphite (theoretical specific capacity of 372 $mAh \cdot g^{-1}$) connote an irreversible capacity (loss of lithium) of 4 $mAh \cdot g^{-1}$ meanwhile an efficiency of 99% if silicon is used (theoretical specific capacity of 4200 $mAh \cdot g^{-1}$) connote an irreversible capacity (loss of lithium) of 42 $mAh \cdot g^{-1}$.

In Figure 27 the problem of cycling a common NMC cathode against a Si/C composite electrode is shown. In this measurement the NMC cathode is twice as big as the Si/C composite anode. Up to cycle 210 the cycling behaviour is controlled by the negative electrode. After the 210^{th} cycle the doubled capacity of mobile lithium is exhausted, at this point the cycling behaviour becomes controlled by the amount of mobile lithium left in the cell, which is limited by the cut off voltage of the cathode.

It is not possible that the cathode materials together with an intelligent cell balancing can solve these problems solely. So it is obvious that further improvements are necessary on both sides (anode and

cathode) before a practical implementation of intermetallic compounds at the negative side is possible.

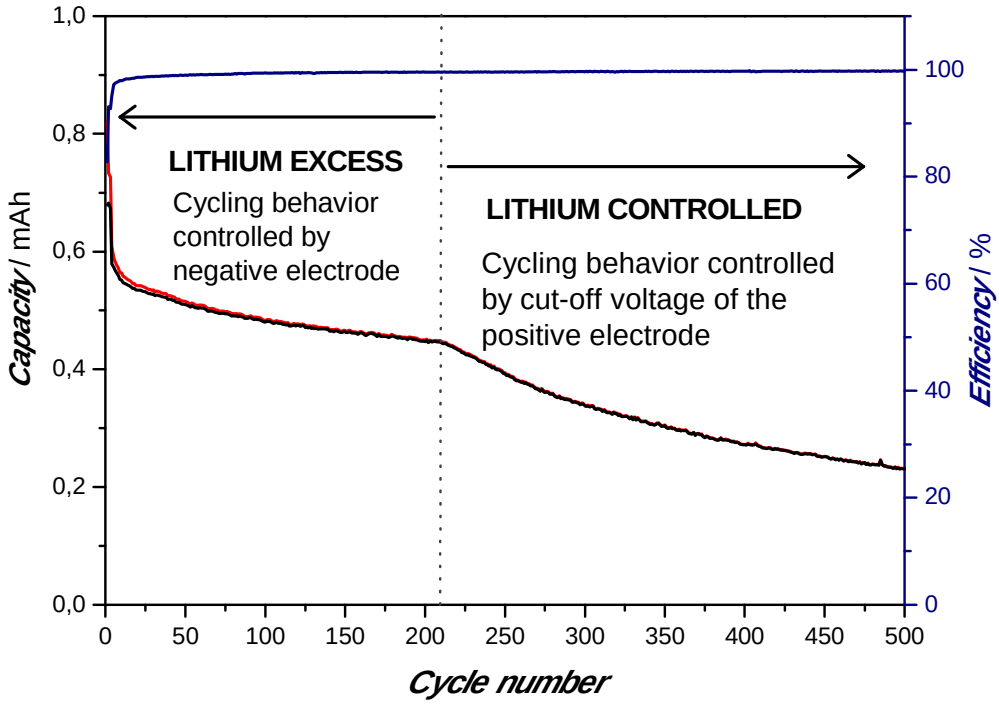

Figure 27: Full cell cycling of silicon/carbon composite vs. NMC in a *Swagelok*® -T-cell [1]

N.S. Hochgatterer showed (100) that by the use of nano silicon in a graphite/silicon composite anode (composition: 64% graphite. 20% nano Si, leftover: inactive materials) 50% of the irreversible capacity is dedicated to decomposition of the electrolyte.

So it seems possible to solve these balancing problems by a reduction of the surface area to avoid the loss of mobile lithium by SEI refilming.

[1] Graph provided by Harald Kren

3 Experimental Part

3.1 Methods and Measurement Setups

Due to the fact that various methods and measurement setups are used, basic explanations of the experimental details are given here.

Thermogravimetric Analysis / Mass Spectrometry (TGA-MS)

For a deeper understanding of the decomposition behaviour of the gelatinous polysilane, used for the fabrication of the novel developed silicon/graphite composite material (see chapter 1.1), TGA-MS experiments were performed. By reason of the chemical characteristics of cyclopentasilane (CPS) and also of the gelatinous polysilane, a special TGA cup was designed. To avoid contact between the polymerized CPS and oxygen, it was necessary to perform the measurement in a sealed TGA cup. The actual measurement was performed under He-atmosphere. For the analysis of the formed gaseous products during heating up, a small hole was put in the TGA cap, which was sealed with indium. During the measurement, when the probe chamber was already under inert gas, the sealed small hole opened at the melting point of indium (156.6 °C) and from then it was possible to analyse the gaseous products in the linked mass spectrometer.

Scanning Electron microscopy (SEM) / Energy Dispersive X-Ray Spectroscopy (EDX)

All scanning electron microscopic measurements were done on a *TESCAN VEGA3 SBU* scanning electron microscope with a secondary electron detector. For chemical analysis, the energy dispersive X-ray measurements were performed with an *Oxford Instruments Energy 250XT* detector.

Transmission Electron Microscopy (TEM) / Electron Energy Loss Spectroscopy

The TEM measurements were done on a FEI Tecnai F20, TEM/STEM (200 kV) equipped with a Schottky field emission gun, an EDAX X-ray detector, a Gatan bright field/annular dark field (ADF) detector, a Fischione high-angle annular dark field (HAADF) detector and a Gatan imaging filter (GIB Quantum™) with a dual energy range EELS acquisition system (DualEELS). All TEM measurements were performed at the Institute for Electron Microscopy and Fine Structure Research" (FELMI/TU Graz)

Electrochemical Characterisation:

All electrochemical tests were performed in a 3 electrode *Swagelok*®-T-cell (Figure 28) using a metallic lithium foil as counter and reference electrode. The average mass load of the electrodes was about 2 mg in total. A polypropylene non woven separator (Freudenberg FS2190) was used to isolate the composite electrode from the lithium counter-electrode. As electrolyte a mixture of ethylene carbonate (EC) and diethyl carbonate (DEC) (EC/DEC, 3/7 v:v) with 2 wt% vinylene carbonate (VC) as additive and 1 M $LiPF_6$ as conducting salt was used. All test cells were assembled in a dry box under argon atmosphere.

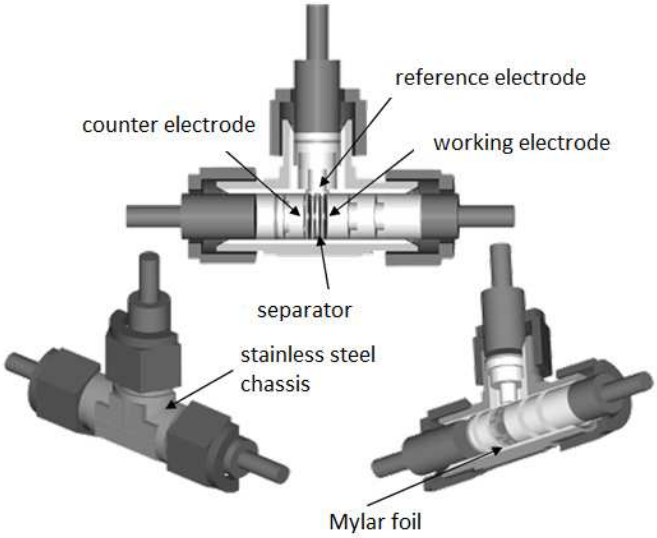

Figure 28: Schematic build up of a modified Swagelok®-T-cell

The cyclic voltammetric experiments were performed with a Potentiostat/Galvanostat (Adesys - Model 1612) at 293 K and a scan rate of 10 $\mu V \cdot s^{-1}$ and the cycling studies with a Maccor Series 4000 battery tester at 293 K.

The theoretical capacity of the material, necessary for the cycling studies, was assigned by the discharge peak area of the cyclic voltammetric measurement.

In-Situ Gas Pressure Measurement

With the Temperature Controlled Pressure Characterisation (TPC) it is possible to detect smallest amounts of gaseous products coming from electrolyte decomposition. It is not only possible to detect decomposition products during cycling and relate them to the charge or discharge step, but also to

the electrolyte decomposition during the SEI formation. The buildup of the TPC cell is close to the 3 electrode *Swagelok*® -T-cell (Figure 28), but with the addition of a pressure sensor (Figure 29).

Figure 29: Photo of the used TPC cell

Galvanostatic Intermittent Titration Technique (GITT):

The galvanostatic intermittent titration technique (GITT) is based on the principle of a small temporary applied current (0.05C) and the observation of the electrode behavior during a relaxation phase. A schematical potential profile and the summarized test program are shown in Figure 30 and Table 3. The buildup of the GITT test cell is analogue to the 3 electrode *Swagelok*® -T-cell (Figure 28) used in the electrochemical characterisations.

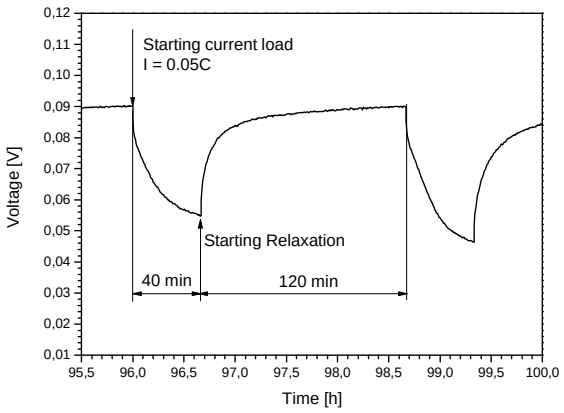

Figure 30: Schematically potential profile of a pulse in a GITT measurement

Table 3: Summarized GITT program

cycle	step	c-rate
1 -	Lithiation	0.05C for 40min
	Relaxation	120 min
	Rerun until the potential is ≤ 0 mV vs. Li/Li^+	

3.2 Graphite/Silicon Composite Material produced by thermal decomposition of Cyclopentasilane (CPS)

Several methods of silicon production are shown in literature (104)(105) (106). Silicon is either accessible through electrochemical (107) or chemical reduction(108) of chlorosilanes. Also a thermal decompositions of hydrido-substituted (109) open chain and cyclic silanes is possible. The gaseous monosilane (SiH_4) is the most common precursor by economical reasons and its good availability, but has some major disadvantages by preparation of coated or thin film materials. By the fact that SiH_4 is gaseous at room temperature the decomposition of well defined thin films or coatings is challenging. Furthermore SiH_4 is self igniting in contact with even very low concentrations of oxygen and therefore difficult to handle.

Higher hydridosilanes with the general structure Si_nH_{2n+2} or cyclic ones $-[SiH_2]_n-$ are able to form silicon via thermal decomposition. Unfortunately the decomposition temperatures of these higher hydrosilanes are often 80 – 100 °C above their boiling point (110). So the silicon production occurs also from the gaseous phase. This fact complicates the preparation of coated or thin film materials as well as the preparation of them by the use of SiH_4.

In literature is shown that cyclopentasilane (CPS, Si_5H_{10}) is able to polymerize UV-light induced(111). The formed polymers have various chain lengths with molecular weights up to 2600 $g \cdot mol^{-1}$and a gelatinous consistence. This gelatinous compound is able to form amorphous silicon by thermal treatment. So it is possible to avoid the problems, which result from the preparation of silicon preparation from the gaseous phase.

Finally a new way to produce a graphite/silicon composite material using a gelatinous silicon compound, formed from CPS as precursor, (112) (113) is shown.

3.2.1 Preparation and Characterisation

The CPS precursor was synthesized using the method which was introduced by Hengge et al. in 1973(114) (115).

Starting with the commercial available diphenyldichlorsilane, the first step is a ring closing reaction catalysed by metallic lithium. The obtained decaphenylpentasilane is chlorinated with anhydrous hydrogen chloride. This step leads to a nearly quantitative yield of the perchlorinated derivative. In the next step pure $LiAlH_4$ was slowly added. Otherwise huge amounts of different hydrogenated hydridosilanes will be obtained in this hydrogenation step. This hydrogenated hydridosilanes could not be used in the further fabrication process.

The obtained cyclic Si_5H_{10} is a colourless liquid. The reaction pathway is shown below (Equation 27). Thanks to Stefan Pichler for the production of the Cyclopentasilane.

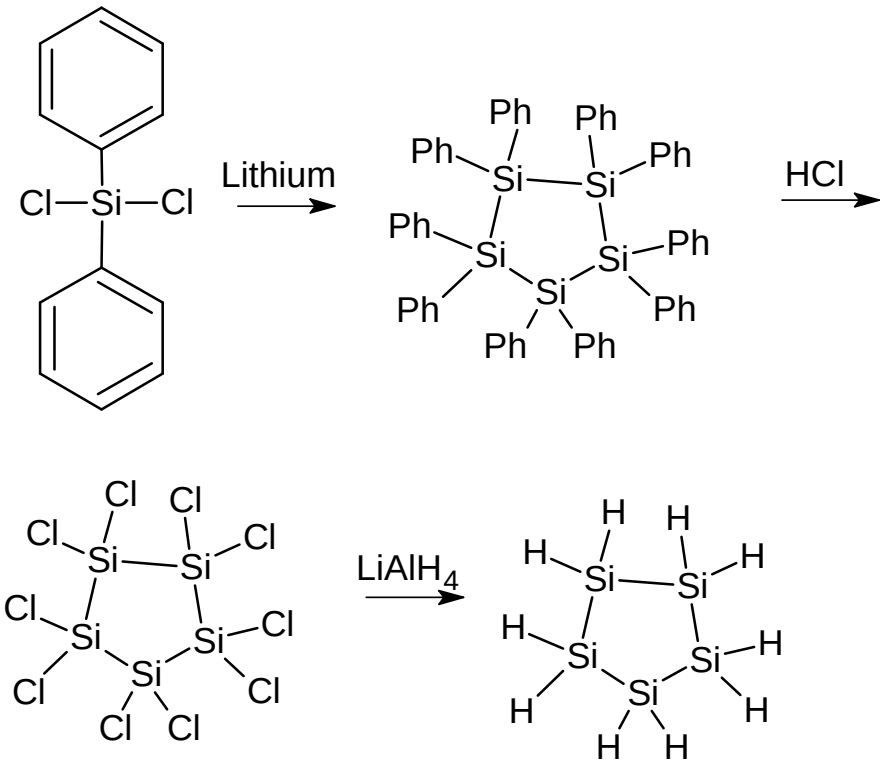

Equation 27

^{1}H NMR and ^{29}Si and -spectroscopic measurement were carried out for the verification of the structure.

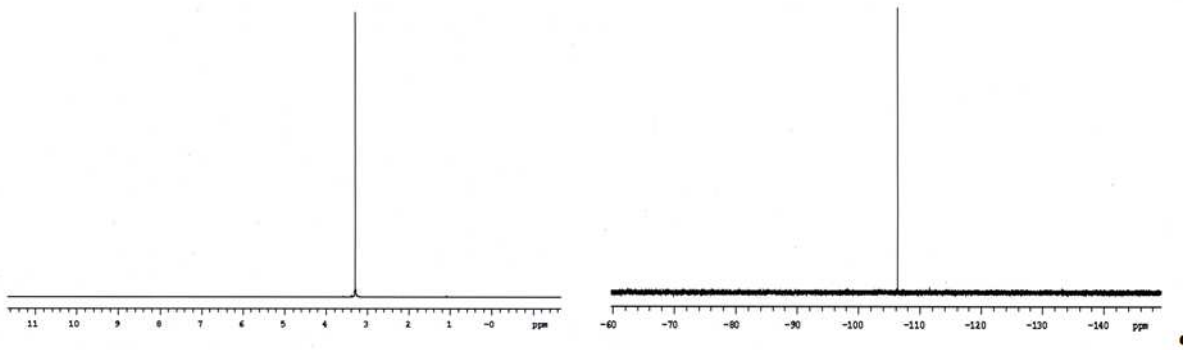

Figure 31: Measured ^{1}H spectrum (left) and ^{29}Si spectrum of cyclopentasilane

Both spectra (^{1}H and the ^{29}Si spectrum) showed the expected results and are consistent with the results reported in literature (116).

For the preparation of the electrode material, the CPS precursor was exposed to UV-light to induce photo polymerisation. During the irradiation with ultraviolet light the colourless CPS became cloudy and the colour turned into light yellow. Accompanied by this reaction, the evolution of gas was observed, which was supposed to be hydrogen. After an exposure time of seven minutes the liquid had turned into a gelatinous compound.

The decomposition behaviour of the gelatinous polysilane was examined by TGA-MS experiments. By reason of the chemical characteristics of CPS and also of the polymerized CPS, the TGA cup was sealed with indium to avoid contact between the polymerized CPS and oxygen.

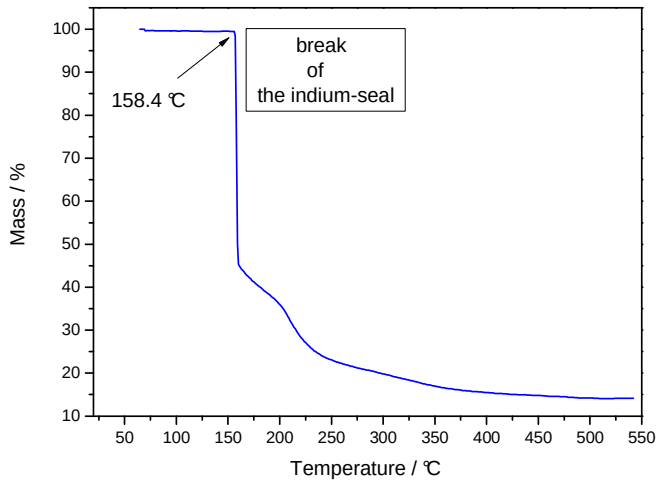

Figure 32: Thermogravimetric analysis of the decomposition of gelatinous polysilane

In Figure 32 it can be seen that at a temperature of 158.4 °C the indium (melting point: 156.6 °C) seal breaks. At this point a MS-signal could be detected. It is obvious that a huge mass loss occurs while the seal breaks. Silicon and fragments of SiH_2, SiH_4 and Si_3H_8 were detected after the seal breaks. By the reason of the wide decomposition temperature range in the further thermal decomposition processes a decomposition temperature of 823 K was chosen.

Next to the formation of silicon also SiH_2, SiH_4, Si_2H_6 and Si_3H_8 decomposition fragments were found (Figure 33). These gaseous fragments were not converted into amorphous silicon during the thermal treatment. They were emitted during the production process of the graphite/silicon composite material in form of off-gas. This result is an explanation for the fact that only 1/3 of the obtained graphite/silicon composite material consists of silicon (see page 49).

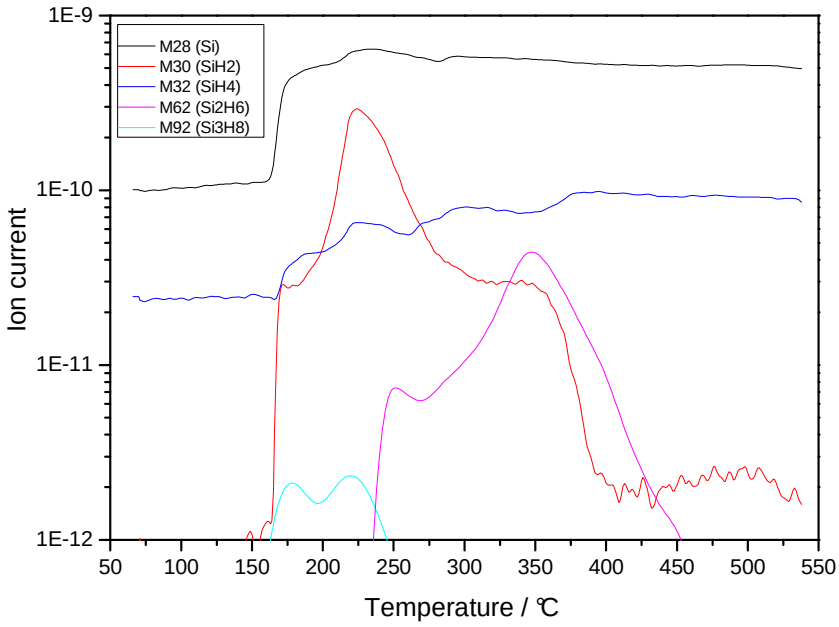

Figure 33: MS-signal of the TGA decomposition products in dependence on temperature

The gelatinous compound was decomposed under an argon atmosphere by thermal treatment with a heating ramp of 15 $K \cdot s^{-1}$up to 823 K and 2 hours at this temperature. To gain particles in a low µm range, the particles were 2 times ball milled (10min, 400 rpm) with a 5 minute break (*Pulverisette 6, classic line*). The weight ratio of the tungsten carbide balls (diameter 0.6 mm) to the silicon raw material was 10:1.

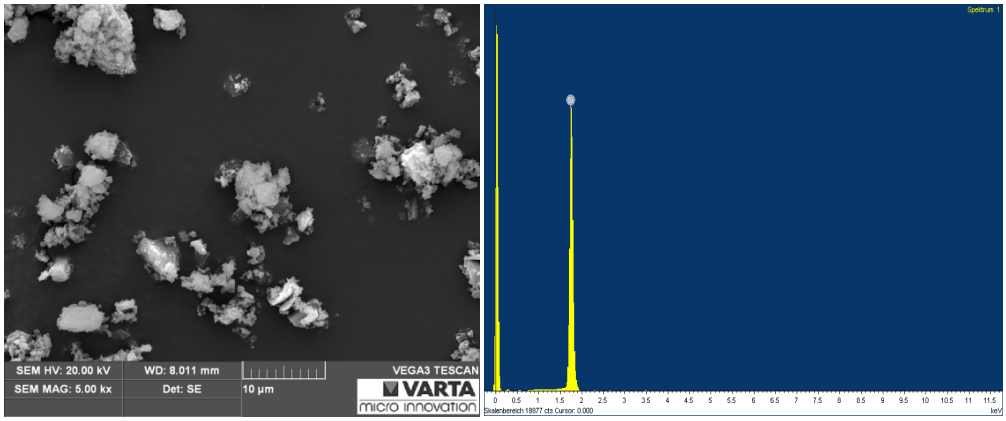

Figure 34: SEM image of amorphous silicon (left) and the chemical anaylsis (EDX spectrum) of the silicon probe (right)

The SEM image shows rough silicon particles, whose dimensions were below 10 micrometer.

To examine the electrochemical behaviour of the produced amorphous silicon a cyclovoltammetric measurement was performed. The prepared electrodes for the electrochemical tests were composed of 84 wt% silicon particles (below 10 µm), 8 wt% carbon black (*Super P)* as conducting agent and 8 wt% *CMC* as binder. The electrode slurry was prepared via an optimized dispersing technique and coated on a copper metallized non woven 3D current collector (POLYMET® XII-1 Cu), predried at 333 K (air) and finally dried at 398 K under vacuum (<10^{-2} mbar) for 24 h.

For the insertion of lithium a broad peak in the area of 250 to 0 mV could be observed. During the extraction of lithium a broad oxidation peak with a peak maximum at 350 mV was observed. As expected a bad reversibility of lithium insertion/extraction existed, which could be attributed to the drawbacks of pure intermetallic compound electrodes (see chapter 2.2.3).

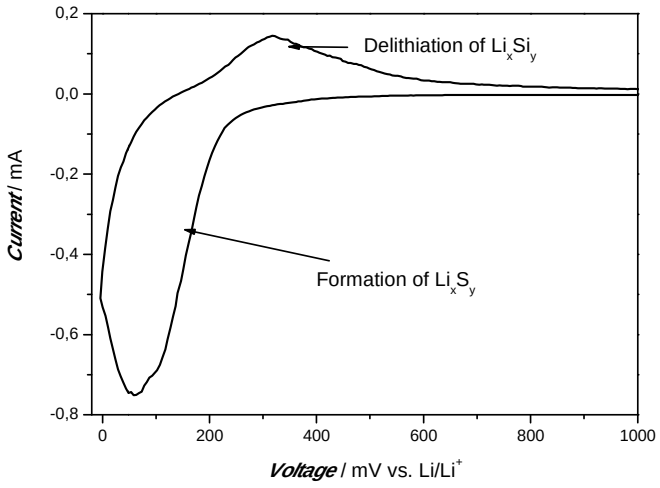

Figure 35: Cyclovoltammetric measurement of amorphous silicon, scan rate: 10 µV·s^{-1}

To obtain the graphite/silicon composite material the gelatinous polysilane was mixed with porous graphite for further processing steps. The following decomposition of the paste containing the graphite and the oligomeric- and polymeric hydridosilanes in a mass ratio of 1:1 was also done at 823 K for 2 hours with a heating ramp of 15 $K \cdot s^{-1}$. All previous process steps were done under an argon atmosphere.

After the decomposition the compound consisted of ⅓ of amorphous silicon and ⅔ of graphite (stochiometry $C_{2/3}Si_{1/3}$), whereas the silicon was deposited on the surface and in the pores of the graphite. For further preparation the gained material was dry grounded with a mortar.

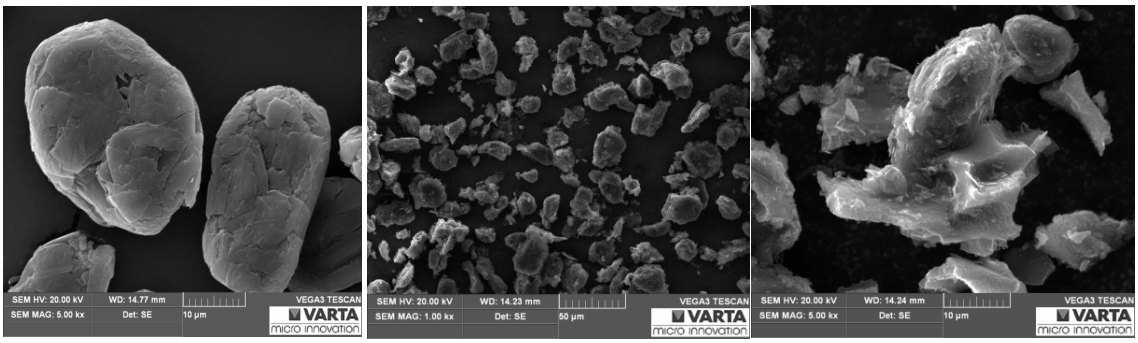

Figure 36: SEM images of natural graphite (left) and of the graphite/silicon composite material (middle and right)

The SEM images clearly show a change of the shape of the particles and coverage of the particle surface (Figure 36) with silicon. The rough textured surface was more a result of the further processing with the mortar than their native shape after the decomposition.

To get information on the inner structure of the particles, they were cut with the focused ion beam technique (FIB) and afterwards Transmission Electron Microscopy measurements were done. With HRTEM measurements the crystal dimension of the deposited silicon and the natural graphite were determined.

On the TEM images (Figure 37, left), which were taken, it was obvious that silicon was not only deposited on the graphite surface, it also filled in the pores of the natural graphite. Due to the fact that the decomposition of the silane gel was neither accompanied with a volume expansion nor with a volume contraction, the amorphous silicon was excellent linked to the graphite without damaging its crystalline structure (Figure 37, right). The low decomposition temperature prevented also the formation of an isolating silicon carbide interphase layer.

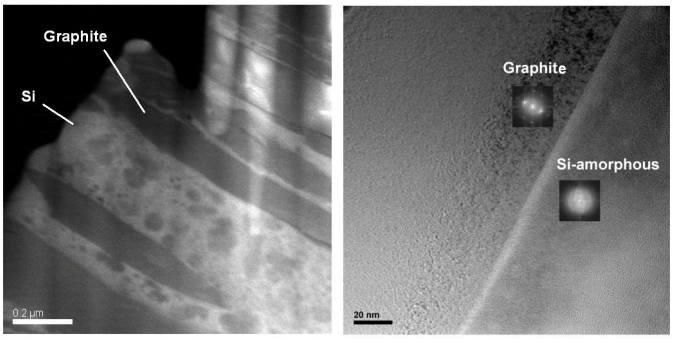

Figure 37: HAADF - TEM image (left) and HRTEM image (right) of the cut graphite/silicon particle material[2]

The silicon/graphite interphase layer was studied in detail by EELS measurement. Also in this analysis no silicon carbide layer was observable (Figure 38). Only the characteristic ionization edges for carbon (C K) and silicon (Si L23) were observed.

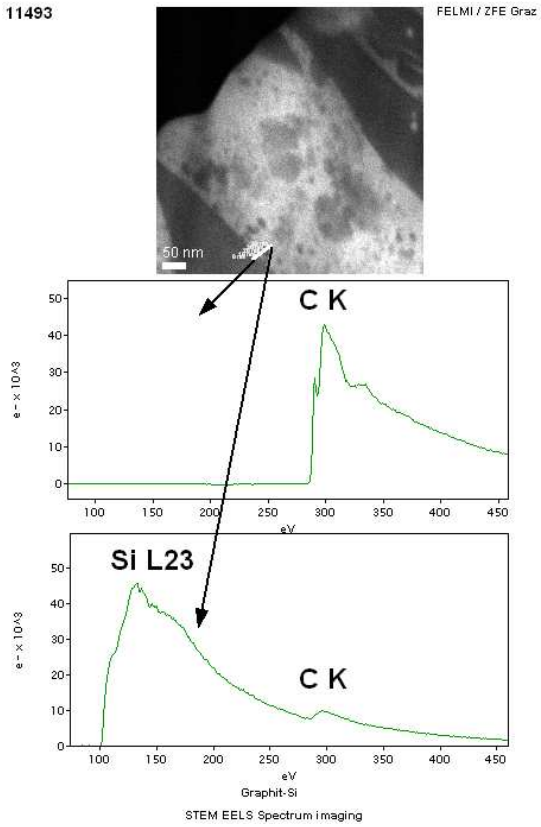

Figure 38: EELS spectrum of the graphite/silicon interphase[3]

The novel design of this active material and the very special structure of the composite material explain the excellent cycling behaviour, although the silicon is not nano sized.

[2] Recorded at the "Institute for Electron Microscopy and Fine Structure Research" (FELMI/TU Graz)

The preparation of the electrodes for the electrochemical tests were done equal to the preparation of the silicon electrodes described before. The electrodes were composed of 84 wt% graphite/silicon particles (20-30 µm), 8 wt% *Super P* as conducting agent and 8 wt% *CMC* as binder.

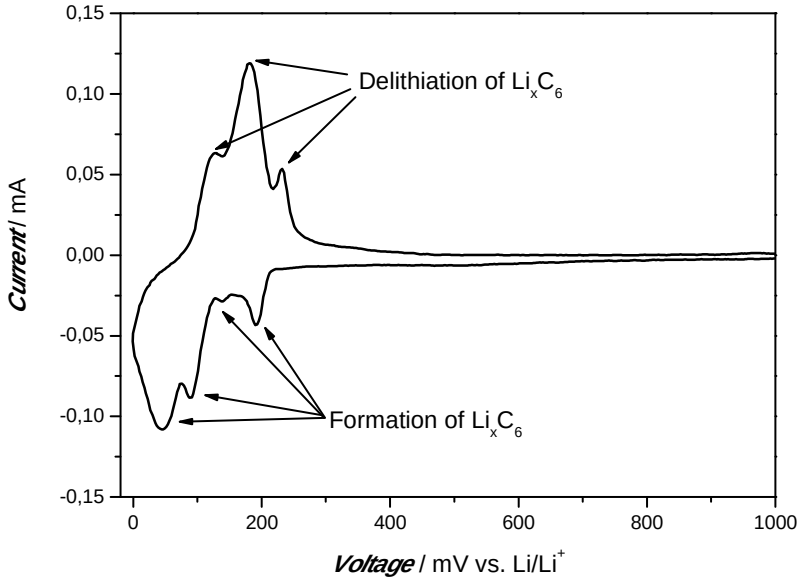

Figure 39: Cyclic voltammetric experiment of natural graphite, scan rate: 10 µV·s^{-1}

Comparing the first cycle in the cyclic voltammetric experiments (Figure 39 and Figure 40), a drastic change of the current – voltage curve and therefore of the electrochemical behaviour could be observed. For the insertion of lithium, the peaks of graphite and those of silicon were overlayed in the area of 250 and 0 mV. It was surprising, that even at a very low scan rate of only 10 µV·s^{-1} no differentiation between the insertion reaction of silicon and graphite could be made. For the oxidation of the material (extraction of lithium) the reactions of graphite and silicon differentiated very well. For graphite we observed the expected 3 oxidation peaks. The only peak for silicon, which could be observed at 500 mV, is in contrast to other characterised silicon materials and also to the results reported in literature(117). Compared to the cyclovoltammetric measurement of the pure amorphous silicon the peak is sharpener, which could be explained by the better kinetic of the whole electrode, but the peak maximum shifted about 150 mV.

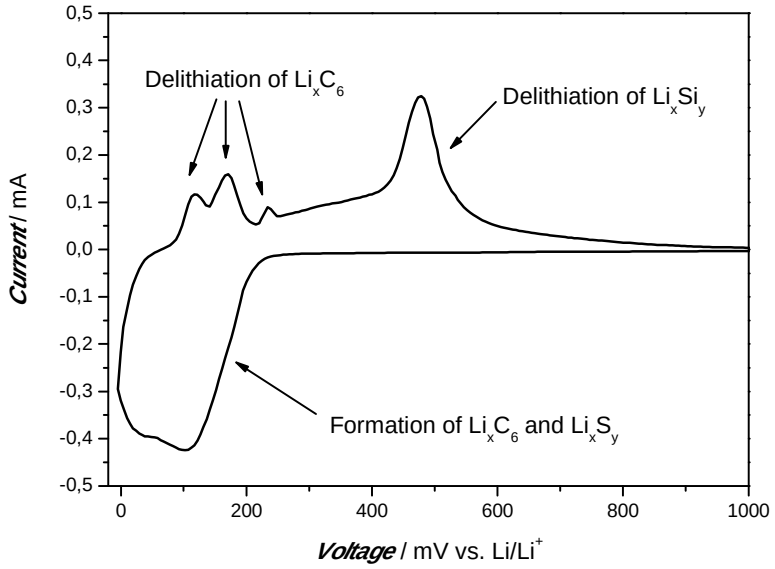

Figure 40: Cyclic voltammetric experiment of the graphite/silicon composite material, scan rate: 10 µV·s^{-1}

The long term cycling test was performed with a Maccor Series 4000 battery tester at 293 K. After one formation cycle with a c-rate of 0.2C and a period of constant voltage charge at 5 mV vs. Li/Li$^+$ for 2 hours, where the capacity was limited to 730 mAh·g^{-1}, corresponding to 60% of the theoretical capacity, the cells were cycled in the potential range of 5 - 1500 mV vs Li/Li$^+$ at a rate of 0.5C and a period of constant voltage charge at 5 mV for 2 hours. The cycling program is summarized in Table 4. The used c-rates were calculated with a theoretical capacity of 1200 mAh·g^{-1} and from the second cycle the charge capacity was limited to 840 mAh·g^{-1}. The theoretical capacity of the material was assigned by the discharge peak area of the cyclic voltammetric measurement. The current density for a c-rate of 1C was 1.32 mA·cm^{-2}.

Table 4: summary of the cycling program (capacity limit 0.7C mAh·g^{-1})

cycle	step	c-rate
1	constant current charging	0.2C to 5 mV or capacity limit
	constant voltage charging	2 h at 5 mV or capacity limit
	constant current discharging	0.2C to 1500 mV
2 - 100	constant current charging	0.5C to 5 mV or capacity limit
	constant voltage charging	2 h at 5 mV or capacity limit
	constant current discharging	0.5C to 1500 mV

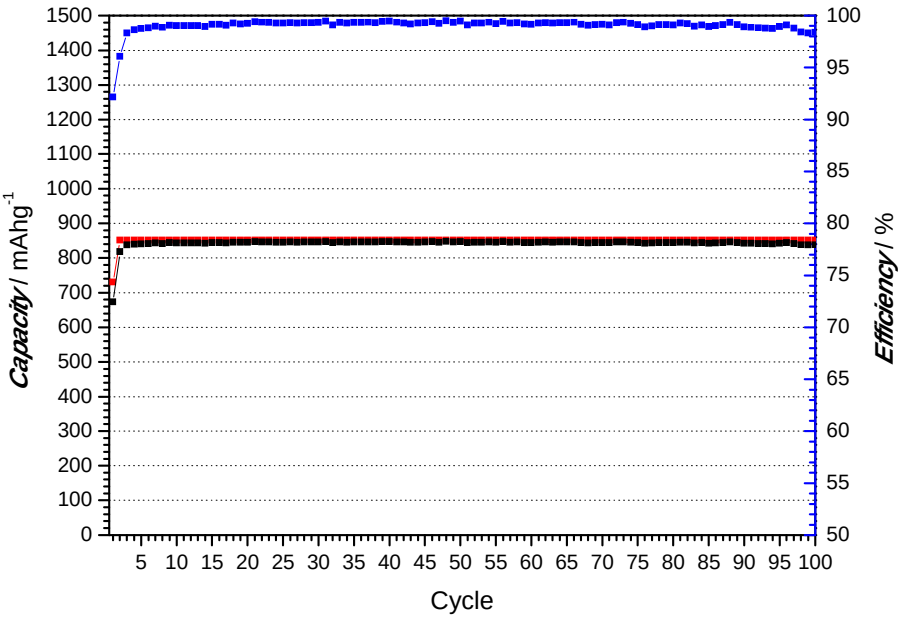

Figure 41: Cycling study of the graphite silicon composite material (capacity limited to 0.7C)

In the cycling study (Figure 41) the capacity was limited to 840 mAh·g^{-1}, what complies with 70% of the theoretical capacity of 1200 mAh·g^{-1}. The lower capacity in the first cycle was a result of the special formation program, in which the capacity was limited to 60% of the theoretical capacity to counter the large volume changes which occur when silicon would be fully loaded. The lower efficiency in the first cycles was the result of the film formation. After the formation a stable cycling of over 100 cycles with an excellent efficiency of more than 99% could be observed (Figure 41).

3.2.2 Determination of the Internal Electrode Resistance - Galvanostatic Intermittent Titration Technique (GITT)

The 1977 introduced galvanostatic intermittent titration technique (GITT) (118) became one of the standard methods to identify the electrochemical behaviour of electrode materials.

The galvanostatic intermittent titration technique (GITT) is based on the principle of a small temporarily applied current (0.05C) and the observation of the electrode behavior during a relaxation phase (Figure 42).

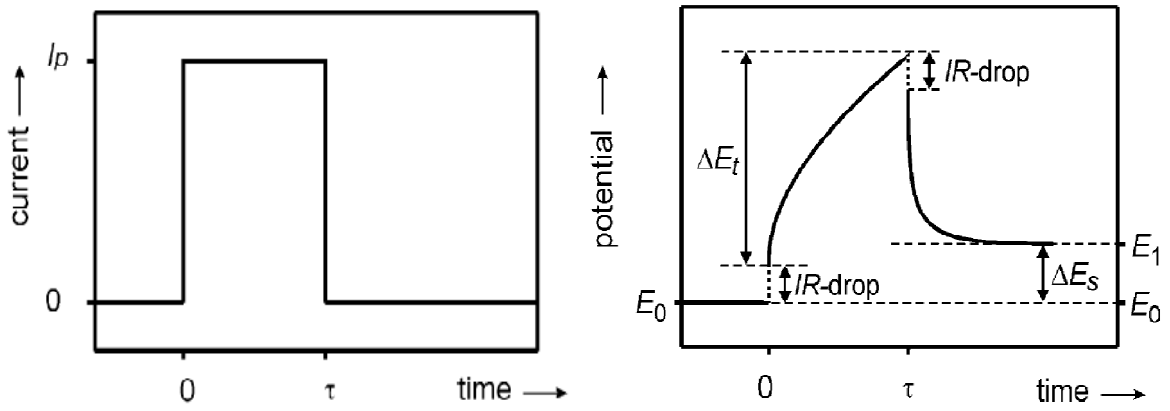

Figure 42: Scheme of a single GITT step, current set point (left) and the associated potential response (right)(119)

Several effects can be observed during the temporary current application. The IR drop is given by the natural characteristics of the used active materials and their interaction in the electrode. Natural characteristics include passivating layers, e.g. SiO_2 layers on the Si surface, diffusion coefficients, crystal structure and defects of the crystal structure. Whereas characteristics like wetability of the electrode with electrolyte or the electronic conductivity of the whole electrode are given by the electrode composition and the interaction between the active material particles. However, all these characteristics influence the charge-transfer behavior of an electrode.

Due to the fact of diffusion processes in the electrode, the cell approximates to a new thermodynamic equilibrium during the relaxation phase. By a change of the stoichiometric composition (lithiation or delithiation of the electrode material) a new potential sets in. Because the relaxation is an indefinitely slow process, the potential approximates asymptotic to the steady state in a real system.

The previous specified small temporarily applied current steps (0.05C) and the following relaxation phases are repeated until the material is fully lithiated.

Together with impedance measurement, the galvanostatic intermittent titration technique (GITT) became one of the standard methods to identify the chemical diffusion coefficient of lithium ions in battery active materials.

Lithium transport in electrodes obey the Fick`s second law, therefore the diffusion coefficient of lithium ions can be calculated by following equation (120):

$$D^{GITT} = \frac{4}{\pi * \tau}\left(\frac{m_B\, V_M}{M_B\, S}\right)^2 * \left(\frac{\Delta E_s}{\Delta E_t}\right)^2$$

Equation 28

τ... constant current pulse time

m_B... mass of host material

V_M... molar volume of host material

M_B... molar mass of host material

S... electrode/electrolyte interphase area

ΔE_s... change of steady state voltage during single GITT step

ΔE_t... total change of cell voltage during constant current pulse

In the case of silicon, it is not possible to calculate absolute values of the diffusion coefficient from the GITT experiment. Due to the fact of high volume changes during lithiation/delithiation important basic parameters, like the surface area of the electrode, changes permanent. Particularly by use of nano particles (e.g.silicon nano particles) existing electrochemical double layers play a non negligible factor, but are unaccounted in the experiment and therefore an additional error source for the absolute calculation of the lithium diffusion coefficient. By this reasons in this work the GITT experiments should only provide information about internal resistances and diffusion abilities of the used materials.

The subsequent shown GITT experiment was carried out at a Si/C composite electrode. The Si/C composite material was produced by thermal decomposition of CPS, and the electrodes were composed of 84 wt% graphite/silicon particles (20-30 µm), 8 wt% carbon black (*Super P)* as conducting agent and 8 wt% *CMC* as binder and the measurement was done in a 3 electrode *Swagelok*®-T-cell. The summarized GITT measurement program is shown in Table 3 (see chapter 3.1).

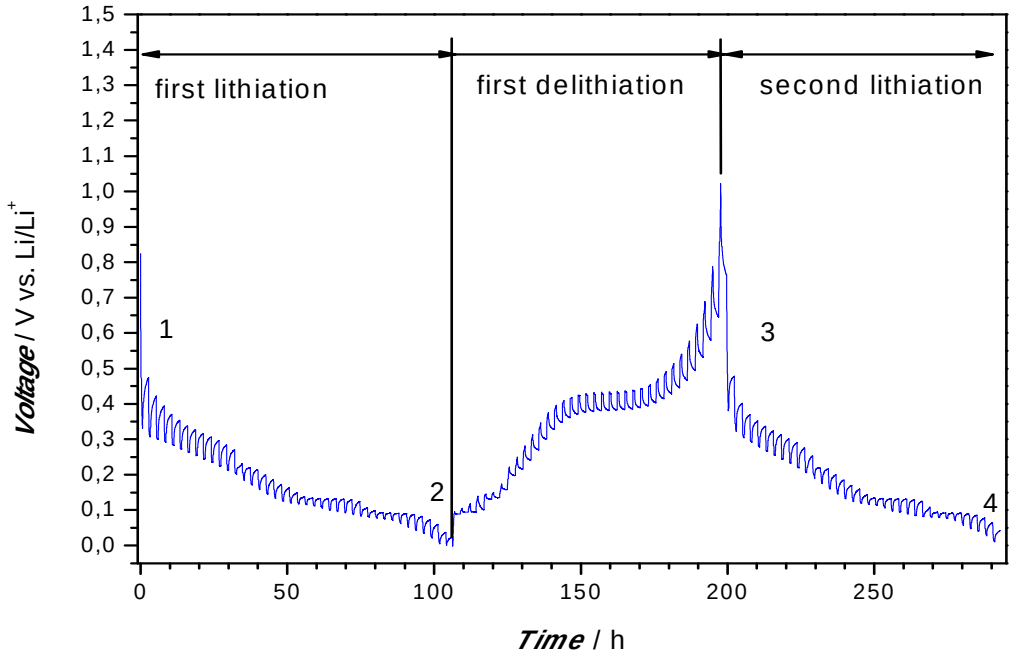

Figure 43: GITT measurement of a silicon/graphite composite electrode formed from CPS

Through closer examination of the GITT experiment two imaginary lines can be observed. In the lithiation step the lower imaginary line describes the potential characteristics while charging conditions, while the upper imaginary line describes the steady state status (open circuit voltage (OCV)), of the respective lithiated silicon/graphite compound. Furthermore it is obvious that the internal reaction resistance decreases during lithiation. The reason for the decreasing internal reaction resistance is a significant higher electric conductivity of the Li_xSi_y phases than the pure silicon phase (72) (analogous to doping of silicon semiconductors). The decrease of the internal reaction resistance can also be observed in the second lithiation step.

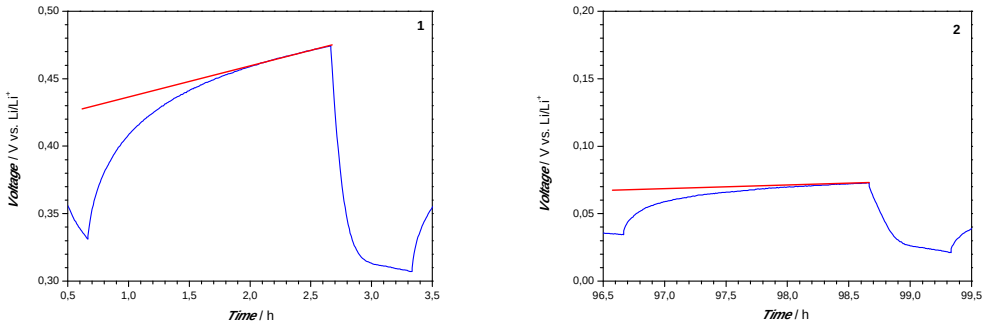

Figure 44: Relaxation profile of a Silicon/Graphite composite electrode, 1: start first lithiation, 2: end first lithiation

By comparison of the relaxation profiles of the first lithiation (area 1, Figure 44) and of the end of the first lithiation a faster relaxation into the steady state is obvious. Because silicon is also deposited on the graphite surface and not only in the pores, a native SiO_2 layer, resulting from storage under air, is build on the particle surface. The observed characteristics are a result of an inhibition of the lithium diffusion at the beginning, coming from this native SiO_2 layer (14). Is this passivation layer broken once, the kinetic behaviour of the electrode is increased (comparison area 1 Figure 44 and area 3 Figure 45). The formation of good lithium ion conducting SEI also decreases the inhibition of the lithium diffusion in the system. Therefore lower overpotentials and a lower IR-Drop can be examined by reason of a higher conducting at higher lithium content.

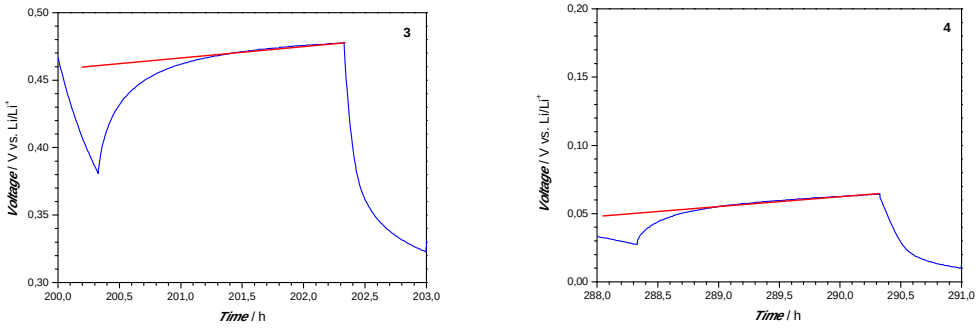

Figure 45: Relaxation profile of a Silicon/Graphite composite electrode, 3: start second lithiation, 4: end second lithiation

3.2.3 Determination of the Rate Capability

A rate capability test of the prepared Si/C composite electrodes was done in a 3 electrode *Swagelok*®-T-cell with lithium as counter- and reference electrode. The mass load of the electrode was 2.5 mg·cm^{-2}. For the determination of the c-rate for the rate capability test, a cyclovoltammetric measurement was performed before.

To determine both, the charge and discharge rate capability, a combined rate capability test was performed. Starting with a moderate c-rate of 0.2C in the first cycle the cell was charged/discharged up to a c-rate of 1C in a potential window of 5 mV – 1500 mV. Intermediate 1 cycle with the moderate starting c-rate of 0.2C were performed to prove the capacity retention during the rate test. The full rate capability test program is shown in Table 5.

Table 5: Summarized rate capability test program

cycle	step	c-rate	current density
1	constant current charging	0.2C to 5 mV	0.6 mA cm^{-2}
	constant current discharging	0.2C to 1500 mV	0.6 mA cm^{-2}
2 – 6	constant current charging	0.4C to 5 mV	1.2 mA cm^{-2}
	constant current discharging	0.4C to 1500 mV	1.2 mA cm^{-2}
7	constant current charging	0.2C to 5 mV	0.6 mA cm^{-2}
	constant current discharging	0.2C to 1500 mV	0.6 mA cm^{-2}
8 – 12	constant current charging	0.6C to 5 mV	1.8 mA cm^{-2}
	constant voltage charging	0.6C to 1500 mV	1.8 mA cm^{-2}
13	constant current charging	0.2C to 5 mV	0.6 mA cm^{-2}
	constant current discharging	0.2C to 1500 mV	0.6 mA cm^{-2}
14 – 18	constant current charging	0.8C to 5 mV	2.4 mA cm^{-2}
	constant current discharging	0.8C to 1500 mV	2.4 mA cm^{-2}
19	constant current charging	0.2C to 5 mV	0.6 mA cm^{-2}
	constant current discharging	0.2C to 1500 mV	0.6 mA cm^{-2}
20 -24	constant current charging	1.0C to 5 mV	3.0 mA cm^{-2}
	constant current discharging	1.0C to 1500 mV	3.0 mA cm^{-2}
25	constant current charging	0.2C to 5 mV	0.6 mA cm^{-2}
	constant current discharging	0.2C to 1500 mV	0.6 mA cm^{-2}

With a moderate c-rate of 0.2C an initial charge capacity of 1180 mAh·g^{-1} could be achieved. With increasing c-rates the charge/discharge capacities decreased clearly. By an applied c-rate of 1C, the achievable charge capacities were 450 mAh·g^{-1} on average. However in the first intermediated cycle (7th cycle) at a moderate c-rate of 0.2C an increased charge capacity (1240 mAh·g^{-1}), compared to the initial charge capacity is obtained. The 5 cycles at a c-rate of 0.4C could be examined as further formation cycles. In the following intermediated cycles (cycle 13, 19 and 25) only a small decrease in the charge capacity could be observed. The low achievable capacities at high applied current densities connoted a limitation of the state of charge (SOC). The lower degree of lithiation leads to smaller volume changes and mechanical stress during lithiation/delithiation with the result of a good capacity retention after 25 cycles.

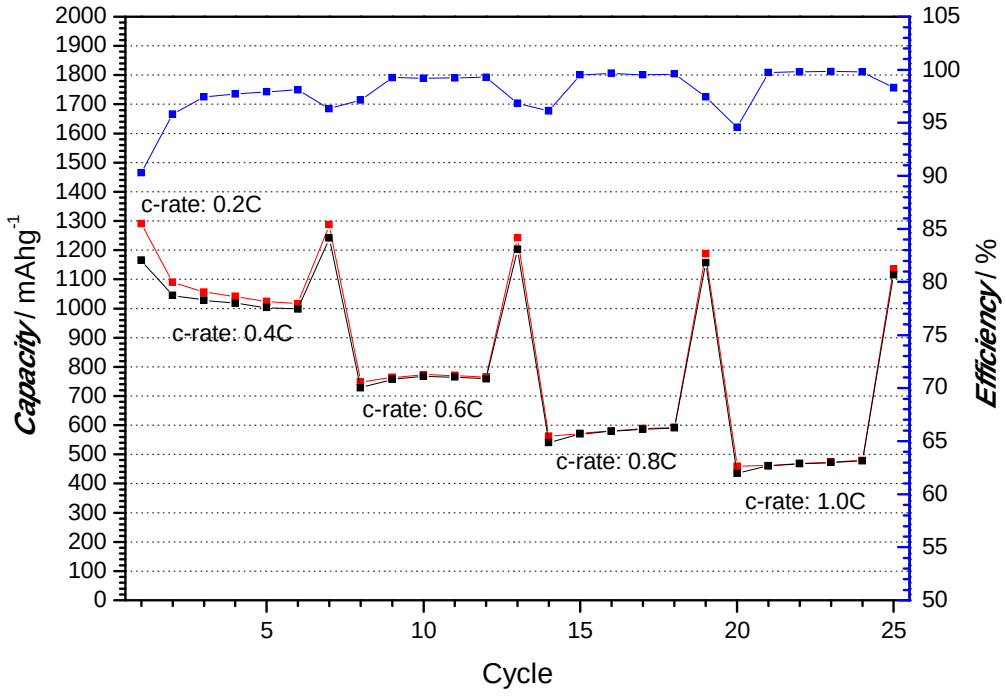

Figure 46: Rate capability test of Si/C composite prepared by decomposition of CPS

Because of the novel active material design with its layered structure a better rate capability could be expected. The good embedding of the silicon in the graphite pores should lead to a better electric conducting. However, given by the fact that the particles are not nano sized, the effect of the better conducting did not increase the rate capability in such a positive way like expected because of larger solid state diffusion paths. But the general capacity decrease at higher c-rates is, due to the high electrode mass load of 2.5 mg·cm^{-2} not surprising. Furthermore a linear decrease of the voltage curve

could be observed at a c-rate of 1.0C (Figure 47). That indicates that the charge reaction was limited by the lithium transport through the electrolyte and not by the rate capability of the active material. The diffusive inhibition was a result of the used mess setup with 6 pieces of a polypropylene non woven separator (Freudenberg FS2190), which was also used as electrolyte reservoir and increased the lithium diffusion paths in the electrolyte. To provide meaningful results at such high current densities (~3.0 $mA \cdot cm^{-2}$) a rate capability test in a full cell should be designed, whereat by reason of the low capacity of the cathode material compared to a silicon/graphite composite material the balancing of such an test setup in labor scale is impossible.

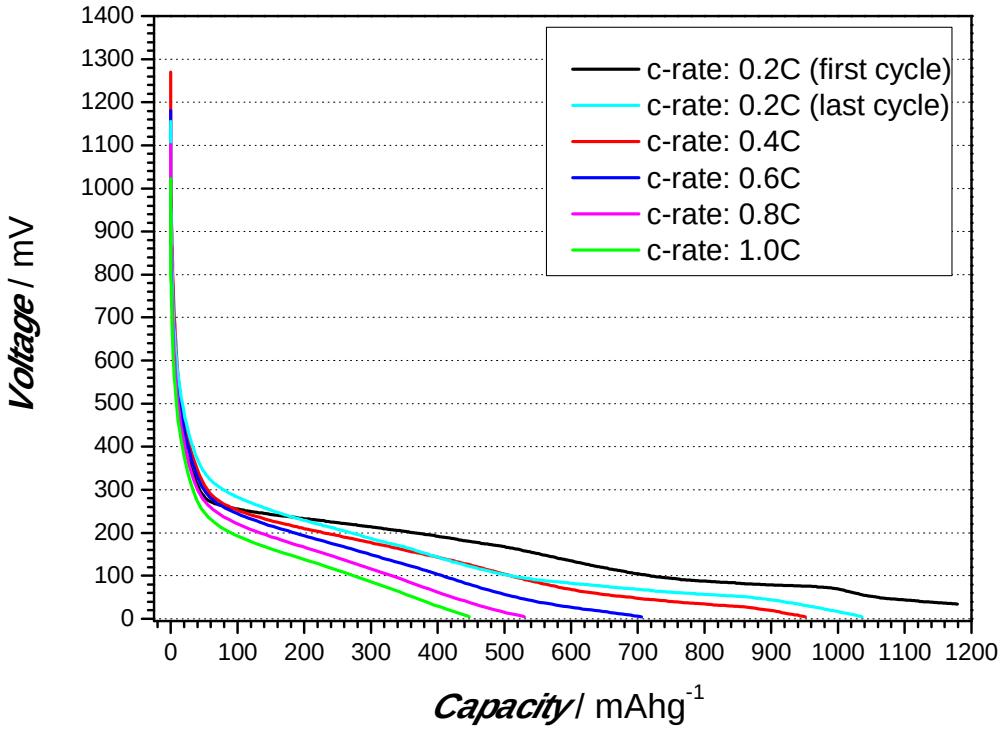

Figure 47: Achieved charge capacities at different c-rates

3.2.4 Influence of Cycling Conditions on the Cycle Life of Silicon Composite Electrodes

The cycling behaviour of silicon and silicon/graphite composite electrodes strongly depends on the cycling conditions. Not only the applied current density decrease or increase the achievable capacities and cycle life, also by controlling the state of charge (SOC) (72) the cycling properties can be enhanced. By a view on the physical and chemical properties of intermetallic compounds, it is easy to distinguish that a limitation of the state of charge (SOC) can enhance the cycle properties of a silicon electrode by controlling the volume expansion during lithiation/delithiation. So the mechanical stress, which leads to pulverization and disintegration of the silicon particles, can be controlled. Subsequent two possibilities of limitation of the state of charge should be discussed and compared to each other.

In the subsequent experiments the electrodes were produced according to the instructions presented in chapter 3.2.1 (see page 48).

Based on the fact that the used 3D current collector is inhomogeneous in mass, it was not possible to determine the mass load of the electrodes by weighing. For this reason the c-rates needed for the galvanostatic charge/discharge tests cannot be calculated theoretically. For the determination of the c-rate for the subsequent measurements, cyclovoltammetric measurements (3 cycles, scan rate: 30 $\mu V \cdot s^{-1}$) had to be done. By reason of electrode formation during the 3 cyclovoltammetric cycles high efficiencies at the first cycles in the galvanostatic charge/discharge tests could be observed.

Capacity limited cycling:

By limitation of the capacity it is possible to generate an active material pool, which can compensate loss of active material during cycling. Furthermore by reason of decreased electrochemical charge, a decreased volume expansion and thus a reduced mechanical stress can be expected, which in turn leads to a reduced loss of active material and so also to an increased efficiency.

In the first measurement the capacity was limited to 920 $mAh \cdot g^{-1}$, so an active material pool of 280 $mAh \cdot g^{-1}$ was generated. To use the whole capacity of 920 $mAh \cdot g^{-1}$, when the cell was cycled with a c-rate of 0.5C, a constant voltage charging step was necessary at 5 mV for 2 hours. The full cycling program is shown in Table 6.

Table 6: Summarized capacity limited (920 mAh·g^{-1}) cycling program

cycle	step	c-rate
1	constant current charging	0.2C to 5 mV or 720 mAh·g^{-1}
	constant voltage charging	2 h at 5 mV or 720 mAh·g^{-1}
	constant current discharging	0.2C to 1500 mV
2 - 100	constant current charging	0.5C to 5 mV or 920 mAh·g^{-1}
	constant voltage charging	2 h at 5 mV or 920 mAh·g^{-1}
	constant current discharging	0.5C to 1500 mV

When the capacity is limited to 920 mAh·g^{-1} a stable cycling over 46 cycles with a good cycling efficiency can be observed (Figure 48). At this point the generated active material pool was exhausted and in the further cycles a loss of capacity can be observed. Noticeable is a small decrease of the cycling efficiency a few cycles before the active material pool is exhausted (cycle 42 up to cycle 45). Furthermore a bigger fluctuating of the efficiency, coming from the loss of active material, could be observed in the last 50 cycles.

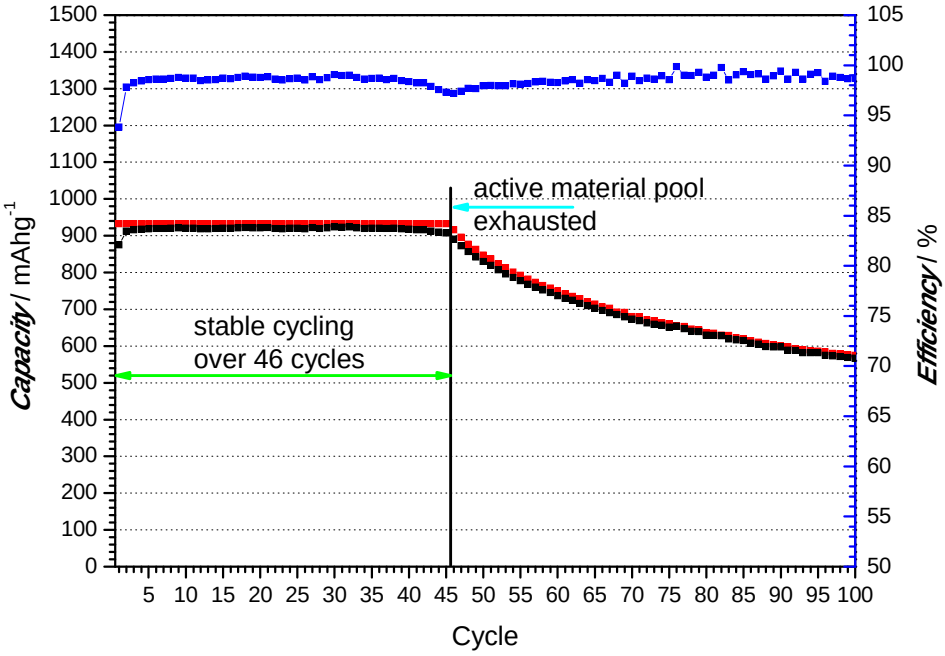

Figure 48: Cycling study of a Si/C composite material, 0.8C 920 mAhg

To point out the effect of capacity limited cycling more clearly, a cycling experiment, where the capacity was limited to 0.5C of the theoretical capacity (600 mAh·g^{-1}, see Figure 49), was done. The used cycling program of this measurement is summarized in Table 7.

Table 7: Summary of the cycling program (capacity limit 0.5C)

cycle	step	c-rate
1 - 250	constant current charging	0.5C to 5 mV or 600 mAh·g^{-1}
	constant voltage charging	2 h at 5 mV or 600 mAh·g^{-1}
	constant current discharging	0.5C to 1500 mV

The limitation to a SOC of 50% and the associated decreased electrochemical charge lead to an impressive enhancement of the cycling stability of the electrode. The reduced mechanical stress resulting in smaller volume changes during lithium insertion/extraction lead to a reduced loss of active material, which can easily be compensated by the generated active material pool. With these cycling conditions it is possible to cycle the silicon/graphite composite material over 250 cycles with an excellent cycling efficiency of over 99.5% after the 50 cycle.

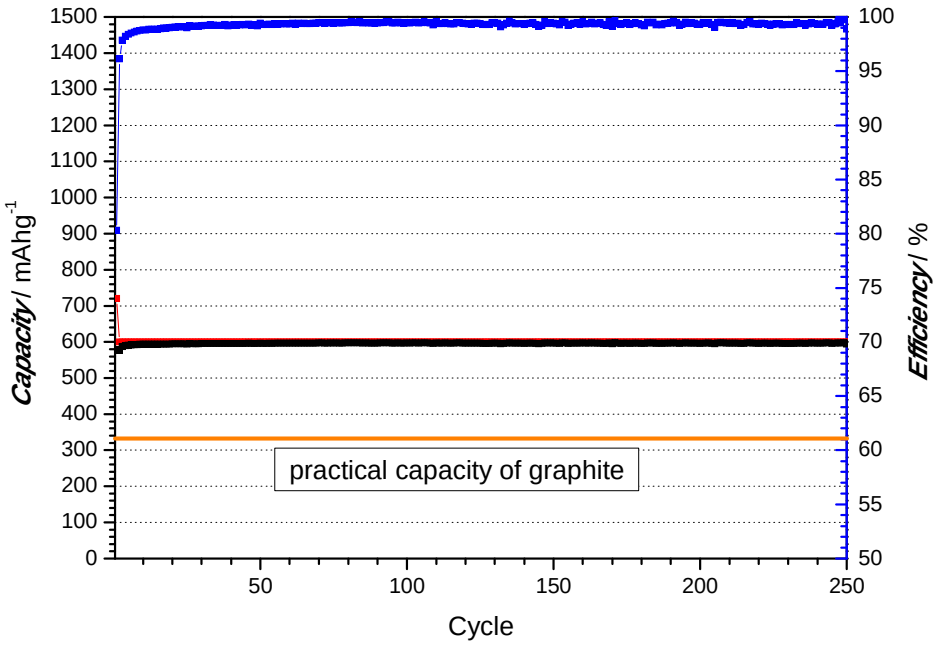

Figure 49: Cycling study of the graphite silicon composite material (capacity limited to 0.5C)

However, 600 mAh·g^{-1} denote a capacity increase of 1.8 times compared to a realistic practical capacity of graphite (330 mAh·g^{-1}). Only small improvements on the cycling efficiency have to be done (e.g. on the electrolyte additive side) to make this composite material useful for the application in state of the art lithium ion batteries.

Capacity limited Cycling combined with a Limited Cut Off Voltage:

The positive influence of capacity limited cycling on the cycling performance of silicon/graphite composite electrodes was impressively shown before. However a cut off voltage of 5 mV denotes the possibility of a crystallization and formation of the $Li_{3.75}Si$ intermetallic phase, which occurs under 50 mV vs. Li/Li$^+$ (65). To avoid the crystallization of this phase, a cut off voltage over 50 mV seems to be a promising approach to reduce the mechanical stress and to prevent the formation of the $Li_{3.75}Si$ phase during lithiation. Unfortunately limiting the cut off voltage implies a decreased usable electrical energy by reason of a decreased overall cell potential (mathematical correlation, see Equation 1 in chapter 1). The combination of capacity limitation and limiting the cut off voltage was chosen to compare the results to the previous measurements and to point out the positive influence of cut off voltage limitation.

After one formation cycle (capacity limit 720 mAh·g^{-1}) cycling the cell with a c-rate of 0.2C to a cut off voltage of 60 mV and a subsequent constant voltage charging step for 2 hours at 60 mV, the cell was cycled with a c-rate of 0.5C to 60 mV and a necessary constant voltage charging step (4 hours at 60 mV) to use the full limited capacity of 960 mAh·g^{-1}.The full cycling program is shown in Table 8.

Table 8: Summarized interrupting voltage limited cycling program (60 mV), capacity limited to 960 mAh·g^{-1}

cycle	step	c-rate
1	constant current charging	0.2C to 60 mV or 720 mAh·g^{-1}
	constant voltage charging	2 h at 60 mV or 720 mAh·g^{-1}
	constant current discharging	0.2C to 1500 mV
2 - 100	constant current charging	0.5C to 60 mV or 960 mAh·g^{-1}
	constant voltage charging	4 h at 60 mV or 960 mAh·g^{-1}
	constant current discharging	0.5C to 1500 mV

Although in this case the generated active material pool is decreased about 40 mAh·g^{-1}, compared to the previous capacity limited cycling experiment (Figure 48), a stable cycling over 100 cycles could be observed (Figure 50). Furthermore an excellent efficiency was also the result of the cut off limitation could and could be observed over all 100 cycles.

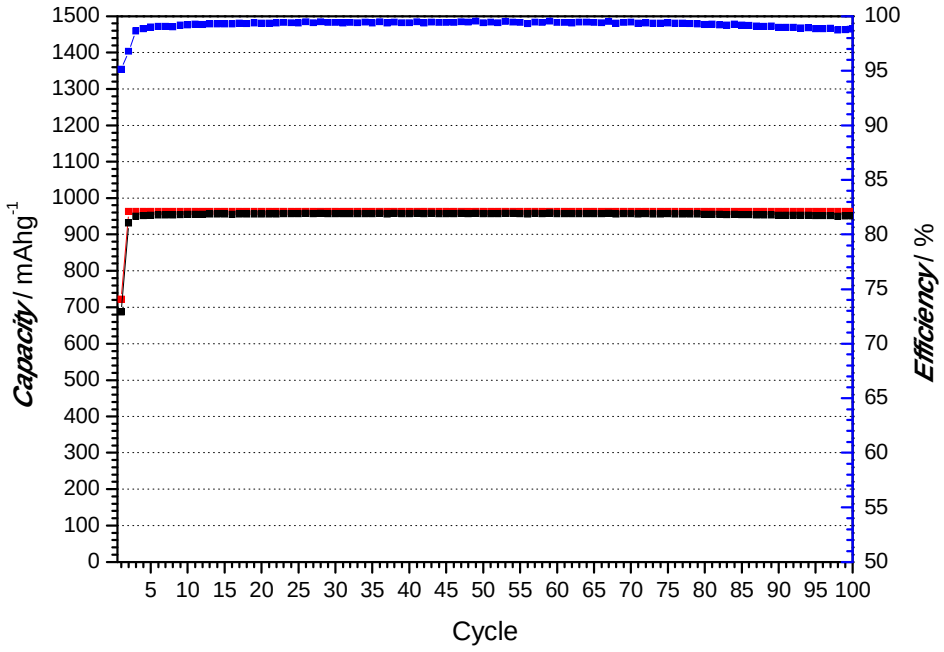

Figure 50: Cycling study of a Si/C composite (CPS) material, 60mV, 0.8C 960 mAhg

By consideration of the cycling results a limitation of the cut off voltage seems reasonable. Combined with a capacity limit, excellent cycling results can be obtained. However the results shown before were made in half cells against lithium. An electrode balancing in a full cell combined with such cycling programs is challenging.

Nevertheless the influence of cycling conditions on the cycle life of silicon/graphite composite electrodes and the need for an intelligent cycling program for silicon and silicon/graphite composite electrodes were impressive shown.

3.2.5 Demonstrator - Preparation and Electrochemical Characterisation of an Full Cell

All cycling studies shown before were measured in half cells against a lithium counter electrode. Such a measurement setup is perfect for the analysis of the electrochemical behaviour of an electrode material, but due to the fact of the lithium reservoir on the counter side there is a huge difference to a real battery, where the amount of mobile lithium is limited. So a full cell cycling experiment, where the amount of mobile lithium in the cell was limited, with the graphite/silicon composite material as negative electrode and an industrial $LiCoO_2$-electrode as cathode was done. As seperator a Separion© separator was used and the electrolyte system consisted of EC/DEC (3:7, v:v), 1M $LiPF_6$ with 2 w% vinylenecarbonate (VC) as film forming agent .

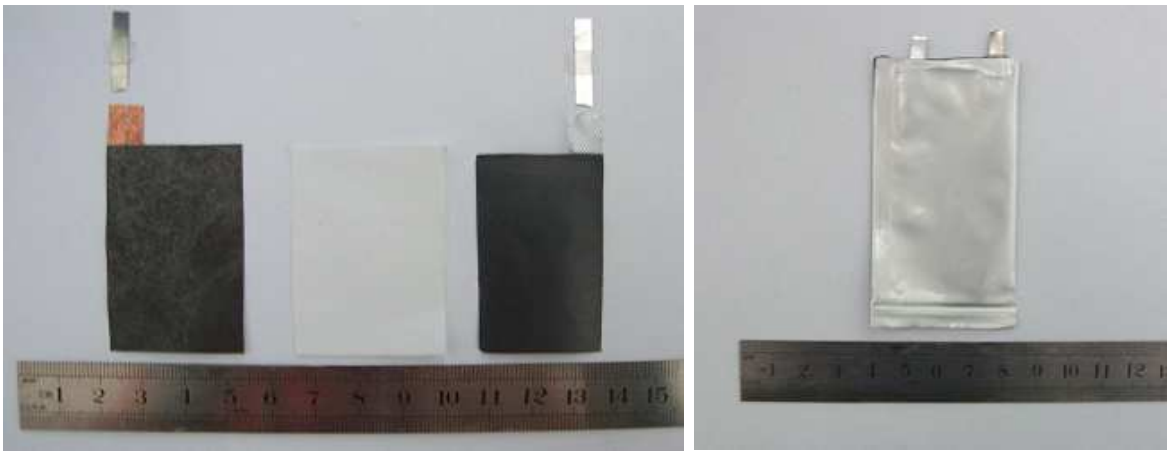

Figure 51: Single components of the full cell (order: anode/sepator/cathode) and finished full cell (right)

For preparation of the full cell the single components were stacked one upon the other (order: anode/separator/cathode). The stack was inlaid in a pouch bag foil and the electrolyte was added under an argon atmosphere and afterwards the pouch bag cell was vacuum sealed (Figure 51, right).

Table 9: Dimensions of the full cell

component	dimension
anode	35 [mm] · 21 [mm]
	capacity: 12.7 mAh
separator	37 [mm] · 23 [mm]
cathode	33 [mm] · 22 [mm]
	capacity: 21.0 mAh

The full cell was cycled in a range of 3.0 V to 4.2 V with a c-rate of 0.5C. In the experiment the capacity was limited to 0.7C of the anode capacity (9.1 mAh).

Table 10: Full cell cycling programm

Cycle	step	c-rate
1 – 100	constant current charging	0.5C to 4.2 V or capacity limit
	constant current discharging	0.5C to 3.0 V

By limiting the capacity to 0.7C of the anode capacity, an active material pool on the anode side was generated, in order to increase the cycling stability during the experiment. The influence of limited cycling on the cycling stability is discussed more in detail within chapter 3.2.4. However, a stable cycling behaviour over 88 cycles, with a decrease of the charge/discharge capacities after the 88th cycle could be observed. In a half cell cycling study with lithium as counter electrode, such a capacity decay can be attributed to an exhausted active material pool, whereas in a full cell cycling study also the loss of mobile lithium can be the reason for such a loss of capacity. The low coloumbic efficiencies given by SEI formation in the first cycles and the constant efficiency in the following cycles (starting cycle 15) were an indicator for a problem with the amount of mobile lithium in the cell, because the loss of active material does not lead to such a continuous efficiency characteristic. With regard to the achieved voltage profiles of the cycling study the reason for the capacity decay could be explained (Figure 53).

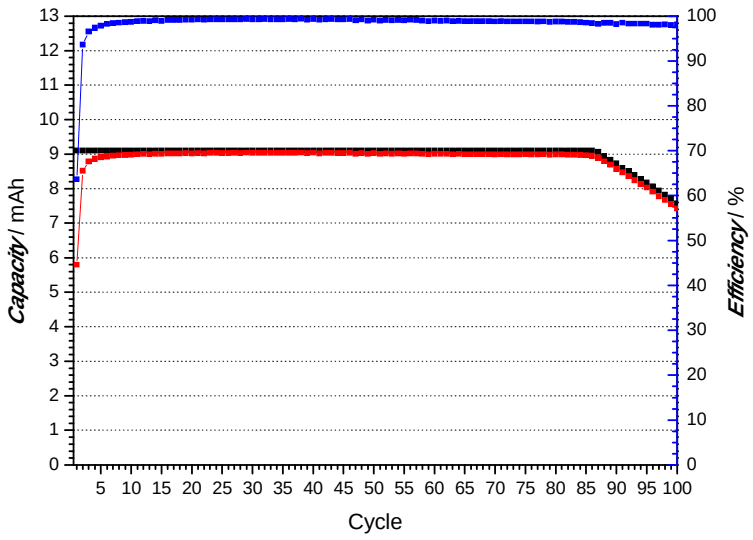

Figure 52: Full cell cycling study

Because of the irreversible loss of mobile lithium in each cycle a potential rise of the cathode occurred, whereby an increase of the overall cell potential could be observed. This irreversible loss of lithium could be dedicated to loss of active material and lithium trapping in the active material but also to a permanent rebuilding of the SEI (electrolyte decomposition). After ~200 hours (=88 cycle) the upper cut off potential of 4.2V was arrived. At this point the cell contained not enough mobile lithium to utilize the full entire anode capacity and so a loss of overall cell capacity could be observed.

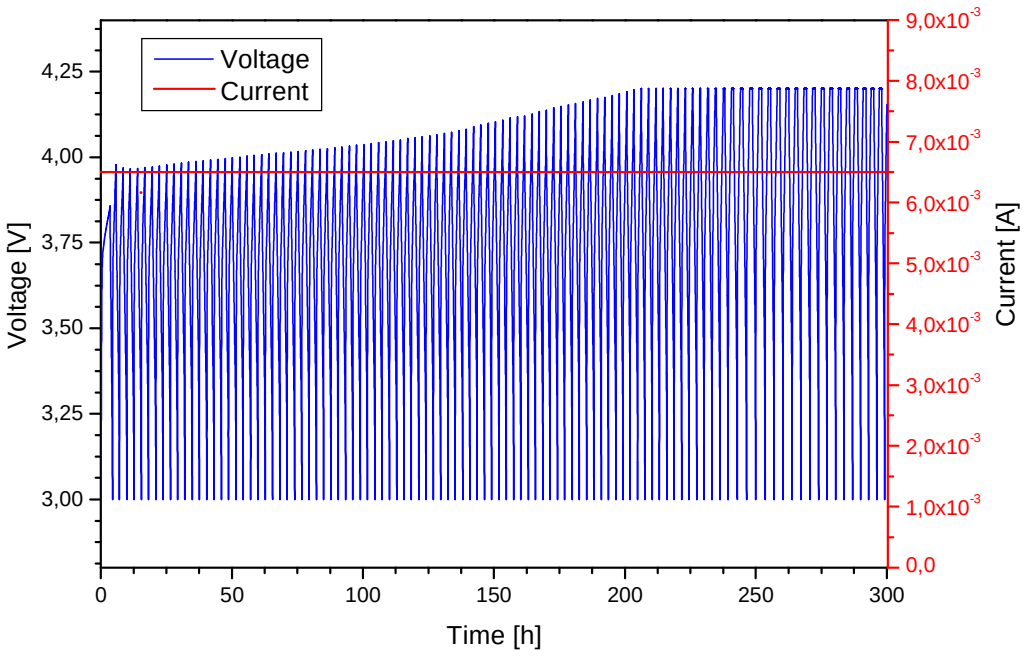

Figure 53: Voltage profile of the full cell cycling study

To increase the cycling stability and to achieve a better cycle life, further improvements for better efficiencies are necessary. Also the possibilities to implement more mobile lithium in the cell to counter the loss of mobile lithium during cycling should be discussed. The use of a bigger overdimensioned cathode could be a possibility, but it must be noted that an overdimensioned cathode can lead to lithium plating on the anode side and will also decrease the specific energy of such a cell.

3.3 Efficiency Problems of High Capacity Si/C Composite Materials

Like shown before the mobile lithium is limited in full cells and high coulombic efficiencies are essential for a long cycle life. A bad reversibility in the first cycle combined with low coloumbic efficiencies in the following cycles connotes a too high loss of mobile lithium. To achieve a long cycle life with low coulombic efficiencies, every mol of lost mobile lithium must be implemented by another way (e.g. overdimensioned cathode).

There are many effects which affect the cycling efficiency during cycling and are responsible for the loss of capacity. In the first cycle mainly the formation of the SEI accompanied with electrolyte decomposition leads to the observed low efficiencies. The quality of the SEI is further decisive for the reversibility of the lithium insertion/extraction in the following cycles.

By the use of composite materials or intermetallic compounds additional effects have to be taken into consideration. Huge volume changes during cycling lead to a permanent rebuilding of the SEI. An inhomogeneous and inflexible SEI, which is not able to handle the large volume changes, dehisce and so free surface area gets in contact with the electrolyte and new SEI is formed. So a selective design of the SEI or a reducing of the surface area is essential.

During lithium insertion/extraction and the associated large volume changes, parts of the active material particles (e.g. silicon) crack and lose their electric contact to the conducting matrix. These cracked parts of the particles are not available to store lithium in the following charge/discharge cycles and a loss of capacity can be observed. In most cases a loss of mobile lithium is also observeable (“lithium trapping”) and is combined with the loss of capacity.

Within the following, the general reasons for “lithium trapping” will be discussed. They are either from thermodynamic or from kinetic nature (100).

Thermodynamic reasons for lithium trapping:

Lithium can be immobilizied in micro- or nanostructered defects, like the immobilization in non metallic impurities, in grain boundaries (alloys) or other internal boundary layers. Also a displacement of particles during cycling, as well as the denoted cracking of lithium containing particles are such reasons. Primarly in the first cycle the fractional solubility of lithium in metals and alloys is also a reason for lithium trapping. Because of the formation of a solid state phase, it is not possible to extract all lithium at the defined cut off potential.

Kinetic reasons for lithium trapping:

Limited lithium diffusion rates, reaction rates or nucleation are major reasons for a not reversible lithium insertion/extraction and are mainly existing by the use of different c-rates during cycling. The diffusion rate depends also strongly on the amount of inserted lithium and is also responsible for the formation of diffusion gradients through a particle.

Due to the fact that lithiation of silicon occurs under formation of four intermetallic phases with different crystal structures, many reactions are running parallel at different reaction zones, and so the possibility of lithium trapping in silicon is enhanced.

3.3.1 Mechanical Stabilization and Enhanced Electrode Conductivity and their Influence on the Coloumbmetric Efficiency

3.3.1.1 Nano Wires as Mechanical Stabilizing Conducting Agent in Electrodes

As shown before, different reasons are responsible for a limited cycle life and low cycling efficiencies. One adjustable screw to increase the cycle life is the stabilization and the increase of the conductivity of the entire electrode by the building of a 3-dimensional matrix by use of metal nano-wires. With a 5 times higher conductivity ($6 \cdot 10^7$ $S \cdot m^{-1}$) compared to common used conducting agents, like carbon black, copper nano wires are an extremely interesting alternative conducting agent. By the fact of their structure, they do not only provide good conductivity they can also improve the mechanical electrode stability and so they are able to compensate the large volume changes of lithium intermetallic compounds during cycling.

3.3.1.1.1 Copper Nano Wire Synthesis

For the preparation of the copper nano wires the synthesis instruction shown in literature (121) was scaled up to obtain a larger amount of nano wires for further electrode fabrication. For this reason a 2000 ml of a 15 $mol \cdot l^{-1}$ NaOH solution was prepared and cooled down to room temperature. The high concentration of NaOH is essential to prevent the copper ions to form copper hydroxide during the preparation. 15 ml of Ethylendiamine (EDA) was added under stirring and afterwards a water based solution of 2.3 g $Cu(NO_3)_2 \cdot 2.5\ H_2O$ was added. The EDA is essential for the control of the product morphology. 2.5 ml of a saturated solution of hydrazine in water was added and the solution was carefully homogenized. The reaction mixture was heated to 60° C for 2 hours. During that time the solution changed its colour from blue into copper brown. After filtration under inert atmosphere 1.1 g of copper nano wires were obtained. To prevent oxidation of the copper nano wires, they were stored under inert atmosphere in a argon dry box. The reaction pathway is shown in Equation 29.

$$2\ Cu^{2+} + N_2H_4 + 4\ OH^- \rightarrow 2\ Cu + N_2 + 4\ H_2O$$

Equation 29

The obtained nano wires are about 20-50 µm long and 300 to 500 nm thick with a nanoscaled rough textured surface (see Figure 54). The rough surface gives the possibility to create a large interface layer between the copper nano wires and the active material. Thereby an improvement of the mechanical stability should be achieved and the contact resistance should be decreased.

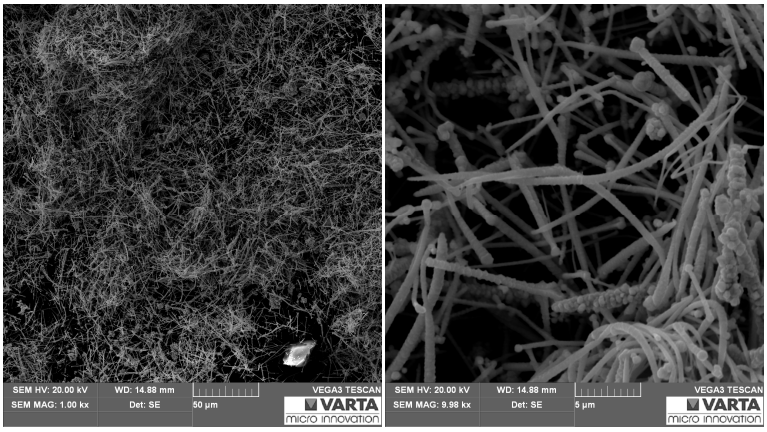

Figure 54: SEM image of copper nano wires - magnification: 1.00 kx and 9.98 kx

3.3.1.1.2 Electrochemical Characterisation of Silicon/Graphite Composite with Copper Nano Wires as Conducting Agent

The electrodes for these electrochemical measurements were composed of 84 % of the Si/C composite material (preparation, see chapter 1.1), as active material, 8 % of copper nano wires as conducting agent and of 8 % Na-CMC as binder.

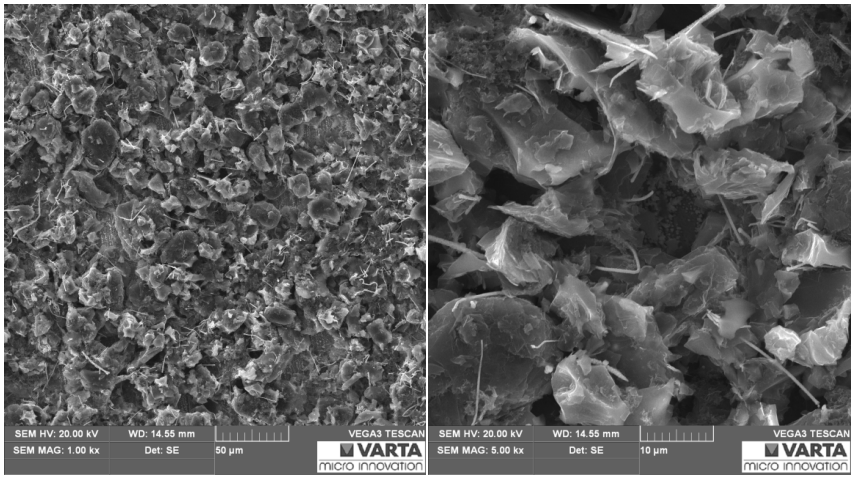

Figure 55: SEM images of a Si/C electrode containing copper nano wires as conducting agent, magnification: x 1000 (left), x 5000 (right)

In Figure 55 the SEM images of the prepared Si/C electrode with copper nano wires as conducting agent are shown. A good distribution of the nano wires in the electrode can be seen (Figure 55, left) and by a closer look at Figure 55 (right) in the middle of the SEM image it is obvious that the flexible mechanical structure of the nano wires is able to withstand a large deformation without breaking.

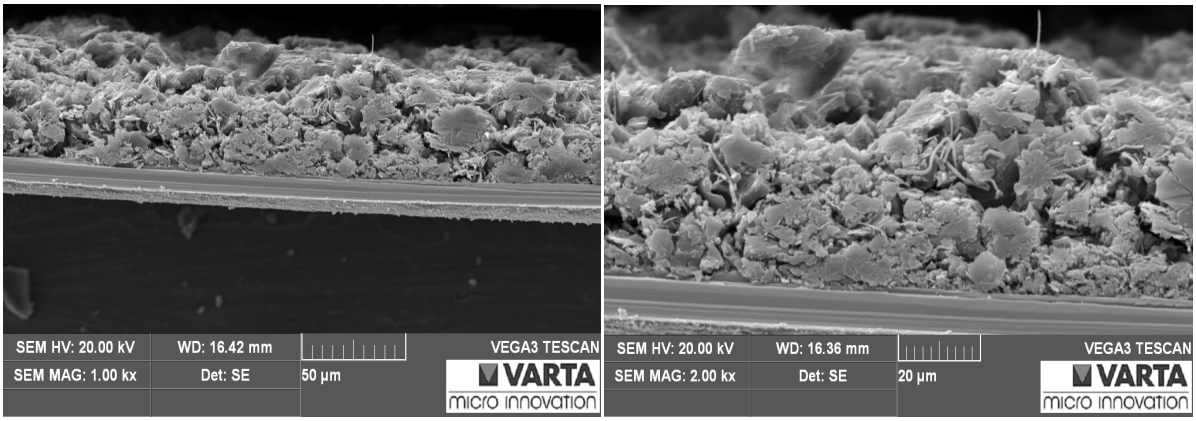

Figure 56: SEM cross section image of a Si/C composite electrode with copper nano wires

The SEM cross section images confirm the good embedding of the nano wires in the electrode and their mechanical flexibility. Not only an enhanced electrode conductivity was the result. Caused by their mechanical flexibility, the nano wires are able to handle the large volume changes during lithiation/delithiation and so the loss of active material, given by losing of interparticle contact, could be decreased.

To examine the electrochemical performance of the electrodes with copper nano wires as conducting agent a constant current cycling measurement was performed. After one formation cycle with a lower c-rate, the cell was cycled with a current of 0.5C and the capacity was limited to 600 $mAh \cdot g^{-1}$. The summarized cycling program is shown in Table 11 and the cycling results in Figure 57.

Table 11: Summarized cycling programm for electrodes with copper nano wires as conducting

cycle	step	c-rate
1	constant current charging	0.2C to 5 mV or 720 $mAh \cdot g^{-1}$
	constant voltage charging	2 h at 5 mV or 720 $mAh \cdot g^{-1}$
	constant current discharging	0.2C to 1500 mV
2 - 100	constant current charging	0.5C to 5 mV or capacity limit
	constant voltage charging	4 h at 5 mV or capacity limit
	constant current discharging	0.5C to 1500 mV

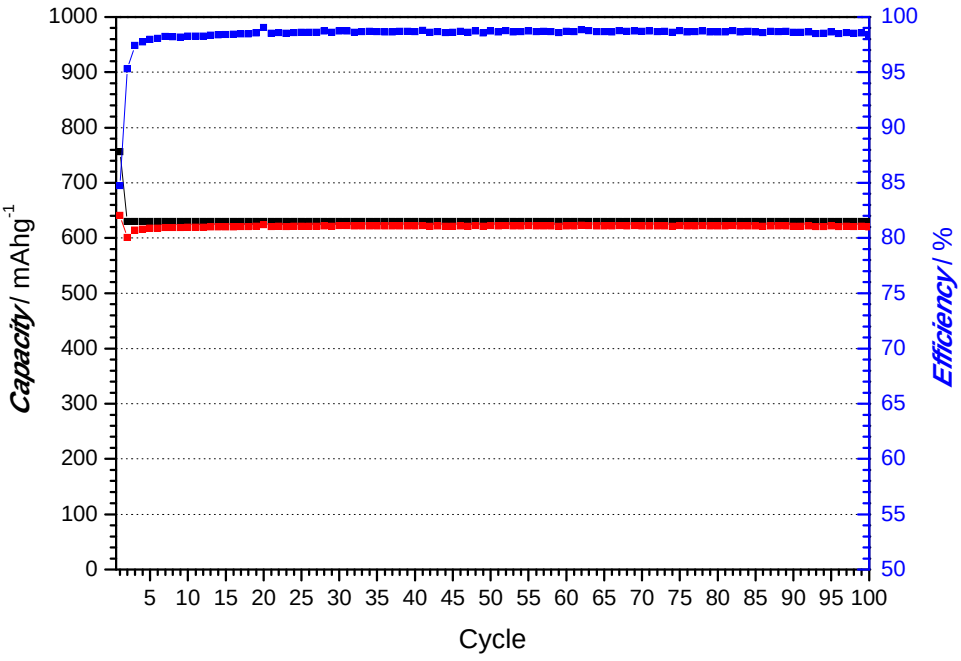

Figure 57: Cycling study of a silicon/graphite - composite with copper nano wires as conducting agent, cap. limit: 600 mAh·g^{-1}

The cycling study of the silicon/graphite composite material with the copper nano wires as conducting agent showed an excellent cycle performance. In the first cycle an efficiency of 84.8 % and a stable cycling of 100 cycles at 600 mAh·g^{-1} could be achieved. These excellent results can be attributed to the perfect contact between the active material particles and the copper nano wires surface. The large interface and the rough surface of the nano wires enable a perfect contact between the active material and the nano wires. The result was a mechanically stabilized composite material with an enhanced cycling efficiency in the first cycles.

To evaluate these cycling results a measurement with Super P as conducting agent was done for comparison. The electrodes were composed of the same amount of the active material (84 w%) and binder (8 w%). The only difference between the electrodes were in the different conducting agent (here 8 w% Super P). The electrodes were cycled with the same cycling conditions (see Table 11).

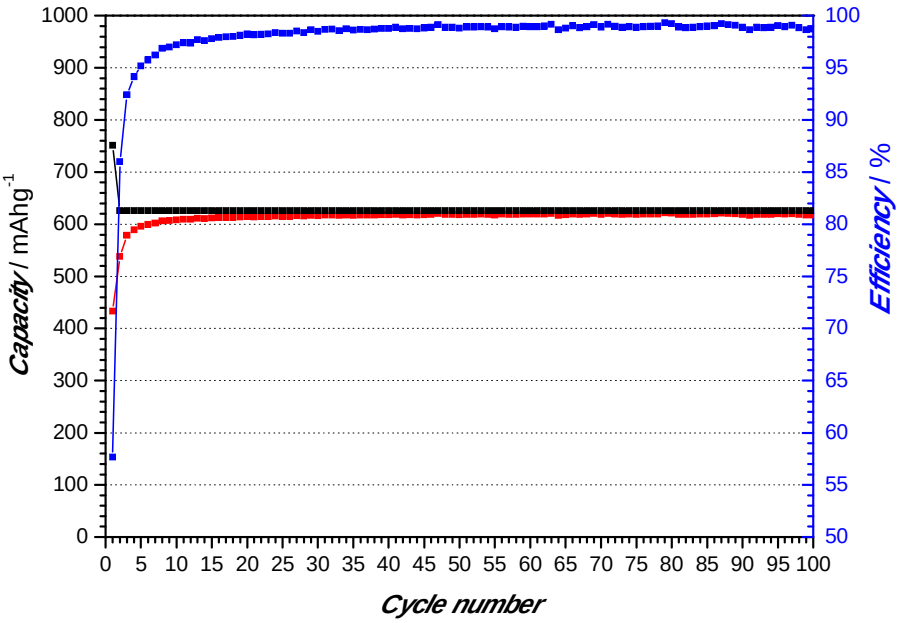

Figure 58: Cycling study of silicon/graphite - composite with Super P as conducting agent, cap. limit: 600 mAh·g^{-1}

Compared to the cycling result with copper nano wires as conducting agent a worse cycling efficiency in the first cycles could be observed. In consideration of the loss of mobile lithium a horrible efficiency of only 57.67 % was achieved in the first cycle, and not until the 10th cycle an adequate efficiency of over 97% was reached. Also a discharge capacity increase could be observed, which is a result of a slow orientation and formation of the active material particles in the electrode matrix.

3.3.1.2 Electrode Stabilization by 3D Current Collector

The influence of mechanical electrode stabilization was shown in the last chapter. A consequent further development for enhancement of electronic conduction and mechanical stabilization of silicon containing high capacity electrodes is the introduction of a 3 dimensional current collector. The 3 dimensional structure of such a current collector provides the ability to assure an excellent mechanical stability and also provides small diffusion ways for the electrons and thereby enhances the electronic conductivity of the whole electrode.

The used 3 dimensional current collector (POLYMET® XII-1 Cu) consisted of a copper metalized polymer non woven with an appropriate structure (see Figure 59).

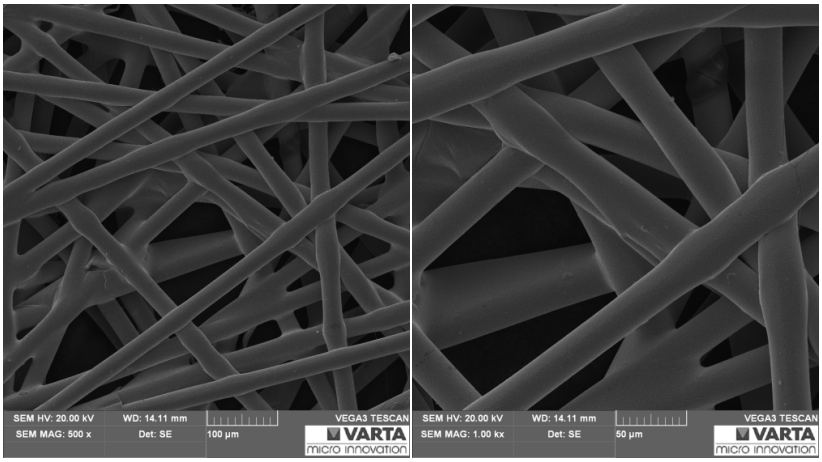

Figure 59: SEM image of the 3D current collector, Magnification: 3000x (right), 500x (left)

The SEM images of the prepared electrode show the excellent connection between the active material and the 3D current collector. Also the small diffusion ways for the electrons, because of the embedding of the active material into the metalized polymer non wovens, are obvious. Due to that reason the electronic conductivity of the whole electrode is enhanced (Figure 60).

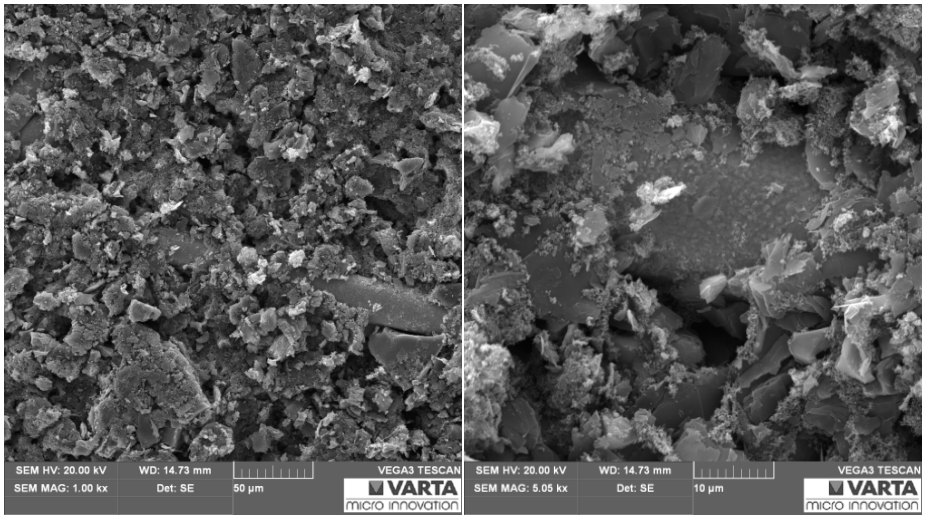

Figure 60: SEM image of the electrode with the 3D current collector, Magnification: x1000 (left), x5050 (right)

The cross section images of the electrode confirm the excellent connection between the electrode material (active material + binder + conducting agent) and the current collector. By better connection between the electrode material and the 3D current collector not only the whole electrode conductivity was increased, also the large volume changes during lithium insertion/extraction could be better compensated, resulting in a mechanical stabilizing effect with decreased loss of active material during cycling.

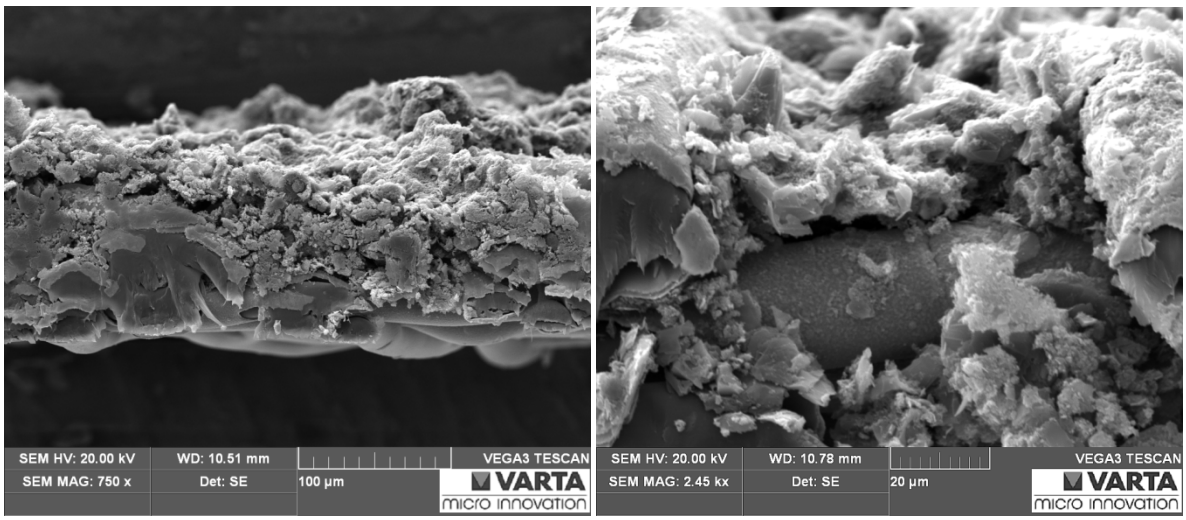

Figure 61: SEM cross section image of a Si/C composite electrode coated on a 3D current collector

In the cyclovoltammetric measurement (Figure 62) no reduction or oxidation peaks coming from the current collector were obvious. The 3D current collector is electrochemically stable between the potential range of 0 - 3V against Li/Li^+. Furthermore the cyclovoltammetric measurement of the silicon/graphite composite shows the typical behaviour of the material, which was produced by the thermal decomposition of CPS on graphite. From the second cycle a high capacity and a good

reversibility of lithium insertion/deinsertion can be observed. Noticeable are the high peak currents, which are an effect of the high mass load of the electrode. In spite of the high mass load of the electrode sharp peaks were observed, which can be attributed to the excellent kinetic of the electrode caused by the large interphase area between the electrode material and the 3D current collector.

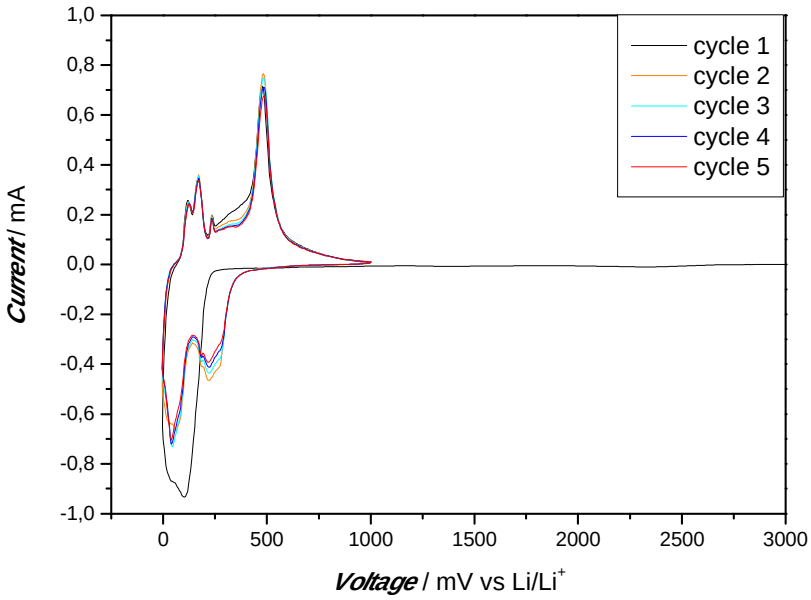

Figure 62: Cyclovoltammetric measurement of a silicon/graphite – composite electrode coated on the 3D current collector, scan rate: 10 µV·s^{-1}

To examine the long time cycling behaviour of electrodes coated on the 3D current collector a constant current charge/discharge measurement was done. After one formation cycle the capacity was limited to 0.5C (corresponds to 600 mAh·g^{-1}). The full cycling program is summarized in Table 12.

Table 12: 3D current collector cycling experiment, summarized cycling program

cycle	step	c-rate
1	constant current charging	0.2C to 5 mV or 720 mAh·g^{-1}
	constant voltage charging	2 h at 5 mV or 720 mAh·g^{-1}
	constant current discharging	0.2C to 1500 mV
2 - 100	constant current charging	0.5C to 5 mV or 600 mAh·g^{-1}
	constant voltage charging	4 h at 5 mV or 600 mAh·g^{-1}
	constant current discharging	0.5C to 1500 mV

The cycling study of the silicon/graphite composite material coated on the 3D current collector shows an excellent cycling stability and comparable coulombic efficiencies to the cycling results of electrodes with copper nano wires as conducting agent. In the first cycle a lower efficiency of 80.3% compared to 84.7% efficiency of the electrodes with copper nano wires as conducting agent was achieved. However in the 2nd cycle the efficiency increased to 96.2% and reached a steady state of 98.8% in the 10th cycle, which is higher compared to the electrodes with copper nano wires as conducting agent. These excellent results can be attributed to the large interphase between the active material particles and the current collector as well as to the formation of a stable 3 dimensional network through the embedded active layer.

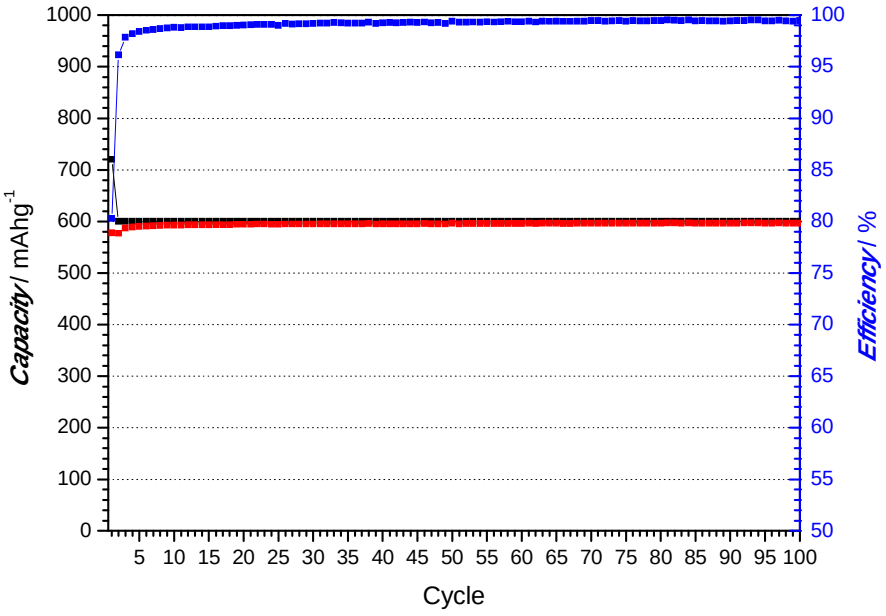

Figure 63: Cycling study of a silicon/graphite – composite electrode coated on the 3D current collector, cap. limit: 600 mAh·g^{-1}

3.3.1.3 Summary and Conclusion

Previously the influence of mechanical stabilization and enhancement of the electronic conductivity on the cycling efficiency was shown by two different ways. The build up of a 3D electrode setup seems to be an appropriate possibility to increase the cycleability of silicon/graphite composite electrodes.

By consideration of the problems with low coloumbic efficiencies during cycling of full cells, a closer look should be taken on the previous reported results. Therefore the efficiencies of the first cycles of the previous cycling experiments were compared.

Table 13: Comparison of the cycling efficiency with different electrode stabilization approaches

cycle	Super P	Copper Nano Wires	3D Current Collector
1	57.97 %	84.73 %	80.30
2	85.98 %	95.30 %	96.14
3	92.41 %	97.43 %	97.48
7	96.20 %	98.23 %	98.61
10	97.20 %	98.26 %	98.8

The huge influence of mechanical electrode stabilization and increased electrode conductivity concerning to the cycling efficiency is obvious by a look on Table 13. Meanwhile a not stabilized electrode only achieve a cycling efficiency of 57.97%, the use of copper nano wires or an 3D current collector enhances the efficiency to more than 80%. After the third cycle an efficiency of over 98% can be achieved. Given by the fact that the efficiency in the first cycles also strongly depends on the electrolyte system, the achievement of a better cycling efficiencies by an optimized electrode setup is quite difficult. So further improvements can only be achieved by controlling of the electrode surface/electrolyte interactions, either by an optimized electrolyte composition, in respect of SEI formation and permanent SEI rebuilding or by decreasing of the electrode surface by the use of not nano sized materials with all its negative factors. Thus it can be stated that an active material design, as shown in chapter 1.1, with not nano sized particles but an outstanding cycle performance seems to be the right approach to overcome such efficiency problems of silicon/graphite electrodes. A more detailed electrochemical study of these complexes of problems is given in chapter 3.3.2.

However, by comparison of the cumulated irreversible capacities (Figure 64) the positive effect of copper nano wires or the 3D current collector is pointed out more clearly. By use of Super P as conducting agent the cumulated irreversible capacity was already 1021.3 mAh·g^{-1} after 50 cycles, meanwhile the cumulated irreversible capacity for copper nano wires as conducting agent was only 598.5 mAh·g^{-1}. By use of a 3D current collector the range of this cumulated irreversible capacity values was achieved after ~100 cycles (615.6 mAh·g^{-1}).

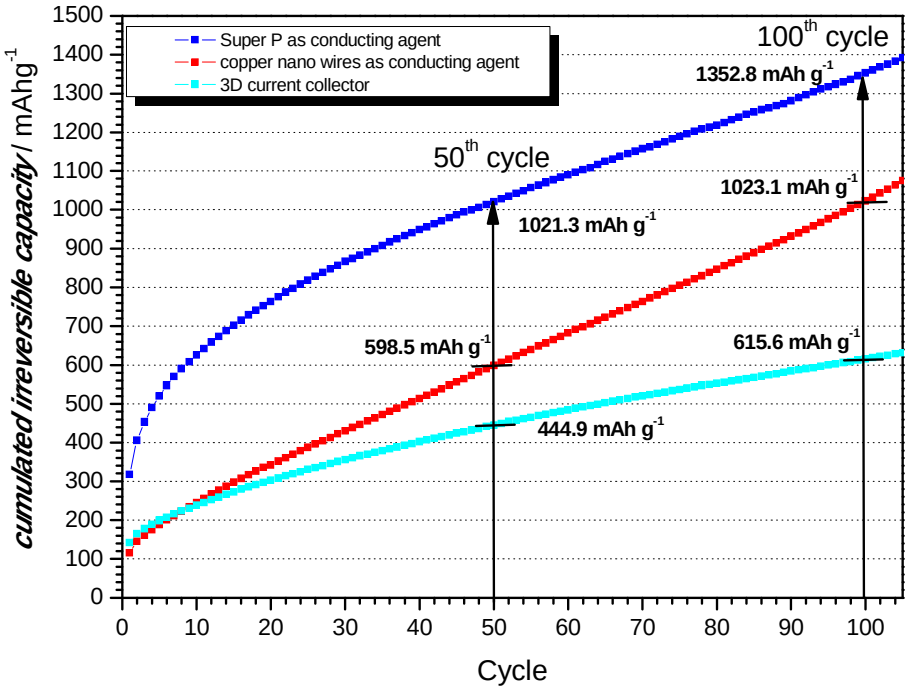

Figure 64: Comparison of the cumulated irreversible capacities of mechanical stabilized electrodes

It must be noted that in a real battery, every mAh·g^{-1} of cumulated irreversible capacity in the cell is combined with a loss of mobile lithium. The impact of such irreversible capacity values is clearly obvious in full cell measurements, like shown in Figure 52 (see chapter 3.2.5).

3.3.2 Low Coulombic Efficiencies caused by Parasitic Surface Reactions: an Electrochemical Point of View

Until now the poor cycling efficiency of silicon/graphite composite materials prevent them from a commercial breakthrough. Because of the poor capacities of the state of the art cathode materials every loss of lithium in a full cell affects double. So a high efficiency of such a composite material is essential. In the last chapter the positive influence of mechanical electrode stabilization and enhancement of the electrode conductivity was shown by various measurements. N. Hochgatterer (100) demonstrated that for nano silicone/graphite composite electrodes only ~50% of the irreversible capacity can be attributed to active material loss. Half of the irreversible efficiency can be attributed to electrolyte decomposition or other parasitic reactions on the electrode surface. To counter these effects either it is necessary to create the perfect SEI, which does not exist by now, or to reduce the surface area of the electrode. By tuning of the electrolyte it is possible to decrease the irreversible capacity to a minimum, but this minimum of irreversible capacity is still too much. Due to the reason that the huge surface area of nano particles intensify the problem of electrolyte decomposition, a promising approach to overcome this problem seems to be the development of a silicon/graphite composite material with reduced electrode/electrolyte surface area.

By comparison of a nano silicon/graphite composite material and the previous developed silicon/graphite active material (see chapter 1.1) the effect of a reduced surface area will be pointed subsequent. The composition of the electrodes is shown in Table 14.

Table 14: Electrode compositions for cycling efficiency measurement

	Composition
Active Material	nano Si/C or Si/C composite material [84 w%]
Conducting Agent	Super P [8 w%]
Binder	Na-CMC [8 w%]

For the comparison of the cycling efficiency constant current charge/discharge measurements were done. After one formation cycle the capacity was limited to 0.7C (840 $mAh \cdot g^{-1}$) of the theoretical capacity. In Table 15 the summarized cycling program is shown. By limiting the capacity it is possible to generate an active material pool and so to fade down the loss of active material during cycling.

Table 15: Summarized cycling program of the efficiency comparison measurements

cycle	step	c-rate
1	constant current charging	0.2C to 5 mV or 720 mAh·g^{-1}
	constant voltage charging	2 h at 5 mV or 720 mAh·g^{-1}
	constant current discharging	0.2C to 1500 mV
2 – 100	constant current charging	0.5C to 5 mV or capacity limit
	constant voltage charging	2 h at 5 mV or capacity limit
	constant current discharging	0.5C to 1500 mV

After one formation cycle, where the capacity was limited to 0.6C (720 mAh·g^{-1}) a stable cycling over 100 cycles at 840 mAh·g^{-1} can be observed (see Figure 65). Already from the 3rd cycle a cycling efficiency of over 98% and from the 9th cycle an efficiency of over 99% was measured for the silicon/graphite material, which was formed by thermal decomposition of CPS on natural graphite. In the following cycles and up to cycle 100, the cycling efficiency remained constant over 99%.

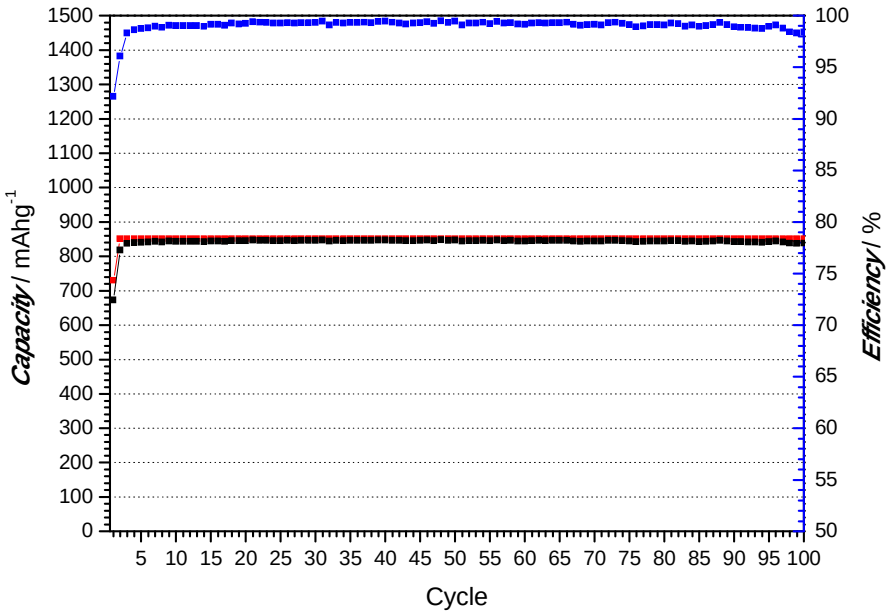

Figure 65: Cycling study of silicon/graphite material, formed from CPS, capacity limited 840 mAh·g^{-1}

Also in the constant current cycling measurement of the nano silicon/graphite electrode a stable cycling of over 100 cycles at 840 mAh·g^{-1} was achieved. However compared to the previous shown measurement (Figure 66) a slight decline of the efficiency in the first cycles up to 50th cycle could be

observed. The reason for the better efficiency in the first cycles could be attributed to the reduced surface area of the silicon/graphite composite material, which was formed by thermal decomposition of CPS on natural graphite. The larger surface area of the nano-silicon/graphite electrode, given by the used silicon nano particles, and the increased electrode/electrolyte reaction surface led to increased electrolyte decomposition because of parasitic reactions and of rebuilding of the SEI during cycling, resulting in a lower efficiency.

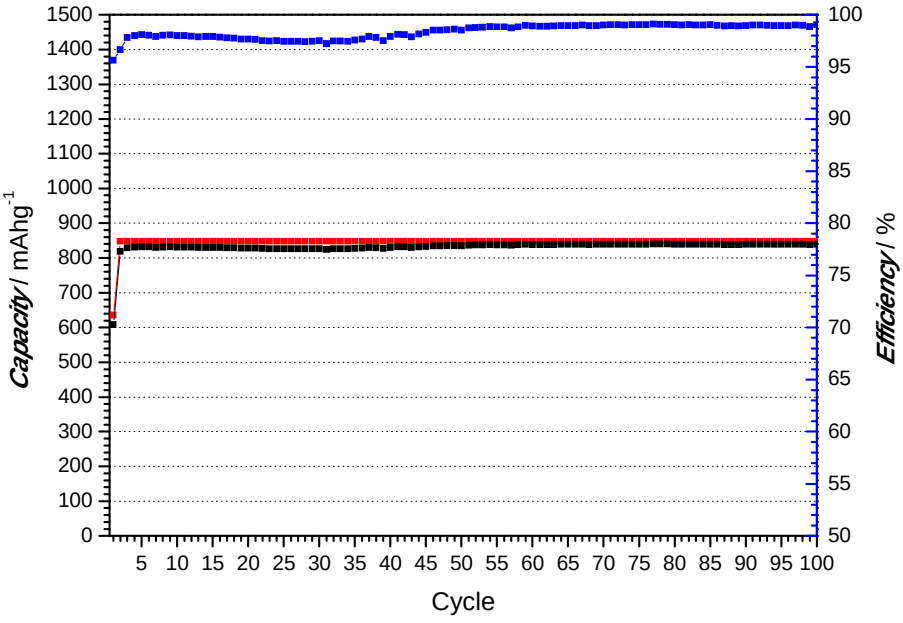

Figure 66: Cycling study of a nano Si/Graphite material, capacity limited to 840 mAh·g^{-1}

The results of the efficiencies, obtained from the cycling experiments, were summarized in Table 16.

Table 16: Comparison of the cycling efficiencies

cycle	Si/C composite	Nano Si/C composite
5	98.76	98.07
10	99.04	97.99
20	99.24	97.66
30	99.34	97.50
40	99.47	97.90
50	99.46	98.51

Although the nano silicon/graphite composite electrode achieved a good efficiency of over 98 % in the 5th cycle, the efficiency problem of the nano Si/C composite electrode is obvious, starting from the 10th cycle up to cycle 50. From the 10th cycle, the efficiency decreases below 98 % and recovers not until the 50th cycle. This range of 40 cycles with a worse efficiency reflects of course the worse irreversible capacity shown in Figure 67.

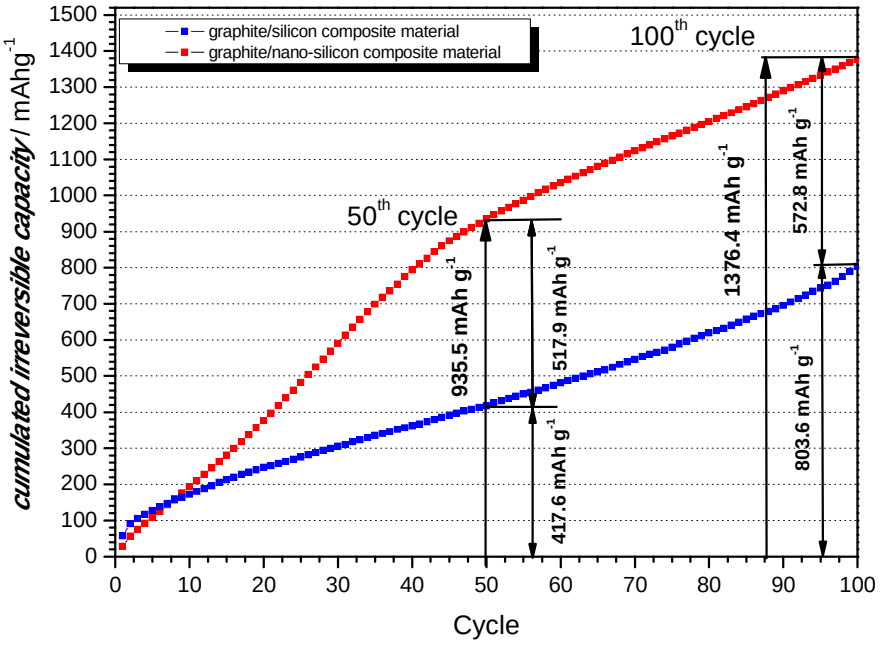

Figure 67: Comparison of the cumulated irreversible capacity

By comparison of the cumulated irreversible capacities it is obvious that from cycle 10 up to cycle 50 the worse efficiency of the nano silicon/graphite composite electrode leads to a huge difference in the cumulated irreversible capacity. Meanwhile during cycle 50 – 100 the difference of the cumulated irreversible capacity approximately remains the same. Like noted in the previous chapter, a higher irreversible capacity means a much higher loss of mobile lithium during cycling.

The results of this chapter clearly indicate the influence of an intelligent active material design on the efficiency and on the irreversible capacity. To verify these results in-situ gas pressure measurements during cycling were performed. The results and interpretation are shown in the next chapter.

3.3.2.1 Verification by In situ Gas Pressure Measurement

By the challenging reason of separating low efficiencies coming from active material loss and low efficiencies coming from electrolyte decomposition, in situ gas pressure measurements were performed in a modified 3 electrode *Swagelok*®-T-cell (Figure 29). During electrolyte decomposition, because of film formation or parasitic reactions on the electrode surface, not only solid decomposition products, but also gaseous products were formed which led to increased cell pressure. With the "Temperature Controlled Pressure Characterisation" (TPC) it was possible do detect smallest amounts of gaseous products coming from electrolyte decomposition. With this tool a verification of the previous results could be made.

A nano silicon/graphite composite electrode and a silicon/graphite (formed by thermal decomposition of CPS) composite electrode containing 84 w% active material, 8 w% Na-CMC as binder and 8 w% carbon black (Super P) as conducting agent were cycled at constant temperature.

Because lithium was chosen as counter electrode, also the electrolyte decomposition products on the counter side were detected. Given that both cells were cycled with the same cycling program and c-rates, the pressure, coming from electrolyte decomposition on negative side, could be suggested as equal. Therefore these decomposition products have no influence on the interpretation of the results.

In the first charge step the cells were formed with a c-rate of 0.2C and a subsequent constant voltage charge step, at 5mV for 2 hours, and also discharged with a c-rate of 0.2C up to 1500 mV. The capacity was limited to 720 $mAh \cdot g^{-1}$ in the first formation cycle. After the first formation cycle the cells where cycled in a potential between 5 mV and 1500 mV with a c-rate of 0.5C and a constant voltage charging step at 5 mV for 2 hours. The used cycling program is summarized inTable 17.

The generated gaseous products and the resulting pressure, coming from the electrolyte decomposition products, were recorded with an in-situ pressure sensor.

Table 17: Summarized cycling program - in situ gas pressure measurement

cycle	step	c-rate
1	constant current charging	0.2C to 5 mV or 720 mAh·g^{-1}
	constant voltage charging	2 h at 5 mV or 720 mAh·g^{-1}
	constant current discharging	0.2C to 1500 mV
2 - ...	constant current charging	0.5C to 5 mV or 840 mAh·g^{-1}
	constant voltage charging	2 h at 5 mV or 840 mAh·g^{-1}
	constant current discharging	0.5C to 1500 mV

Nano Silicon/Graphite Composite Electrode:

After a rest step of 1 hour, where the potential and the pressure of the cell was monitored, a starting internal pressure of 1038 mbar was detected. After 6 cycles the internal pressure increased about 22 mbar up to 1060 mbar. The increased pressure is a result of gaseous electrolyte decomposition products coming from SEI formation in the first cycle and permanent SEI rebuilding in the following cycles. The wavelike pressure curve can be attributed to the volume expansion (pressure increase) and the simultaneous rebuilding of the SEI during lithiation, meanwhile the pressure remains approximately stable, when the volume contraction occurs during delithiation. Also gaseous products may be desolved in the electrolyte and so the pressure also decreases.

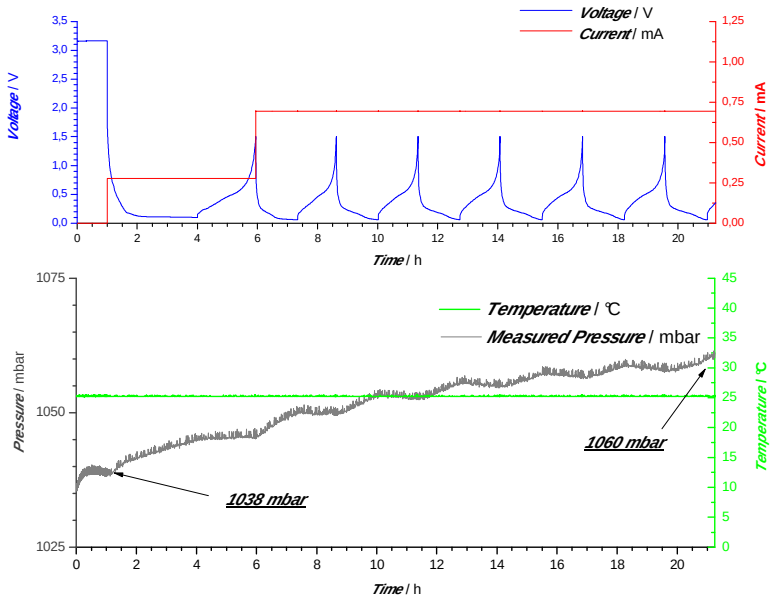

Figure 68: Gas pressure measurement of a nano Silicon/Graphite composite electrode

Silicon/Graphite Composite Electrode:

Also in the second in situ gas pressure measurement experiment, during a 1 hour initial rest step, the pressure and the cell potential was monitored. A starting internal pressure of 1044 mbar, which increased during 6 cycles up to 1051 mbar, was measured. The previous observed wavelike pressure curve cannot be seen in this measurement (Figure 69), what is a result of the better embedment of the silicon in the electrode (keywords: layer structure, silicon embedded in graphite pores).

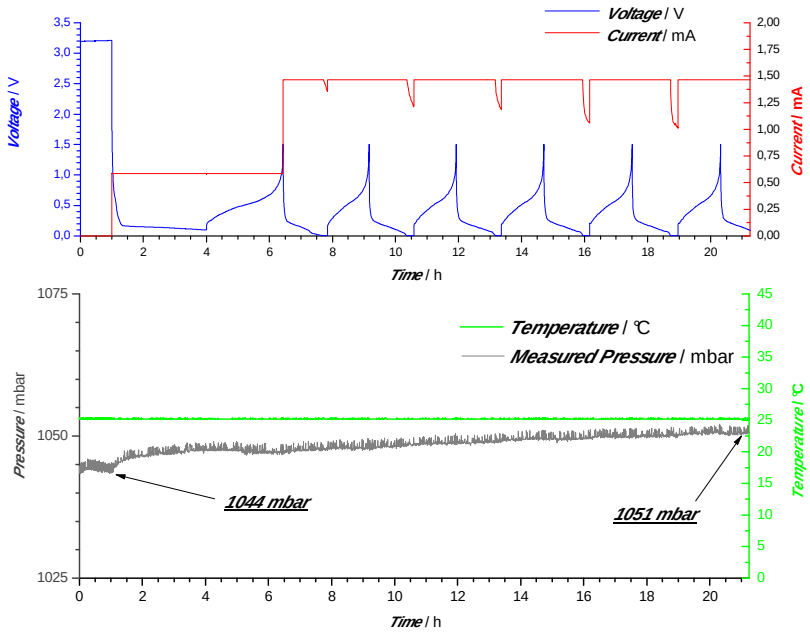

Figure 69: Gas pressure measurement of a Si/C composite material (CPS decomposition)

Compared to the nano silicon/graphite experiment, for the silicon/graphite composite material the internal pressure increase was much lower, although the observed cumulated irreversible capacity was approximately the same after the first six cycles (see Figure 67, chapter 3.3.2). These results suggested that the electrolyte decomposition and permanent refilming of SEI during cycling was a massive problem on use of nano sized materials like nano silicon. In contrary the loss of active material in the first cycles is the major problem of the silicon/graphite composite material, which was produced by thermal decomposition of CPS. The current curve in Figure 69 confirmed these results. The period of constant voltage charging increased during the cycles, which meant that the silicon, deposited on the surface of the graphite, spalled during lithiation. A longer constant voltage charge step was necessary and an irreversible loss of active material could be observed.

However the in situ gas pressure measurement experiments clearly showed the negative influence of electrolyte decomposition on the irreversible capacity of nano silicon electrodes. Conversely the positive influence of the right active material design on parasitic reactions during cycling was shown.

3.4 Germanium as possible Active Material

As in chapter 2.2.3 noted, there is a large interest in the development of binary lithium intermetallic systems for the application in secondary lithium ion batteries, especially for the tin and silicon based systems. The analogues Li_xGe_y system has received only little attention. The fully lithiated $Li_{4.4}Ge$ has a theoretical capacity of 1600 $mAh \cdot g^{-1}$ which is ~40% compared to the lithiated silicon system (70).

The main advantage of germanium is the diffusivity of lithium in germanium, which is 400 times higher than the diffusivity of lithium in silicon at room temperature (73). This fact makes germanium to an attractive electrode material for the use in high power lithium ion batteries or as an addition to silicon electrodes to increase the lithium diffusivity of such electrodes.

To consider practical aspects of using this material in secondary lithium ion batteries, micro-scaled germanium particles were used for the electrode preparation. Because of costs and processability these particles were more appropriate choice than thin films electrodes prepared by CVD.

The germanium particles were synthesized by low temperature reduction of germanium tetrachloride with a slight excess (ca. 5 mol%) of alkali metals in ethereal solvents. After dissolving the concomitantly formed alkali chloride salts in deionized water followed by filtration, the thus obtained crude material was dried in vacuum and used for the electrochemical studies. The obtained germanium particles were ground by mortar and characterized by SEM and EDX measurements.

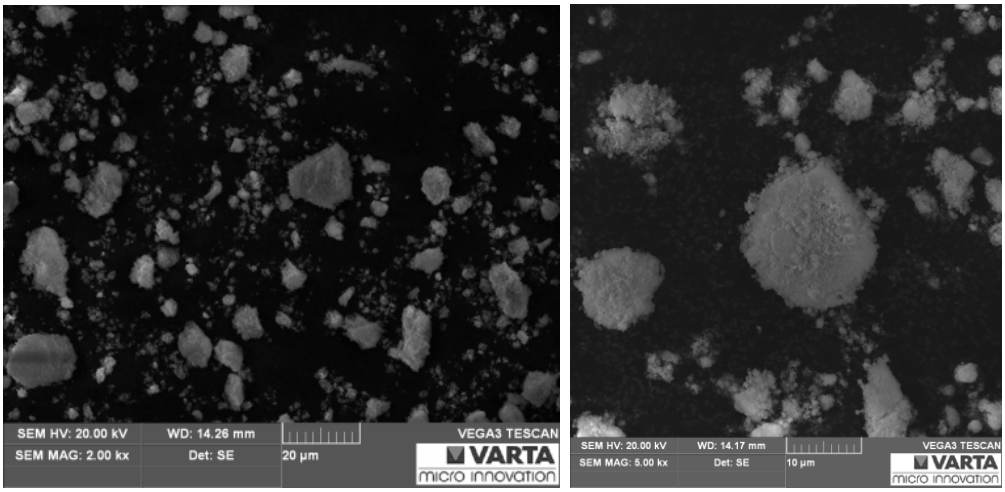

Figure 70: SEM image of the prepared germanium particles

The SEM images showed a broad particle size distribution, but all particles were below 20 micrometer. The energy dispersive X-ray spectroscopy showed that no pure germanium particles were obtained. Oxygen was found too, what indicated a germanium-oxide layer on the surface. Due to the fact that germanium is stable under air, the germanium-oxide layer had to be a result of the synthesis.

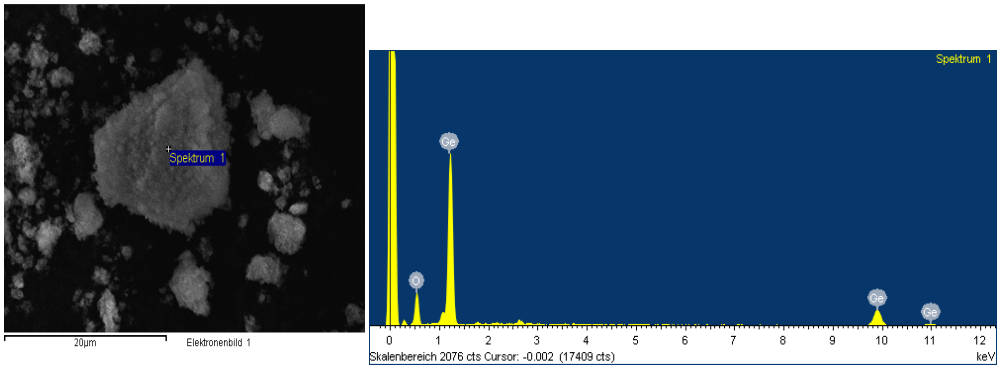

Figure 71: EDX measurement of the prepared germanium particle

The crystal structure characterization of the germanium - particles were done by X-ray diffraction (XRD).

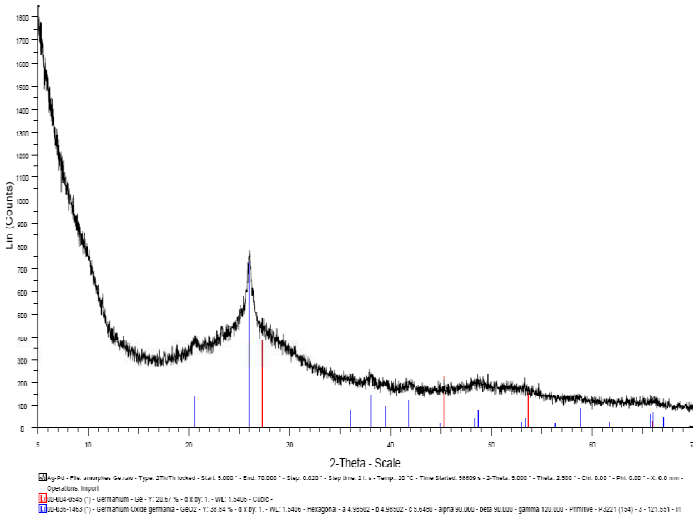

Figure 72: XRD measurement of germanium particles

The XRD measurements confirmed the presumption from EDX measurements. The obtained germanium particle are amorphous germanium particles with a crystalline germanium(II)oxide-surface layer on it.

Electrochemical Characterisation:

Two different binder types were used for the preparation of the electrodes. On the one hand an organic processable PVdF-HFP in *N*-methyl pyrolidone (NMP) was used, and on the other hand an aqueous processable Na-CMC binder. The electrode slurries were prepared via an optimized dispersing technique. The compositions of the slurries are shown in Table 18

Table 18: Slurry composition of the germanium slurries

	NMP based Slurry	Water based Slurry
Active Material	Germanium [84 w%]	Germanium [84 w%]
Conducting Agent	Super P [8 w%]	Super P [8 w%]
Binder	PVdF-HFP [8 w%]	Na-CMC [8 w%]

For the electrochemical characterization cyclic voltammetric measurements and galvanostatical charge/discharge experiments, using EC/DEC = 3/7 (v/v) +2 wt% VC, 1M $LiPF_6$ as electrolyte, were performed. The measurements were done in a three electrode configuration *swagelok*©-T-cell using a lithium metal foil as counter and reference electrode and the germanium electrode as working electrode.

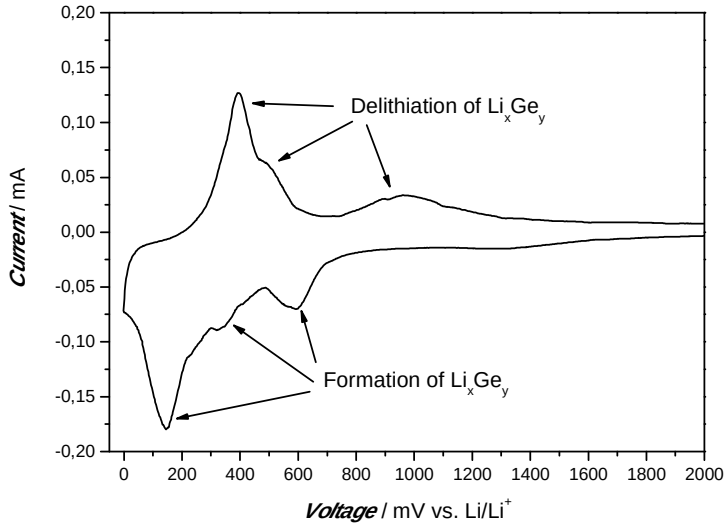

Figure 73: Cyclovoltammetric measurement of a water processed germanium electrode, 30 µV·s^{-1}

In the cyclovoltammetric measurement three lithium intercalation/extraction peaks could be observed. The formation of the Li_xGe_y intermetallic compound occurred between a wide potential range (starting at a potential of 800 mV). The observed broad peaks were a result of the used micro scaled particles, and also the distinctive germanium oxide layer was responsible for the worse kinetic of the electrode.

For comparison a cyclovoltammetric measurement of a germanium electrode produced with commercial available germanium particles (ABCR, Ge-1080, purity: 99.999%, 50 micron) was done. The electrode was composed of 84 wt% the germanium particles, 8 wt% *Super P* as conducting agent and 8 wt% *CMC* as binder.

The SEM images clearly indicate agglomerated germanium particles. The particle shape could be attributed to the purification and further treatment of the particles by the manufacturer to gain particles with 99.999% purity and a particle size of 50 microns (Figure 74).

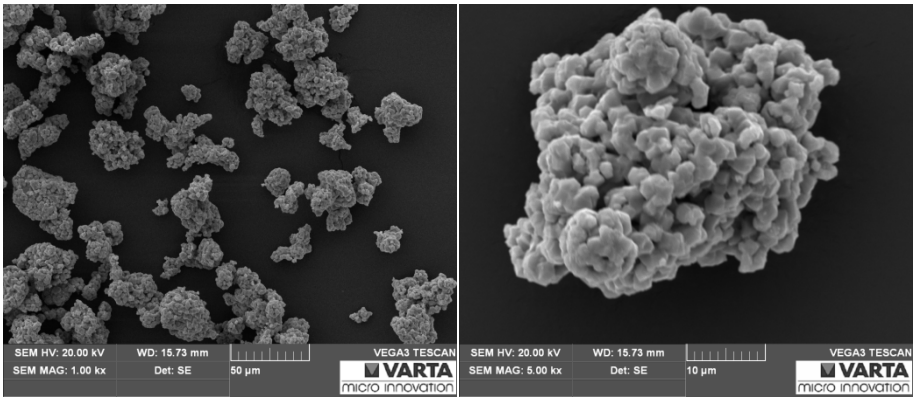

Figure 74: SEM image of the commercial available germanium particles

In the cyclovoltammetric measurement also three lithium intercalation/deintercalation peaks could be observed. The missing surface oxide layer on the commercial avaiable germanium particles led to sharp peaks for the formation of the intermetallic Li_xGe_y phases at potentials of 450, 230 and 150 mV against Li/Li^+. Instead of a clearly separated second and third delithiation peak, only one peak at a potential of 580 mV against Li/Li^+ could be observed. The second delithiation peak was indicated only by a small change in the shoulder of this peak at a potential of 490 mV.

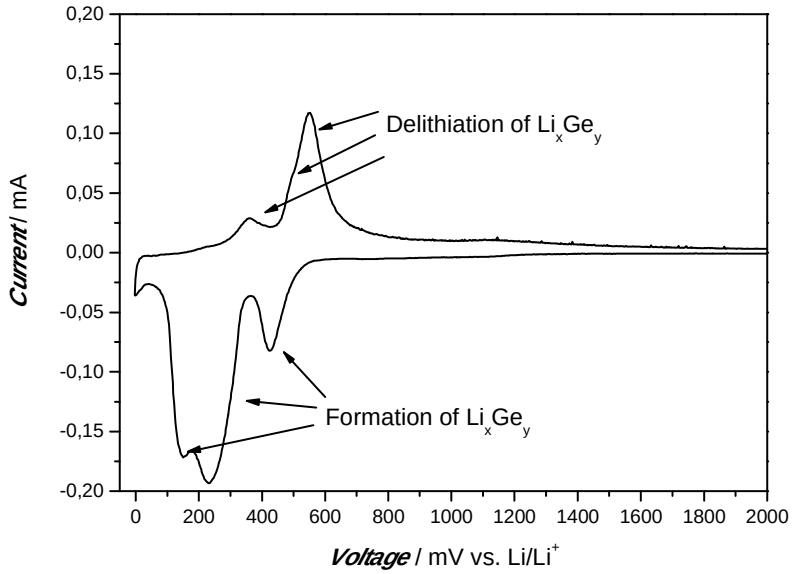

Figure 75: Cyclovoltammetric measurement of germanium electrode processed with commercial available germanium, 30 µV.s^{-1}

However, although the particle size of the commercial available germanium particles was larger than of the synthesized particles, a better electrode kinetic could be observed. For an explanation of this effect a GITT experiment of an electrode with the synthesized germanium particles as active material was performed.

Determination of Internal Electrode Resistance - GITT measurements:

To gain information about internal resistances and diffusion abilities of the germanium electrode a galvanostatic intermittent titration technique (GITT) experiment was done. The summarized GITT measurement program is shown in Table 3 in chapter 3.1

Table 19: Summarized GITT program

cycle	step	c-rate
1 -	Lithiation	0.05C for 40min
	Relaxation	120 min
	Rerun until the potential is ≤ 0 mV vs. Li/Li$^+$	

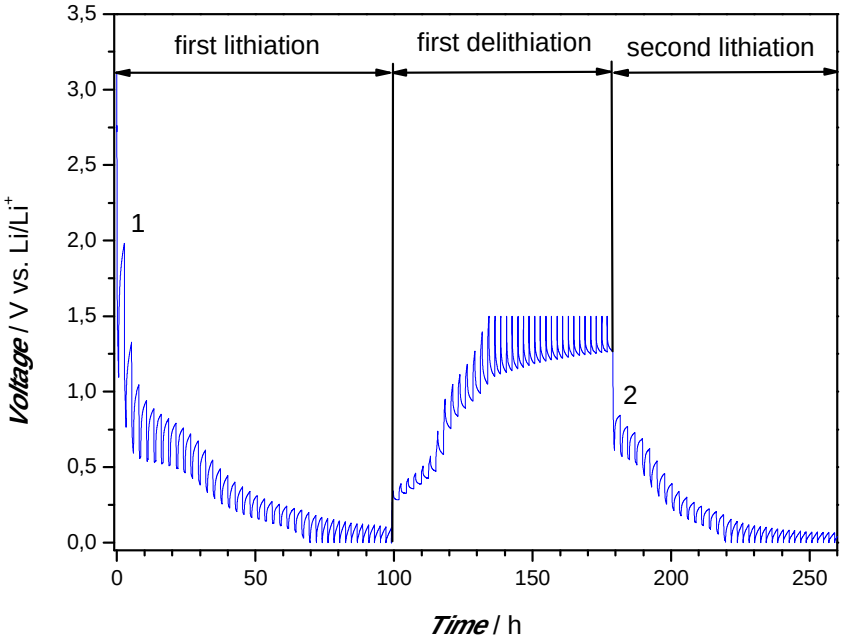

Figure 76: GITT experiment of a germanium electrode

The galvanostatic intermittent titration technique experiment confirmed the results coming from the cyclovoltammetric measurement. At the beginning of the second lithiation (area 2) the steady state was reached faster than at the beginning of the first lithiation (area 1). The oxide layer on the surface of the germanium particle led to a diffusive inhibition during the first lithiation. Once the oxide layer was broken or reduced and the SEI was formed, the kinetic behavior of the electrode was increasing and a lower IR-drop could be examined.

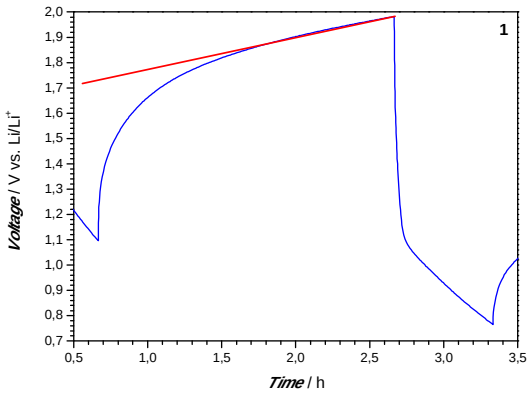

Figure 77: Relaxation profile of a germanium electrode, 1: start first lithiation

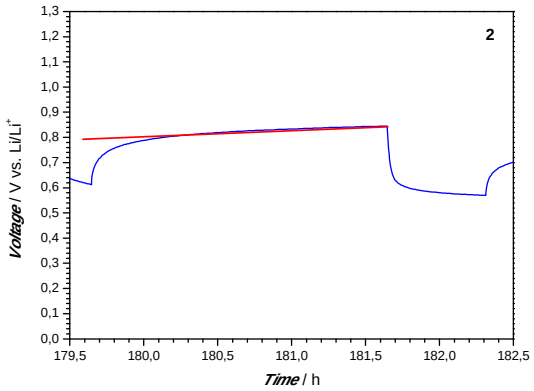

Figure 78: Relaxation profile of a germanium electrode, 2: start second lithiation

Galvanostatical Charge/Discharge Tests:

In the galvanostatical charge/discharge measurements the electrodes were cycled with a c-rate of 0.1C between a potential range of 5 – 1500 mV vs Li/Li^+ and a period of constant voltage charge at 5 mV vs. Li/Li^+ for 4 hours. The capacity was limited to 800 $mAh \cdot g^{-1}$, which corresponded to 50% of the theoretical capacity of germanium. The cycling program is summarized in Table 20. The used c-rates were calculated with a theoretical capacity of 1600 $mAh \cdot g^{-1}$.

Table 20: Summarized cycling program - germanium electrodes

cycle	step	c-rate
1 - 40	constant current charging	0.1C to 5 mV
	constant voltage charging	4 h at 5 mV or 800 $mAh \cdot g^{-1}$
	constant current discharging	0.1C to 1500 mV

The research results obtained from galvanostatical charge/discharge experiments demonstrate that it is possible to cycle germanium particles over 40 cycles with an appealing cycling stability and a low capacity fading (Figure 79 and Figure 80), when the capacity is limited to 800 $mAh \cdot g^{-1}$.

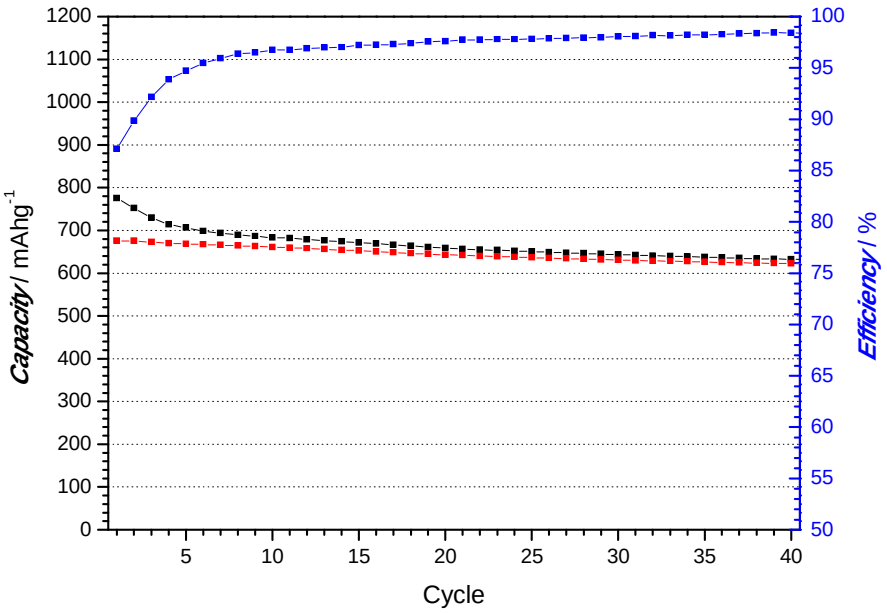

Figure 79: Capacity limited cycling of a germanium-electrode with PVdF-HFP as binder

The use of PVdF-HFP as binder provides a better cycling stability and efficiency than the CMC binder (comparison between Figure 79 and Figure 80). However surprisingly the full limited capacity of 800 $mAh \cdot g^{-1}$ was not achieved in both cases. This could be attributed to the large particles and the worse kinetic of the electrode. The second cut off condition of 4 hours constant voltage charging at 5 mV were not sufficient to charge the full capacity of 800 $mAh \cdot g^{-1}$. The better cycling stability and efficiency of the PVdF-HFP binder led to the conclusion that the binding mechanism of the CMC binder, which was postulated by Hochgatterer et. al. (59) for silicon is despite of an oxide layer on the particle surface not valid for the synthesized germanium particles.

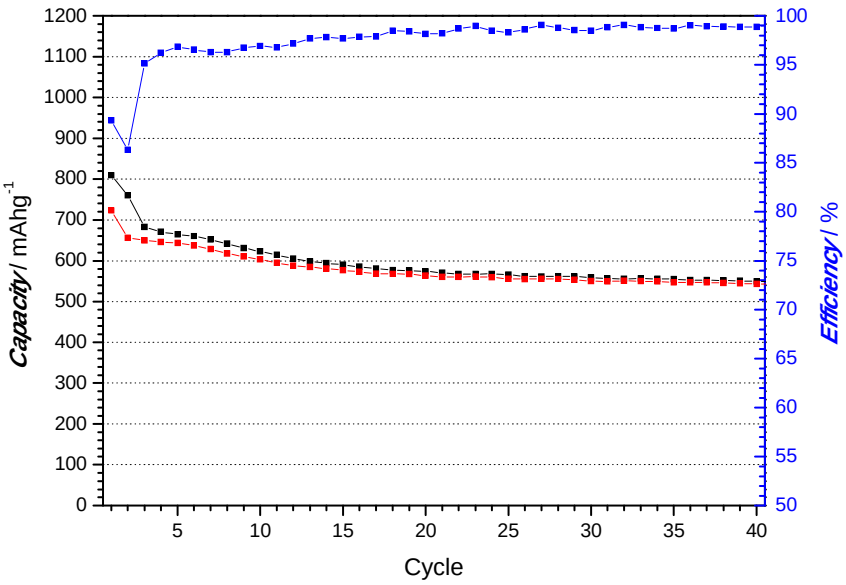

Figure 80: Capacity limited cycling of a germanium electrode with CMC as binder

In the first cycles a fluctuating of the efficiencies (Figure 80) can be observed. This fluctuation indicate a loss of active material in each cycle, what is indeed surprising because the capacity was limited to 800 $mAh \cdot g^{-1}$ and so a loss of active material should be compensated by the generated active material pool. However the fluctuating cycling efficiencies could be explained by loss of active material particles during cycling.

The cycling results clearly indicate that it is not only possible to cycle expensive thin film germanium electrodes produced by chemical vapour deposition or germanium nano wires stable over several cycles. The synthesized germanium particles also showed an appropriate cycling behaviour and are, not only because of economic reasons, a more appropriate choice than thin films electrodes prepared by CVD. Also the processability is an advantage of these particles and so a further research and development of these particles, for the use as active material on the negative side in lithium ion batteries, seems to be meaningful.

4 Conclusion

Due to the miniaturization and optimization of portable electronic devices, higher specific energies ($Wh \cdot kg^{-1}$) and energy densities ($Wh \cdot l^{-1}$) are required. Compared to other batteries, particularly aqueous ones like the nickel metal hydride system, it is obvious that lithium ion batteries (LIBs) are the only electrochemical energy storage system that will be able to fulfil all market requirements.

In order to achieve higher energy densities it is necessary to replace the common used graphitic carbons by a new generation of lithium intermetallic compounds forming materials like silicon. Unfortunately, the achievable high capacities are linked with many disadvantages, given by the chemical and physical nature of these intermetallic compounds. High volume changes during lithiation/delithiation connected with the highly ionic character leads to mechanical stress and a rapid decay of the capacity.

The degradations mechanisms of particles in the µm range as well as the influence of the particle size on the cycling stability were studied in literature sufficient (47) (79) (80). There is a deviant chemistry behaviour of nano sized particles compared to macro sized ones, resulting as well in a different deformation, volume expansion and cracking behaviour and improves the cycling stability significantly.

Unfortunately the use of nano sized particles leads to an increased electrode/electrolyte phase boundary, given by the huge surface area of these particles. Due to the reason that the, in the first cycle formed, SEI is quite unflexible, a permanent rebuilding of the SEI combined with electrolyte decomposition and loss of mobile lithium is the result. This effect is even worsen by the huge surface area of the nano particles. In a full cell the loss of mobile lithium leads to rapid capacity decay because the capacity becomes controlled by the amount of mobile lithium available from the cathode.

For this reason an active material with a reduced surface area was developed in this work. This material is able to provide the same cycling stability like silicon/graphite composite materials using nano silicon but offers the advantage of an improved coloumbic efficiency.

The new way to prepare this high capacity silicon/graphite composite material through decomposition of a polymeric silane precursor on a porous natural graphite results in a novel structured material. The obtained good electrochemical properties of this composite material can be explained by its structure. The production process leads to silicon deposition, not only on the

graphite particles but also in the pores of the graphite. The obtained active material consisted of ⅓ of amorphous silicon and ⅔ of graphite (stochiometry $C_{2/3}Si_{1/3}$) resulting in a capacity of 1200 mAh·g^{-1}. Good embedment of the silicon in the graphite matrix results in a stable cycling behaviour for 100 cycles at 840 mAh·g^{-1} and excellent efficiencies of over 99%. Due to the fact that the decomposition of the silane gel was neither accompanied with a volume expansion nor with a volume contraction, the amorphous silicon was excellent linked to the graphite without damaging its crystalline structure. The graphite is also able to compensate the volume changes of the silicon during lithiation/delithiation without being damaged.

Results displayed by in situ gas pressure measurements indicate that the obtained particles in the micrometer range reduce the irreversible capacity by electrolyte decomposition and other parasitic surface reactions significantly. The reduced particle/electrolyte phase boundary results in a decreased film formation, in the first, and film rebuilding reactions during following cycles.

The influence of cycling conditions and parameters on the cycling behaviour of silicon containing electrodes and their importance for a long cycle life were also shown in this work. The results clearly indicate that by limiting the capacity or limiting the cut off potential a control of the volume changes during cycling is possible. Therefore a control of the formation of the intermetallic phases can be achieved. Also the crystallization of the $Li_{15}Si_4$ phase can be avoided, resulting in a decreased loss of active material during cycling.

Further results show the positive influence of a 3 dimensional electrode network with enhanced electronic conductivity by the use of copper nano wires or by the use of a 3 dimensional current collector. By building up a mechanical stabilized 3 dimensional networtk it is possible to avoid the loss of active material by spalling of particles. The results also indicate, that by the use of this electrode setup, coloumbic efficiencies can be achieved, that allow the application of the developed material in full cells.

In the final chapter the preparation and electrochemical performance of electrodes containing germanium particles are shown. The synthesized germanium particles also show an appropriate cycling behaviour and are, not only because of economic aspects, a more appropriate choice than thin films electrodes prepared by CVD. Because of the simple processability of these particles and a, compared to silicon, 400 times higher lithium diffusivity, the use of these particles as additive, in silicon containing electrodes seems to be a good choice as well.

5 Abbreviations

CMC	carboxymethylcellulose
CPS	cyclopentasilane
C-rate	definition: current that is needed to charge the battery/electrode within one hour
CV	cyclovoltammogramme
CVD	chemical vapour deposition
DEC	diethylenecarbonate
EC	ethylenecarbonate
EDA	ethylenediamine
EDX	energy dispersive X-ray spectroscopy
EELS	electron energy loss spectroscopy
GIC	graphite intercalation compounds
GITT	galvanostatic intermittent titration technique
HFP	hexafluoropropylene
HRTEM	high resolution transmission electron microscopy
LIB	lithium ion battery
$LiPF_6$	lithiumhexafluorophosphate
MS	mass spectrometry
NMC	lithium nickel manganese cobaltoxide
NMP	N-methyl pyrolidone

NMR	nuclear magnetic resonance spectroscopy
OCV	open circuit voltage
PC	propylenecarbonate
PD_{Li}	lithium packing density
PVdF	polyvinylidene difluoride
SEM	scanning electron microscopy
SBR	styrene butadiene rubber
SEI	solid electrolyte interphase
SEM	scanning electron microscopy
Si/C	silicone/graphite
SOC	state of charge
TEM	transmission electron microscopy
TGA	thermogravimetric analysis
TPC	temperature controlled pressure characterisation
VC	vinylenecarbonate
XRD	X-ray diffraction
LIC	lithium intermetallic compounds

6 List of Figures

7 List of Tables

8 References

1. *25th International Battery Seminar & Exhibit.* **Takeshita, H.** Fort Lauterdale, USA : s.n., 2008.

2. European Commision. [Online] [Cited: 19 01 2011.] http://ec.europa.eu/research/energy/pdf/expert_workshops.pdf.

3. **S. Koller, M. Schmuck.** lecture. *Batteries and Supercapacitors.* TU Graz : s.n., 2010.

4. **S. Patoux, L.Sannier, H. Lignier, Y. Reynier, C. Bourbon, S. Jouanneau, F. Le Cras, S. Martinet.** *Electrochim. Acta.* 53, 2007, 4137-4145.

5. **M. Yoshio, T. Tsumura, N. Dimov.** *J. Power Sources.* 146, 2005, 10-14.

6. **Sony.** [Online] [Cited: 14 02 2011.] http://www.sony.net/SonyInfo/News/Press/200502/05-006E/.

7. **L. Galvani,** *De viribus electricitatis in motu musculari commentarius.* Bologna : Accademia delle Scienze, 1791.

8. [Online] [Cited: 11 01 2011.] http://de.academic.ru/dic.nsf/dewiki/301012.

9. **Horwood, E.** *Instrumental Methods in Electrochemistry* . Chichester : Southampton Electrochemistry Group, 1985.

10. **Besenhard, J.O.** *Handbook of Battery Materials.* Weinheim : Wiley, 1999.

11. **C. H. Hamann, A. Hamnett, W. Vielstich.** *Electrochemistry.* Weinheim : Wiley-VCH, 1998.

12. **A.J. Bard, I.R. Faulkner.** *Electrochemical Methods.* London : John Wiley, 1980.

13. **B. Scrosati, Jürgen Garche.** *J. Power Sources.* 195, 2010, 2419 - 2430.

14. **J. Maier.** *J. Power Sources.* 174, 2007, 569-574.

15. **Pierson, H.O.** *Handbook of Carbon, Graphite, Diamond and Fullerenes.* Park Ridge, NJ : Noyes Publication, 1993.

16. **Kinoshita, K.** *Carbon, Electrochemical and Physiochemical Properties.* New York : Wiley, 1987.

17. **O. Vohler, F. von Sturm, E. Wege, H. von Kienle, M. Voll, P. Kleinschmitt.** *Ullmann`s Encyclopedia of Industrial Chemistry.* Weinheim : Wiley, 1986.

18. **A. Herold.** *Bull. Soc. Chim. France.* 187, 1955, 999.

19. **M. Wakihara.** *Materials Science and Engineering.* 33, 2001, 109 – 134.

20. **Inaba, M.** Negative Electrodes: Graphite. *Encyclopedia of Electrochemical Power Sources.* s.l. : Elsevier Science & Technology, 2009.

21. **D. Billaud, E. McRae, A. Herold.** *Mat. Res. Bull.* 14, 1979, 857.

22. **X. Y. Song, K. Kinoshita, T.D. Tran.** *J. Electrochem. Soc.* 143, 1996, L120.

23. **Moret, R.** *Intercalation in Layered Materials.* New York : Plenum, 1986.

24. **Fischer, J.E.** *Chemical Physics of Intercalation.* New York : Plenum, 1987.

25. **J.R. Dahn.** *Physical Review.* 44, 1991, Vol. 17, 9170.

26. **K.-C. Moeller, M. Winter.** Script zum Praktikum Anorganisch-Chemische Technologie. *Primäre und wiederaufladbare Lithium-Batterien.* TU Graz : s.n., 2005.

27. **M. Winter, K.-C. Moeller, J.O. Besenhard.** Carbonaceous and Graphitic Anodes. *Science and Technology of Lithium batteries.* Dordrecht : Kluwer Academic Publischers, 2004.

28. **M. Winter, J. O. Besenhard, M. E. Spahr, P. Novak.** *Adv. Mater.* 10, 1998, 725 – 763.

29. **N. Daumas, A. Herold.** *C. R. Acad. Sci. Paris.* 268C, 1969, 373.

30. **N. Daumas., A. Herold.** *Bull. Soc. Chim.* 5, 1971, 1598.

31. **J.R. Dahn, R. Fong, M.J. Spoon.** *Phys. Rev. B.* 42, 1990, 6424.

32. **A.H. Whitehead, K. Edström, N. Rao, J.R. Owen.** *J. Power Sources.* 63, 1996, 41.

33. **W. Huang, R. Frech, J. Electrochem. Soc.** *J. Electrochem. Soc.* 145, 1998, 765.

34. **M. Inaba, H. Yoshida, Z. Ogumi, T. Abe, Y. Mizutani, M. Asano.** *J. Electrochem. Soc.* 142, 1995, 20.

35. **J.B. Barr, I.C. Lewis.** *Carbon.* 16, 1978, 439.

36. **J. R. Dahn, Tao Zheng, Yinghu Liu, J. S. Xue.** *Science.* 1995, Vol. 270, 590-593.

37. **Y. Liu, J. S. Xue, T. Zheng, J. R. Dahn.** *Carbon.* 34, 1996, Vol. 2, 1993-200.

38. **M. Winter, J.O. Besenhard.** *Electrochim. Acta.* 45, 1999, Vols. 1-2, 31-50.

39. **C.E. Johnson, M.S. Foster.** *J. Electrochem. Soc.* 116, 1969, 1612.

40. **S. Lai.** *J. Electrochem. Soc.* 123, 1976, 1196.

41. **W. Müller, H. Schäfer.** *Z. Naturforsch.* 28b, 1973, 246.

42. **J.S. Dunning, W.H. Tiedemann, L. Hsueh, D.N. Bennion.** *J. Electrochem. Soc.* 118, 1971, 1886.

43. **M.L.B. Rao.** *J. Electrochem. Soc.* 114, 1967, 665.

44. **R.A. Huggins.** *J. Power Sources.* 22, 1998, 341.

45. **R.A. Huggins,** *J. Power Sources.* 26, 1989, 109.

46. **Shinbun, Nippon Denki.** March 11, 1996.

47. **J. Yang, M. Winter, J.O. Besenhard.** *Solid State Ionics.* 90, 1996, 281.

48. **J.O. Besenhard, J. Yang, M. Winter.** *J. Power Sources.* 68, 1997, 87.

49. **K. Brandt.** *Solid State Ionics.* 69, 1994, 173.

50. **R. Nesper.** *Prog. Solid State Chem.* 20, 1990, 1.

51. **Nesper, R.** *Angew. Chem. Int. Ed. Engl.* 30, 1991, 789.

52. **Huggins, R.A.** Lithium Alloy Anodes. [book auth.] J.O. Besenhard. *Handbook of Battery Materials.* Weinheim : Wiley-VCH, 1999.

53. **B.A. Boukamp, G.C. Lesh, R.A. Huggins,.** *J. Electrochem. Soc.* 128, 1981, 725.

54. **T. Brousse, R. Retoux, U. Herterich, D. M. Schleich,.** *J. Electrochem. Soc.* 145, 1998, 1.

55. **M. Holzapfel, H. Buqa, L.J. Hardwick, M. Hahn, A. Würsig, W. Scheifele, P. Novák, R. Kötz, C. Veit, F. M. Petrat.** *Electrochim. Acta.* 52, 2006, 973.

56. **C.K. Chan, H. Peng, G. Liu, K. McIlwrath, X. F. Zhang, R.A. Huggins, Y. Cui.** *Nature Nanotechnology.* 3, 2008, 31.

57. **L.F. Cui, R. Ruffo, C.K. Chan, H. Peng, Y. Cui.** *Nano Letters.* 9, 2009, Vol. 1, 491.

58. **B. Lestriez, S. Bahri, J. Sandu, L. Roue, D Guyomard.** *Electrochem. Commun.* 9, 2007, 2801.

59. **N.S. Hochgatterer, M.R. Schweiger, S. Koller, P.R. Raimann, T. Wöhrle, C. Wurm, M. Winter.** *Electrochem Solid State Lett.* 11, 2008, A76.

60. **C.J. Wen, R.A. Huggins.** *J. Solid State Chem.* 37, 1981, 271.

61. **Börnstein, Landolt.** *New Series IV/11A4.* s.l. : Springer, 2001. 330.

62. **A. Anani, R.A. Huggins.** *J. Power Sources .* 38, 1992, 351.

63. **H. Li, X. Huang, L. Chen, G. Zhou, Z. Zhang, D, Yu, Y. J. Mo, N. Pei.** *Solid State Ionics .* 135, 2000, 181.

64. **P. Limthongkul, Y.I. Jang, N. J. Dudney, Y.M. Chiang.** *J. Power Sources.* 119 -121, 2003, 604.

65. **M. N. Obrovac, L. Christensen.** *Electrochem. Solid- State Lett.* 7, 2004, A93.

66. **P. Limthongkul, Y.I.Jang, N. J. Dudney, Y.M. Chiang.** *Acta Materialia.* 51, 2003, Vol. 4, 1103-1113.

67. **T. D. Hatchard, J. R. Dahn.** *J. Electrochem. Soc.* 151, 2004, A838.

68. **J. Y. Kwona, J. H. Ryub, S. M. Oha.** *Electrochim. Acta.* 52, 2010, Vol. 27, 8051-8055.

69. **Koller, S.** About the Nature of the Electrochemical Formation of Binary Lithium-Silicon Intermetallic Phases from Nonaqueous Electrolytes. *Dissertation.* 2009.

70. **C. K. Chan, X. F. Zhan, Y. Cui.** *Nano Letters.* 8, 2008, Vol. 1, 307-309.

71. **Y. Nagao, H. Sakaguchi, H. Honda, T. Fukunaga, T. Esaka,.** *J. Electrochem. Soc.* 151, 2004, A1572.

72. **U. Kasavajjula, C. Wang, A., J. Appleby.** *J. Power Sources.* 163, 2007, 1003 - 1039.

73. **J. Gratz, C.C. Ahn, R. Yazami, B. Fultz.** *J. Electrochem. Soc.* 151, 2004, A698-A702.

74. **C.S. Fuller, J.C. Severiens.** *Phys. Rev.* 96, 1954, 21.

75. **M. R. St. John, A. J. Furgala, A. F. Sammells.** *J. Electrochem. Soc.* 127, 1980, C136.

76. **S. Yoon, C. M. Park, H.J. Sohn.** *Electrochemical and Solid State Letters.* 11, 2008, A42 - A45.

77. **J. Sangster, A. D. Pelton.** *Journal of Phase Equilibria.* 18, 1997, Vol. 3, 289-294.

78. **G. Cui, L. Gu, L. Zhi, N. Kaskhedikar, P.A. v. Aken, K. Müllen, J. Maier.** *Adv. Mater.* 20, 2008, 3079-3083.

79. **M. Holzapfel, H. Buqaa, L. J. Hardwick, M. Hahn, A. Würsig, W. Scheifele, P. Novák, R. Kötz, C. Veit, F.M. Petrat.** *Electrochim. Acta.* 52, 2006, Vol. 3, 973-978.

80. **J. Wolfenstine.** *J. Power Sources.* 79, 1999, 111.

81. **W.R. Liu, M.H. Yang, H.C. Wu, S. M. Chiao, N.L. Wua.** *Electrochemical and Solid-State Letters.* 8, 2005, Vol. 2, A100.

82. **H. Buqa, M. Holzapfel, F. Krumeich, C. Veit, P. Novak.** *J.Power Sources.* 161, 2006, 617-622.

83. **J.-S. Bridel, T. Azaı, M. Morcrette, J.-M. Tarascon, D. Larcher.** *Chem. Mater.* 22, 2010, 1229-1241.

84. **B. Lestriez, S. Bahri, I. Sandu, L. Roue, D. Guyomard.** *Electrochem. Commun.* 9, 2007, 2801 - 2806.

85. **D. Mazouzi, B. Lestriez, L. Roue, D. Guyomard.** *Electrochem. Solid State Letters.* 12, 2009, A215.

86. **D. Guyomard, J-M. Tarascon.** *Adv. Mater.* 6, 2004, 408.

87. **E. Peled,** *J. Electrochem Soc.* 126, 1979, 2047.

88. **R. Mogi, M. Inaba, Y. Iriyama, T. Abe, Z. Ogumi.** *J. Electrochem Soc.* 149, 2002, 385.

89.**E. Peled**, *J. Power Source.* 9, 1983, 253.

90. **P. Vermaa, P. Maire, P. Novák.** *Electrochim. Acta.* 55, 2010, Vol. 22, 6332 - 6341.

91. **D. Alliata, R. Kotz, P. Novak, H. Siegenthaler.** *Electrochem. Commun.* 2, 2000, 436.

92. **T. Yoshida, M. Takahashi, S. Morikawa, C. Ihara, H. Katsukawa, T. Shiratsuchi, J. Yamaki.** *J. Electrochem. Soc.* 153, 2006, 576.

93. **K. Edström, M. Herstedt, D.P. Abraham.** *J. Power Sources.* 153, 2006, 380.

94. **D. Aurbach.** *J. Power Sources.* 89, 2000, 206.

95. **M. Winter, J. O. Besenhard.** *Chemie in unserer Zeit.* 6, 1999, 322.

96. **D. Rahner,** *J. Power Sources.* 81-82, 1999, 358-361.

97. **J.O. Besenhard, M. Winter, J. Yang, W. Biberacher.** *J. Power Sources.* 54, 1995, 228.

98. **D. Aurbach.** *J. Power Sources.* 119 - 121, 2003, 497.

99. **S.S. Zhang,** *J. Power Sources.* 162, 2006, 1379-1394.

100. **Hochgatterer, N. S.** Zellulosechemie in der Lithium-Ionen-Technologie. *Dissertation.* 2008.

101. **N.S. Choi, K.H. Yew, M.S. Sung, Y. Nitta, S.S. Kim, K.Y. Lee.** *Proceedings of the 56th ISE Meeting , Busan, Korea.* 2005, Abstract 3A-068-P.

102. **Y.M. Lee, J.Y. Lee, H.-T. Shim, J.K. Lee, J.-K. Park.** *J. Electrochem. Soc.* 154, 2007, A515.

103. **C.K. Chan, R. Ruffo, S.S. Hong, Y. Cui.** *J. Power Sources.* 189, 2009, 1132-1140.

104. **P. Zuo, G. Yin, Z. Yang, Z. Wang, X. Cheng, D. Jia, C. Du.** *Materials Chemistry and Physics.* 115, 2009, 757.

105. **H.Wolf, Z. Pajkic, T. Gerdes, M.Willert-Porada.** *J. Power Sources.* 190, 2009, 157.

106. **Z. Luo, D. Fan, X. Liu, H. Mao, C. Yao, Z. Deng.** *J. Power Sources.* 189, 2009, 16.

107. **M. Schmuck, A. Balducci, B. Rupp, W. Kern, S. Passerini, M. Winter,.** *Journal of Solid State Electrochemistry.* 12, 2008, 2203.

108. **A.F.B. Braga, S.P. Moreira, P.R. Zampieri, J.M.G. Bacchin, P.R. Mei.** *Solar Energy Materials & Solar Cells.* 92, 2008, 418.

109. **T. Pöpken, R. Sonnenschein.** *Verfahren zur Herstellung von Silicium . DE102004010055A1* 2005.

110. **A.F. Holleman, E. Wiberg,.** *Lehrbuch der Anorganischen Chemie.* Berlin : de Gruyter, 2007.

111. **T. Shimoda, Y. Matsuki, M. Furusawa, T. Aoki, I. Yudasaka, H. Tanaka, H. Iwasawa, D. Wang, M. Miyasaka, Y. Takeuchi.** *Nature.* 440, 2006, 783.

112. **B. Fuchsbichler, S. Koller, F. Uhlig, S. Pichler.** *Neues Elektrodenaktivmaterial für elektrochemische Elemente. DE 102008063552 A1* 2008.

113. **B. Fuchsbichler, C. Stangl, H. Kren, F. Uhlig, S. Koller.** *J. Power Sources.* 196, 2011, Vol. 5, 2889.

114. **E. Hengge, G. Bauer.** *Angewandte Chemie.* 85, 1973, 304.

115. **E. Hengge, R. Janoschek.** *Chemical Reviews.* 95, 1995, 1495.

116. *Spectral data.* [Wiley Subscription Services] Spectrum ID: CC-01-SI_NMR-2042.

117. **Y.S. Jung, K.T. Lee, S.M. Oh.** *Electrochim. Acta.* 52, 2007, 7061.

118. **W. Weppner, R.A. Huggins.** *J. Electrochem. Society.* 124, 1977, 1569.

119. W. **Weppner, R.A. Huggins,** *Journal of Solid State Chemistry.* 22, 1977, 297-308.

120. **X.H. Rui, N. Ding, J. Liu, C. Li, C.H. Chen.** *Electrochim. Acta.* 55, 2010, 2384-2390.

121. **Y. Chang, M.L. Lye, H.C. Zeng.** *Langmuir.* 21, 2005, 3746-3748.